X-Ray Studies of the Density Depletion at Hydrophobic Water-Solid Interfaces

Markus Mezger
Stuttgart, 2008

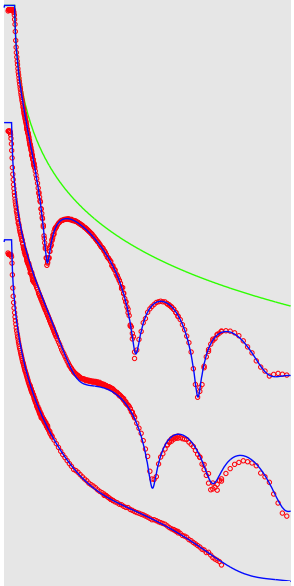

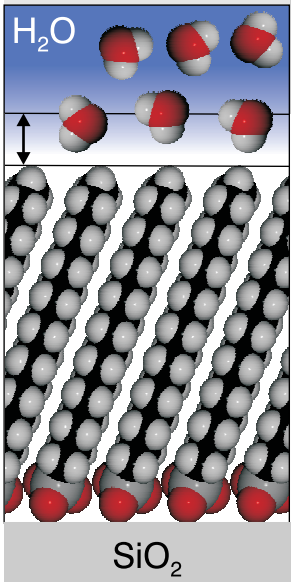

Max-Planck-Institut
für Metallforschung
Stuttgart

Institut für Theoretische
und Angewandte Physik
Universität Stuttgart

X-ray Studies of the Density Depletion at Hydrophobic Water-Solid Interfaces

Von der Fakultät Mathematik und Physik der Universität Stuttgart
zur Erlangung der Würde eines Doktors der
Naturwissenschaften (Dr. rer. nat.) genehmigte Abhandlung

Vorgelegt von

MARKUS MEZGER

aus Stuttgart-Bad Cannstatt

Hauptberichter:	Prof. Dr. H. Dosch
Mitberichter:	Prof. Dr. C. Bechinger
Eingereicht am:	10. Januar 2008
Tag der mündlichen Prüfung:	20. Mai 2008

Institut für Theoretische und Angewandte Physik
der Universität Stuttgart
Max-Planck-Institut für Metallforschung
in Stuttgart

2008

Contents

1 Deutsche Zusammenfassung **5**
Motivation 5
Hochenergie Röntgen Reflektivität 6
Experimentelles 7
Ergebnisse 7
Diskussion 13

2 Introduction **14**

3 Water at interfaces **16**
3.1 Properties of bulk water 16
3.2 Hydrophobic interfaces 20
3.3 The solid-liquid interface –Theoretical description 24
3.4 The solid-liquid interface –Experimental results 29

4 X-Ray scattering and data analysis methods **36**
4.1 Introduction to x-ray reflectivity 36
4.2 Calculation of the x-ray reflection pattern 39
4.3 From scattering data to real space information 46
4.4 The x-ray scattering cross section 55

5 Experimental Details **59**
5.1 X-ray setup 59
5.2 Sample environment 72
5.3 Sample preparation 76
5.4 Reflectivity experiments 80

6 Data analysis, results, and discussion **83**
6.1 Overview of the x-ray experiments 83
6.2 The dry OTS-layer 85
6.3 The hydrophobic water-OTS interface 88
6.4 The water-SiO_2 interface. 96
6.5 Influence of gases dissolved in the water 96
6.6 Discussion of the interfacial density depletion 97
6.7 Radiation damage in the OTS-layer 99

7 Conclusions **105**

8 Outlook **109**

A Abbreviations and Acronyms **111**

B Symbols used in Equations **112**

Bibliography **114**

Acknowledgment **126**

Chapter 1

Deutsche Zusammenfassung

Motivation

Aufgrund der elementaren Bedeutung von Wasser für das Leben auf der Erde stellte die Erforschung seines Aufbaus und seiner Eigenschaften seit jeher einen Schwerpunkt wissenschaftlichen Arbeitens dar. So setzten sich schon die Philosophen des antiken Griechenlands und später auch Leonardo da Vinci intensiv mit diesem Themenkomplex auseinander [1]. Die Beschreibung von Wasser unterscheidet sich in vielerlei Hinsicht von der einfacher Flüssigkeiten und stellt aufgrund der komplexen Natur der Wasserstoffbrückenbindungen auch heute noch eine Herausforderung dar. Ihr Ursprung findet sich in der atomaren Struktur des Wassermoleküls, welches in Abb. 1.1 schematisch dargestellt ist. Eine deutschsprachige Zusammenfassung der Eigenschaften von Wasser sowie offener Fragen, welche Gegenstand aktueller Forschung sind, findet sich in den Arbeiten von Ludwig und Paschke [2] aus dem Jahr 2005 sowie von P. Ball [3].

Bringt man nun Wasser in Kontakt mit einer Grenzfläche, so treten neben den Wechselwirkungen innerhalb der Flüssigkeitsmoleküle weitere mit der Wand auf. Von unpolaren Materialien scheint Wasser aufgrund seiner stark anziehenden intermolekularen Kräfte abgestoßen zu werden, was als hydrophober Effekt bekannt ist. Dagegen können sich zwischen polaren (hydrophilen) Substanzen und den ebenfalls polaren Wassermolekülen stark attraktive Wechselwirkungen ausbilden, welche zu Benetzung führen [4]. Hydrophobe und hydrophile Grenzflächen spielen in der Natur eine wesentliche Rolle. Beispiele finden sich sowohl makroskopisch in Form wasserabstoßender Wachsschichten auf der Cuticula vieler Pflanzen, als auch auf molekularer Ebene im Zusammenhang mit der Stabilität und der Form biologischer Strukturen. Sie bestimmen die Faltung von Proteinen [5] und den Aufbau von Zellmembranen [6].

Daher ist das mikroskopische Verständnis der Wechselwirkung zwischen Wasser und hydrophilen sowie hydrophoben Materialien unerlässlich, um dessen Eigenschaften in biologischen aber auch technischen Systemen quantitativ beschreiben und vorhersagen zu können [7]. Alle Grenzflächenphänomene, seien es Be- und Entnetzung oder Reibung auf mikroskopischer Ebene sind äußerst sensitiv auf die Details dieser Wechselwirkung. Insbesondere ist das Auftreten einer dünnen Flüssigkeitsschicht erniedrigter Dichte, welche

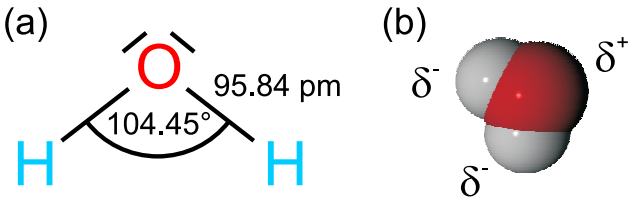

Abbildung 1.1: Molekulare Struktur des Wassers.

sich an hydrophoben Wassergrenzflächen ausbildet, für die eingangs erwähnten Erscheinungen von größter Relevanz. Gerade dieses Phänomen ist in der aktuellen Forschung jedoch Gegenstand kontrovers geführter Diskussionen [8].

Hochenergie Röntgen Reflektivität

In einem konventionellen Röntgenreflektivitätsexperiment trifft ein Röntgenstrahl unter flachem Winkel auf eine Oberfläche und wird von dieser zurück geworfen. Die reflektierte Intensität wird als Funktion des vertikalen Impulsübertrags q_z gemessen, indem der Einfallswinkel α_i und Ausfallswinkel α_f symmetrisch eingestellt werden. Die Elektronendichteverteilung $\rho_\mathrm{e}(z)$ senkrecht zur Oberfläche erzeugt dabei ein charakteristisches Interferenzmuster, aus dem sich die vertikale Struktur nahe der Oberfläche rekonstruieren lässt.

Im Gegensatz zu Röntgenstrahlen bei $10\,\mathrm{keV}$, welche in Wasser oder anderen Flüssigkeiten und Festkörpern bereits auf einer Länge von wenigen 100 $\mu\mathrm{m}$ größtenteils absorbiert werden, lassen sich mit hochenergetischen Photonen ($E \approx 70\,\mathrm{keV}$) mehrere Zentimeter von Wasser durchdringen. Dies ermöglicht es, mit Reflektivitätsexperimenten nicht nur freie Oberflächen zu vermessen, sondern eröffnet auch einen Zugang zu tief vergrabenen Grenzflächen. Während konventionelle Röntgenreflektivitätsexperimente weit verbreitet und fertige Aufbauten an vielen Synchrotronstrahlungsquellen vorhanden sind, sind Hochenergiereflektivitätsmessungen mit komplexen Aufbauten verbunden, welche bisher für reine Anwender nicht zugänglich waren [9].

Zur Analyse der in dieser Arbeit gewonnenen Reflektivitätsmessungen wurde ein Computerprogramm entwickelt. Seine Stärke im Vergleich zu anderen Auswerteprogrammen besteht insbesondere in der Implementierung verschiedener Nebenbedingungen, welche für eine eindeutige Rekonstruktion der untersuchten Strukturen unerlässlich ist. Es basiert auf der von Parratt [10] entwickelten Rekursionsmethode, sowie der Implementation der Streugleichung in kinematischer Nährung (Master-Formalismus [11]). Zur Berechnung quasi-beliebiger vertikaler Elektronendichteprofile wird die Struktur in $0.2\,\text{Å}$ dicke Scheibchen unterteilt, in welchen der Brechungsindex als konstant angenommen werden kann [12]. Ein Monte Carlo Algorithmus [13] erlaubt auch in hochdimensionalen Parameterräumen das Auffinden des globalen Minimums und damit eine zuverlässige Bestimmung der Grenzflächenstruktur.

Experimentelles

Hydrophobe Grenzflächen wurden durch Aufbringen organischer Moleküle mit einer langen unpolaren Alkylkette auf Siliziumdioxid (SiO_2) hergestellt. Unter bestimmten Bedingungen bildet Octadecyl-Trichlorsilan (OTS) auf Silizium-Substraten selbstorganisierte monomolekulare Schichten, welche kovalent an das auf der Si-Oberfläche gewachsene SiO_2 gebunden sind. Für Reflektivitätsmessungen wurden Proben von $20\,\mathrm{mm} \times 25\,\mathrm{mm}$ Größe und einer Dicke von $625\,\mu\mathrm{m}$ verwendet. Um als Ausgangsbasis eine hydrophile OH-terminierte Oxidoberfläche zu erhalten, wurden die Si-Wafer in Piranha geätzt. Die hydrophobe Beschichtung erfolgte aus einer 1 mM Lösung von OTS in einer 3:1 Mischung von n-Hexan und Chloroform durch Einlegen der Si-Substrate über einen Zeitraum von 3 Stunden.

Die Röntgenreflektivitätsexperimente wurden am Hochenergiemessplatz ID15A der Europäischen Synchrotron Strahlungsquelle (ESRF) in Grenoble, Frankreich mit Hilfe eines neuartigen und speziell für Grenz- und Oberflächenexperimente optimierten Hoch-Energie-Mikro-Diffraktometers (HEMD) durchgeführt. Dieses Instrument wurde parallel zu dieser Arbeit durch das MPI für Metallforschung an der ESRF installiert. Abbildung 1.2 zeigt schematisch den experimentellen Aufbau, welcher in dieser Arbeit Anwendung fand. Ein hochenergetischer Röntgenstrahl ($E = 72.5\,\mathrm{keV}$) wird mittels eines Linsensystems (CRL), bestehend aus 194 einzelnen parabolischer Aluminiumlinsen, auf die Probenposition fokussiert. Hiermit konnte der Strahl auf eine Größe von $6.5\,\mu\mathrm{m} \times 25\,\mu\mathrm{m}$ (vertikal $\times$ horizontal) gebündelt werden. Damit wird auch bei kleinen Einfallswinkeln α_i ein möglichst kurzer Beleuchtungsfleck erzeugt. Die Strahlendosis wurde mittels eines dreieckigen Absorberblocks aus Bleiglas sowie einer schnell schließenden Verschlussblende im Primärstrahl soweit als möglich reduziert, um Schäden an der hydrophoben Beschichtung zu minimieren.

Eine aus Glas gefertigte Probenzelle in Verbindung mit Polyethylen, Teflon und PFA Komponenten, erlaubt die Präparation einer hochreinen hydrophoben fest-flüssig Grenzfläche (siehe Abb. 1.2). Die Kammer kann über ein Saugvakuum mit entgastem Wasser befüllt werden. Als Fenster für die hochenergetische Röntgenstrahlung dienen $0.5\,\mathrm{mm}$ dicke Glasplättchen, welche parallel in die zylindrische Probenzelle eingeschmolzen wurden.

Ergebnisse

Die Wasser-OTS-Grenzfläche

Abbildung 1.3a zeigt die experimentelle Röntgenreflektivitätsmessung zusammen mit berechneten Kurven, basierend auf verschiedenen Dichteprofilen, welche sich in der Breite d_w der Grenzflächenschicht erniedrigter Dichte unterscheiden. Eine detaillierte Analyse zeigt (siehe Abb. 1.3b), dass sich die experimentell bestimmte Reflektivitätskurve durch verschiedene Realraumprofile mit einer Grenzschichtdicke zwischen $1\,$Å und $6\,$Å wiedergeben lässt. Allen Modellen gemeinsam ist jedoch ein integrales Dichtedefizit von

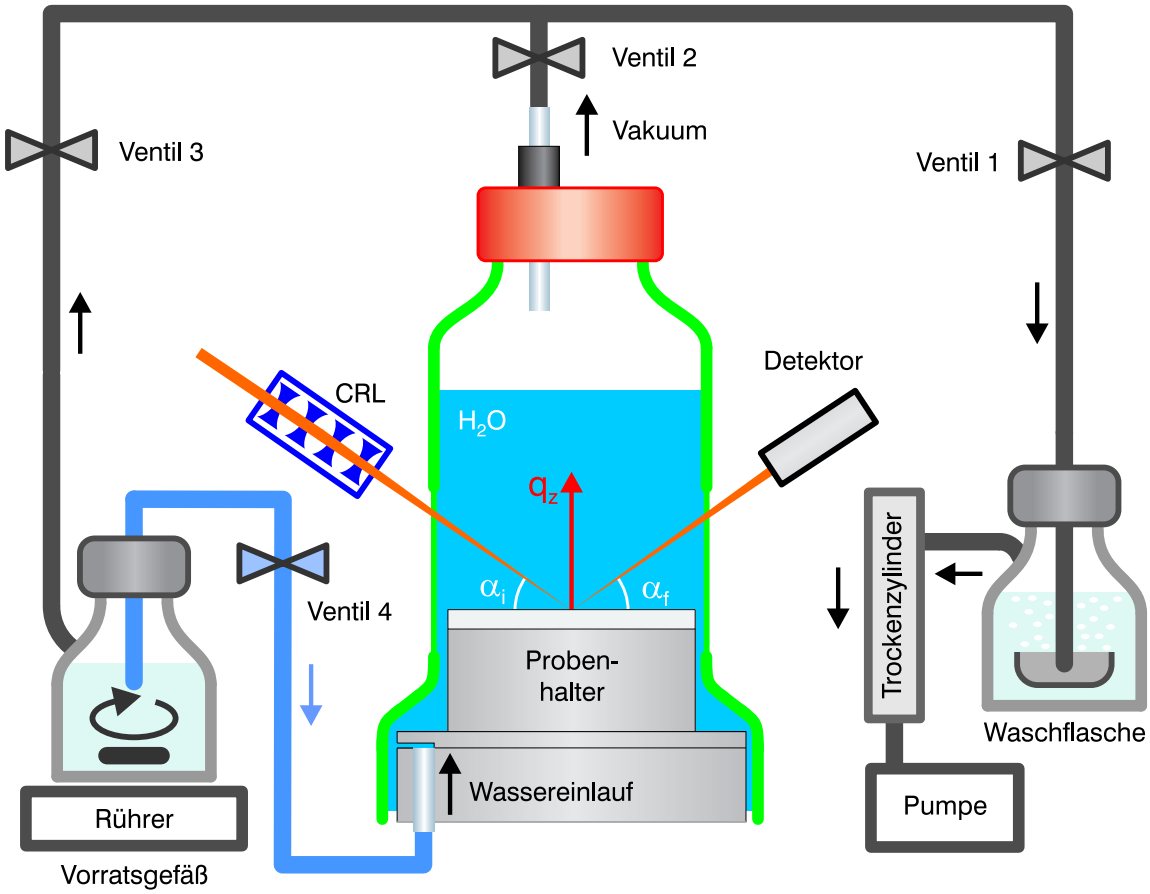

Abbildung 1.2: Skizze des experimentellen Aufbaus zur Vermessung der Wasser-OTS-Grenzfläche. Der durch die Linse (CRL) mikrofokussierte hochenergetische Röntgenstrahl durchstrahlt die mit Wasser gefüllte Probenkammer von der Seite und wird an der fest-flüssig Grenzfläche reflektiert. Durch die Verbindungen der Probenkammer mit einem Vakuumsystem und einer Vorrichtung zur Präparation von entgastem Wasser lässt sich dieses, ohne in Kontakt mit der Umgebungsluft zu kommen, in die Messzelle füllen.

$d_{\mathrm{w}}\,(\rho_{\mathrm{H_2O}} - \rho_{\mathrm{w}}) = 1.1\,\text{Å}\,\mathrm{g\,cm^{-3}}$. In Abb. 1.4 ist eine der möglichen Elektronendichteverteilungen dargestellt. Der Grund, weshalb die experimentellen Datensätze keine Unterscheidung zwischen den angegebenen Modellen zulassen, liegt einerseits im beschränkten Impulstransferbereich q_z, welcher sich im Ortsraum durch eine auf $\frac{\pi}{q_z^{\max}}$ limitierte Realraumauflösung bemerkbar macht und andererseits in der Rauigkeit der hydrophoben Beschichtung, welche durch die molekulare Struktur der Alkylketten gegeben ist.

Dass sich die vertikale Struktur überhaupt mit derartiger Genauigkeit bestimmen lässt, liegt an der Kontrastanpassung zwischen den dicht gepackten Kohlenwasserstoffketten und dem Wasser. Die wasserabstoßende Schicht wirkt damit zugleich als Referenzlage, deren Sichtbarkeit in Reflektivitätsexperimenten erst durch das Vorhandensein einer zusätzlichen Grenzflächenschicht erniedrigter Dichte erreicht wird. Hieraus wird auch ersichtlich, weshalb sich aus vergleichbaren Röntgenreflektivitätsexperimenten von Wasser an hydrophilen SiO_2 Grenzflächen keine Aussagen zum nanoskopischen Dichteprofil ableiten lassen.

Ein in der Literatur kontrovers diskutierter Sachverhalt betrifft die Existenz so genannter Nanoblasen (*nanobubbles*) an hydrophoben Wassergrenzflächen. Während diese in manchen AFM Messungen [14–19] wiederholt beobachtet wurden, liegt die Vermutung nahe, dass es sich hierbei um einen Einschlusseffekt zwischen der AFM Spitze und dem Substrat handelt. In off-spekulären Messungen würden derartige Gasblasen zu einem starken diffusen Streusignal führen. Die hohe instrumentelle transversale Winkelauflösung des HEMD Aufbaus führt zu einer Impulstransferunschärfe im Bereich kleiner Reflektionswinkel von nur $\delta q_x = \pm 0.4 \cdot 10^{-5}\,\text{Å}^{-1}$. Bei höheren Winkeln ($q_z = 0.5\,\text{Å}^{-1}$) vergrößert sich dieser Wert auflösungsbedingt auf $\delta q_x = \pm 2 \cdot 10^{-5}\,\text{Å}^{-1}$, wobei keinerlei diffuse Streuung, welche von Nanoblasen herrühren könnte, beobachtet wurde. Die angegebene Reflexionsbreite entspricht im Realraum einer lateralen Längenskala zwischen 30 und $160\,\mu\mathrm{m}$. Damit schließen die durchgeführten Streuexperimente die Existenz von Gasblasen im Nanometerbereich aus.

Eine allgemein verständlich gehaltene Übersicht zu den Ergebnissen, welche in dieser Arbeit erzielt wurden, findet sich sowohl in den Pressemitteilungen der Max-Planck-Gesellschaft [20] und der Europäischen Synchrotronstrahlungsquelle in Grenoble [21], als auch in einem Bericht, welcher vor kurzem im Wissenschaftsmagazin “Max Planck Forschung” erschien [22].

Einfluss der im Wasser gelösten Gase auf die Grenzschicht

Eine weitere in der Literatur kontrovers geführte Diskussion dreht sich um den Einfluss im Wasser gelöster Gase auf die Grenzschicht, welche sich im Kontakt zu hydrophoben Materialien bildet. Nimmt man an, dass sich unpolare Gase aus einer gesättigten Lösung an der hydrophoben Grenzfläche anlagern, d.h. es kommt zur Bildung eines dünnen Gasfilmes, der die Grenzflächenenergie erniedrigt, so müsste sich dieser Effekt in einem vergrößerten Dichtedefizit bemerkbar machen. Es wurden daher zusätzliche Messungen mit Wasser durchgeführt, welches zuvor mit Edelgasen (Ar, Xe, Kr), linearen unpolaren (N_2,

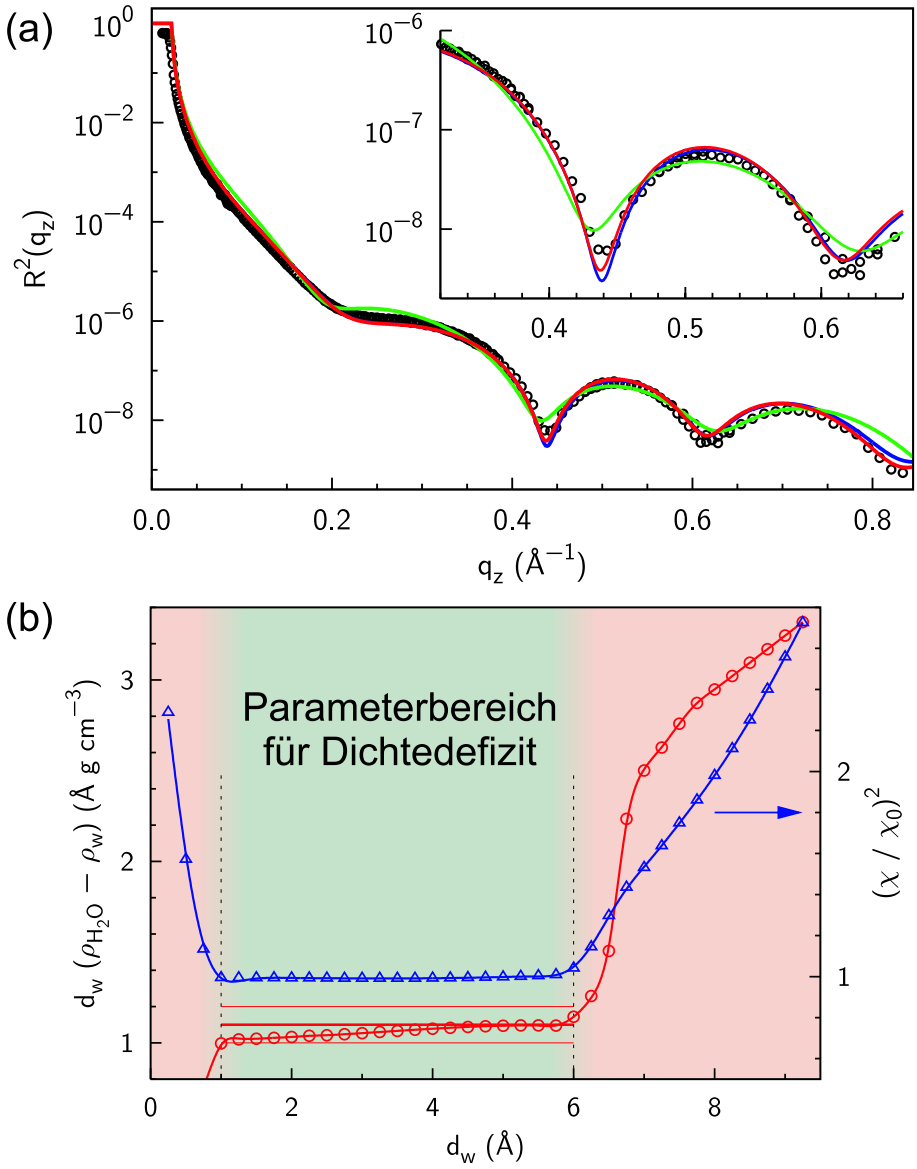

Abbildung 1.3: (a) Röntgenreflektivität der Wasser-OTS-Grenzfläche. Die experimentellen Daten (Kreise) lassen sich mit einem 4-Lagen Modell (siehe Text) unter Hinzunahme einer Grenzflächenschicht erniedrigter Dichte wiedergeben. Für eine festgehaltene Dicke der Grenzflächenschicht d_w ergeben sich durch Anpassung (durchgezogene Linien: blau $2.0\,$Å; rot $3.8\,$Å) verschiedene Parametersätze, welche die experimentellen Daten gleichermaßen gut beschreiben. Erst bei einer Schichtdicke von $8.0\,$Å (grüne Kurve) zeigen sich, insbesondere im Bereich der Minima, deutliche Abweichungen. (b) Im Bereich $1\,\text{Å} < d_\mathrm{w} < 6\,\text{Å}$ (grün schattierter Bereich) zeigen alle Parametersätze eine vergleichbare Abweichung χ (blaue Dreiecke) bei einem konstanten integrierten Dichtedefizit von $d_\mathrm{w}\,(\rho_{\mathrm{H_2O}} - \rho_\mathrm{w}) = 1.1\,\text{Å}\,\mathrm{g\,cm^{-3}}$ (rote Kreise).

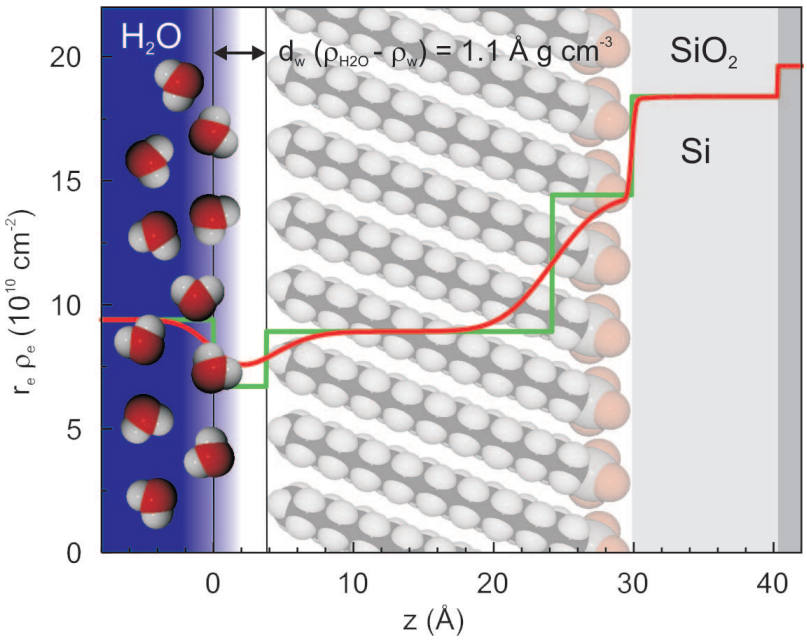

Abbildung 1.4: Rekonstruiertes Realraumelektronendichteprofil, bestehend aus SiO_2 (natives Siliziumdioxid), der OTS-Schicht aus Kopf- und Schwanzgruppe, sowie einem Bereich erniedrigter Wasserdichte an der Grenzfläche (grüne Linie: Rechtecksmodell; rote Linie: Dichteprofil unter Berücksichtigung der Rauhigkeiten zwischen den einzelnen Lagen.). Die in Abb. 1.3 eingezeichnete rote Kurve ($3.8\,\text{Å}$) basiert auf dem hier abgebildeten Elektronendichteprofil.

O_2, CO_2) und polaren Gasen (CO) angereichert wurde. Des Weiteren wurde eine Messung mit $0.5\,\text{M}$ wässriger HCl-Lösung durchgeführt. Abbildung 1.5 zeigt eine Auswahl der gemessenen Reflektivitätskurven. Es ist klar ersichtlich, dass im Rahmen der Messgenauigkeit alle Kurven, insbesondere auch bei den hohen Impulsüberträgen wie sie in dieser Arbeit erreicht wurden, deckungsgleich sind. Daraus kann geschlossen werden, dass auf einer Längenskala größer $4\,\text{Å}$, welche durch die Realraumauflösung gegeben ist, gelöste Gase keinen Einfluss auf die Grenzflächenstruktur haben. Insbesondere lässt sich eine Änderung des integralen Dichtedefizits ausschließen.

Strahlenschaden der OTS Schicht

Während sich an der trockenen OTS-Probe mehrere aufeinanderfolgende Reflektivitätsmessungen durchführen lassen, ohne dass dabei ein merklicher Strahlenschaden beobachtbar ist, tritt bei Messungen unter Wasser rasch eine Zerstörung der organischen Schicht auf. Um diesen Effekt zu quantifizieren, wurde der zeitliche Verlauf der reflektierten Intensität bei einem Impulsübertrag destruktiver Interferenz ($q_z = 0.44\,\text{Å}^{-1}$) beobachtet. Selbst kleine strukturelle Veränderungen, welche mit einer veränderten Dichte oder Dicke der

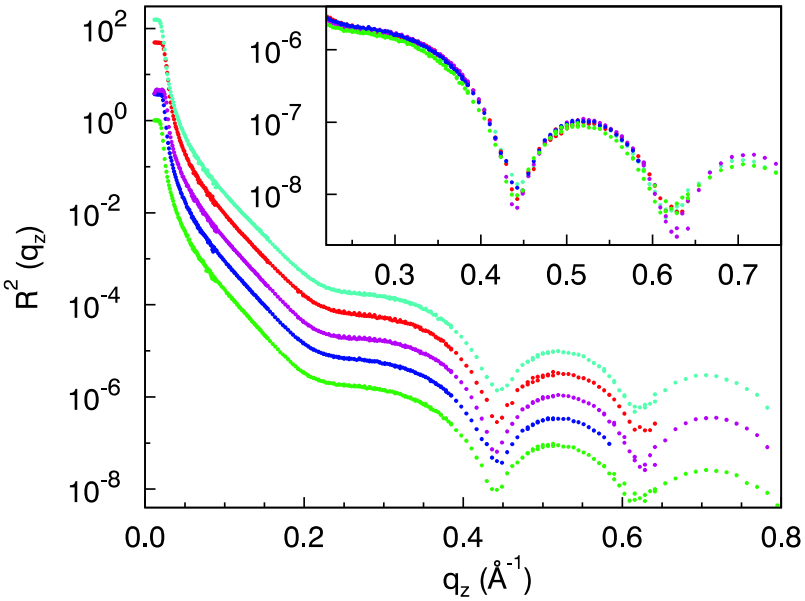

Abbildung 1.5: Röntgenreflektivität einer OTS-Schicht in Kontakt mit Wasser, welches mit verschiedenen Gasen gesättigt wurde (untere grüne Kurve: entgastes Wasser, blau: CO, violett: CO_2, rot: Ar, obere türkise Kurve: 0.5 M HCl). Die Datensätze wurden zur besseren Darstellung vertikal verschoben. Das Inset zeigt eine Vergrößerung des Messbereichs, in dem die Messmethode die höchste Empfindlichkeit für kleine Änderungen der Grenzflächenstruktur aufweist.

OTS-Schicht einhergehen, stören die gegenseitige Auslöschung der reflektierten Wellen und führen damit, analog zur Aufhellung in der klassischen Optik, zu einem deutlich sichtbaren Intensitätsanstieg. Abbildung 1.6 zeigt, dass sich innerhalb einer Zeitspanne von $50\,\mathrm{s}$ (Inkubationszeit), was in Wasser einer Strahlendosis von etwa $600\,\mathrm{kGy}$ entspricht, keine Veränderung bemerkbar macht. Danach jedoch lässt sich plötzlich ein deutlicher Anstieg der reflektierten Intensität feststellen.

Dieses Phänomen basiert auf der Erzeugung von OH-Radikalen im Röntgenstrahl. Die kurzlebigen und instabilen Radikale diffundieren an die Grenzschicht, wo sie mit der Alkylkette der OTS-Moleküle zu Alkohol oder deprotonierten Carbonsäuregruppen reagieren können. Solange diese Defekte genügend voneinander separiert sind, ergeben sich keine messbaren Veränderungen in der Röntgenreflektivität (Inkubationszeit). Wird aber eine gewisse Defektdichte überschritten, so treten die polaren bzw. geladenen Gruppen miteinander in Wechselwirkung, was zu Verzerrungen und Verschiebungen in der gesamten geordneten OTS-Schicht führt und sich daher in der gemessenen Intensität bemerkbar macht. Um sicherzustellen, dass alle Datenpunkte auf einem intakten Oberflächenbereich gemessen wurden, wurde die Probe zwischen jedem Messpunkt seitlich verschoben.

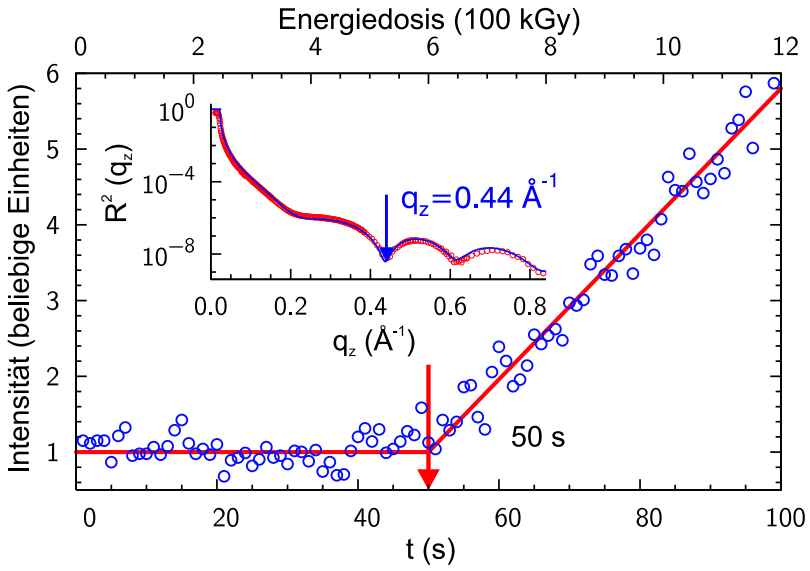

Abbildung 1.6: Zeitabhängige Variation der Röntgenreflektivität einer OTS-Probe in Wasser, gemessen bei einem Impulsübertrag destruktiver Interferenz ($q_z = 0.44\,\text{Å}^{-1}$, siehe Inset). Der Strahlenschaden macht sich nach einer Zeit von ungefähr $50\,\text{s}$ durch einen deutlichen Anstieg der reflektierten Intensität bemerkbar. Dies entspricht einer im Wasser absorbierten Energiedosis von $600\,\text{kGy}$ (obere Achse).

Diskussion

Die Analyse der Reflektivitätsmessungen an hydrophoben Wassergrenzflächen ergibt ein integrales Dichtedefizit von $d_\text{w}\,(\rho_{\text{H}_2\text{O}} - \rho_\text{w}) = 1.1\,\text{Å}\,\text{g}\,\text{cm}^{-3}$, welches weniger als einer halben Monolage von Volumen Wasser entspricht und sich über einen Bereich von bis zu zwei molekularen Wasserdurchmessern [23, 24] erstreckt (siehe Abb. 1.1). Aufgrund der begrenzten Auflösung der verwendeten Methode lassen sich aus diesen Messungen alleine jedoch keine eindeutigen Aussagen zur molekularen Wasserstruktur und deren Ursprungs treffen. Zusammen mit anderen experimentellen Methoden, numerischen Simulationen und theoretischen Modellen, liefern sie jedoch wichtige Informationen zum tieferen Verständnis von Wasser an hydrophoben Grenzflächen. Die Existenz einer derartigen Grenzschicht erniedrigter Dichte und vergleichbarer Dicke im Bereich einiger Å wurde sowohl in Molekulardynamiksimulationen [25–30] vorhergesagt, als auch durch indirekte Methoden [31] experimentell bestätigt. Spektroskopische Messungen (SFG) zeigen eine deutliche Ausrichtung der Wassermoleküle an hydrophilen [32, 33] und hydrophoben [34, 35] Grenzflächen. Im Gegensatz dazu lieferten frühere Neutronenstreuexperimente [36–38] an Wassergrenzflächen auflösungsbedingt weitaus größere Schichtdicken.

Chapter 2

Introduction

Motivation

The microscopic understanding of the interaction of water with hydrophobic and hydrophilic materials is of utmost importance for the quantitative description of the properties of water in natural and technological environments. All interfacial phenomena related to water, such as wetting, drying, or lubrication in confined geometries, crucially depend on the details of this interaction [7]. In biology, hydrophobic and hydrophilic interfaces affect the complex mechanism of protein folding and stability [5] as well as the formation of membranes [6]. However, the microscopic details of how water meets a hydrophobic interface are still not settled and in fact rather controversial. A particularly important aspect concerns the appearance of water density depletion at a solid interface. While molecular dynamic simulations became the major tool for predicting the structure of solid-water interfaces [30], for the two most fundamental parameters, the total density deficit, integrated across the interface, as well as the distance until the water at a hydrophobic wall reaches the bulk density, no reliable experimental numbers were published by 2004. Thus, the objective of this study was the accurate determination of these parameters by high-energy x-ray reflectivity experiments.

Outline of the Thesis

Following this introduction, the thesis continues with an overview on the properties of liquid bulk water and the theoretical description of a solid-liquid interface as well as previous experimental work done in this field. Chapter 4 gives a short introduction to x-ray reflectivity experiments and data analysis, with emphasis on deeply buried interfaces and high energy x-rays. Experimental details on the sample preparation and environment, the setup at the high energy beamline ID15A at the ESRF, and the x-ray reflectivity measurements can be found in chapter 5. The analysis and discussion of the experimental data is given in chapter 6. It largely follows the two papers which where published and prepared recently [39, 40] summarizing the results obtained from this study. In the subsequent outlook (Chapter 8) it is shown how this thesis is embedded in the research activities at the Max Plack Institute for Metals Research and which further interesting studies on this topic

could be done in the future. The thesis concludes with a conclussion and summary of the presented results (Chapter 7).

Articles on a popular science level reporting on the results obtained in this thesis, can be found in the press releases of the Max-Planck Society [20] and the European Synchrotron Radiation Facility [21], as well as in an essay published in the “Max Planck Forschung” magazine [22].

Chapter 3

Water at interfaces

This chapter provides an introduction on the physics of water at interfaces. In the first section, a brief overview on the properties of bulk water [2,41,42] is given focusing on the aspects essential for the discussion of this work's results. The preparation and properties of hydrophobic interfaces tailored for the high energy x-ray reflectivity experiments are discussed separately, followed by an theoretical description of solid-liquid interfaces and results from numerical simulations. With a summary and comparison of previous experimental work that was performed on hydrophobic water interfaces the chapter concludes.

3.1 Properties of bulk water

Many of the water properties are directly linked to its molecular arrangement. Figure 3.1a shows a sketch of the water molecule consisting out of one oxygen (red spheres) and two hydrogen (grey spheres) atoms. The H-O-H bond angle of $104.45°$ corresponds to an octahedral angle ($109.47°$) distorted by the two free electron pairs of the oxygen atom. In combination with the non-linear conformation, the difference in the electro-negativity

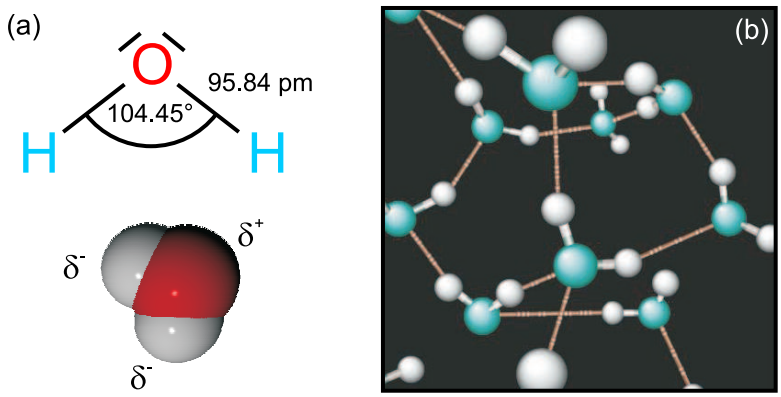

Figure 3.1: (a) Sketch of the water molecule. (b) Hydrogen bond network of water (taken from Chandler [4]).

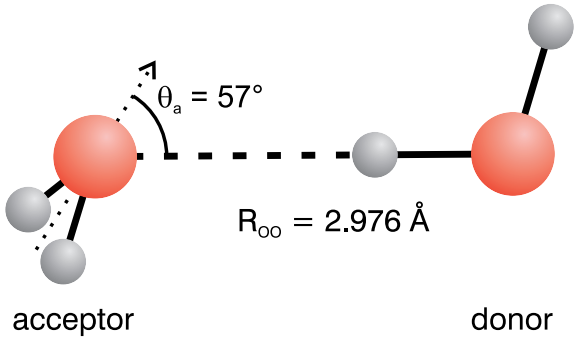

Figure 3.2: Sketch of the hydrogen bond formed by an isolated dimer consisting of two water molecules (large red spheres: oxygen; small grey spheres hydrogen atoms).

between hydrogen (2.20) and oxygen (3.44)[1] leads to a strong dipolar moment of $6.151 \cdot 10^{-30}\,\mathrm{Cm}$.

Each water molecule can participate in up to four hydrogen bonds by sharing its two associated hydrogen atoms with two neighboring molecules. With approximately $12\,\mathrm{kJ\,mol^{-1}}$ the binding energy of a hydrogen bond in water lies in between those of covalent bonds[2] and week VdW (Van der Waals[3] interactions. In liquid water this leads to a highly cross-linked hydrogen bond network as depicted in Fig. 3.1b [4, 43]. On average, every water molecules builds up three to four bonds arranged preferentially in a locally tetrahedral environment. This explains the strong internal interaction and thus the high surface tension ($72.8\,\mathrm{mN\,m^{-1}}$), the large evaporation heat ($40.7\,\mathrm{kJ\,mol^{-1}}$), and the elevated boiling point of water in comparison to similar compounds[4] such as H_2S. Detailed information on the properties of hydrogen bonds can be extracted from the microwave spectrum. Odutola et al. [44] determined the structure of an isolated water dimer (see Fig. 3.2 in a low temperature molecular beam. Since hydrogen bonding is a strongly correlated phenomenon, the distance between the oxygen atoms as well as the bond angle are influenced by other hydrogen bonds formed with neighboring water molecules.

Figure 3.3 shows the phase diagram of water[5]. In ordinary Ice Ih the oxygen atoms are placed in accordance to the hexagonal wurtzite structure. One hydrogen atom is sitting in between every two neighboring oxygen atoms in accordance to the Bernal-Fowler rules [46][6]. Following up this concept, in 1935 L. Pauling was able to explain the residual entropy in ice and other crystals with some randomness of atomic arrangement [47]. The atom positions in the unit cell were determined precisely by Röttger et al. [48] and Line et al. [49] with x-ray and neutron powder diffraction. They give an O-O distance between neighboring oxygen atoms of $2.75\,\text{Å}$, which is significantly smaller than the length of a

[1] Pauling electronegativity scale

[2] Typical bond enthalpies for covalent single bonds are in the range of $150 - 500\,\mathrm{kJ\,mol^{-1}}$.

[3] Johannes Diderik van der Waals (1837-1923), Dutch scientist.)

[4] The boiling point of H_2S is $-60.7\,^\circ\mathrm{C}$ although the molecular mass is nearly doubled.

[5] Today, the phase diagram of water contains 15 established phases of crystalline ice [42, 45] and at least 2 solid amorphous phases. For simplicity, these different solid phases are not shown in Fig. 3.3.

[6] The hydrogen atoms are placed asymmetrically in between the oxygen atoms. They form a structure locally fulfilling the so-called ice-rules, exhibiting no long-range correlations in the hydrogen positions

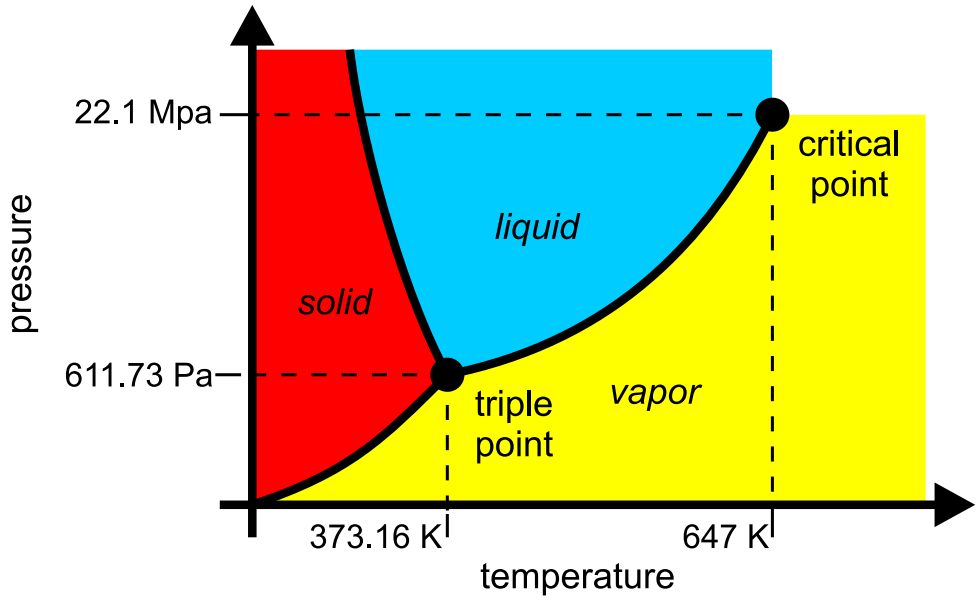

Figure 3.3: Schematic phase diagram of water in vicinity of ambient conditions.

hydrogen bond in the water dimer.

By crossing the melting curve, water transforms from the solid to the liquid phase. Here, an irregular behavior – the melting point depression at increasing pressure[7] – occurs[8]. One standard approach to gain information about the internal structure of liquids are x-ray and neutron scattering methods [53]. In Fig. 3.4, the scattered x-ray intensity from a bulk water sample is shown[9]. The average separation of neighboring molecules can be roughly estimated from the peak position of the first maximum in the scattered intensity at $q = 2.02\,\text{Å}^{-1}$ to $2R \approx 2\pi/q \approx 3.1\,\text{Å}$. Quantitative scattering experiments were performed using x-rays [24, 55, 56] and neutrons [23]. From the oxygen–oxygen correlation function $g_{OO}(r)$, the Fourier transform of the partial liquid structure factor $S_{\text{OO}}(q)$, both x-ray and neutron scattering experiments give a value of approximately $2R = 2.8\,\text{Å}$ for the average distance between two nearest water molecules. By small-angle x-ray and neutron scattering Bosio et al. and Xie et al. [57–59] determined the correlation length of bulk water to $\xi = 4 - 8\,\text{Å}$, i.e. approximately two molecular diameters of water.

[7] Via the Clapeyron equation $\mathrm{d}p/\mathrm{d}T = \Delta S/\Delta V$, the negative slope of the melting curve is directly related to the volume increase ΔV when water freezes.

[8] It is one of the most prominent examples for the deviation of water properties from those of simple liquids [50, 51] caused by its complex tetrahedral hydrogen bond network [52]. Other intriguing anomalies of the response functions are the maximum density of liquid water at $4\,^{\circ}\text{C}$, the thermal expansion coefficient, the heat capacity, and the isothermal compressibility.

[9] The measurement was performed at the high energy beamline ID15A, ESRF, Grenoble. For a quantitative analysis, absolute normalization of the scattering data is required in order to obtain a meaningful result. In the setup used, adherent systematic errors prevent in this case a high quality data analysis.

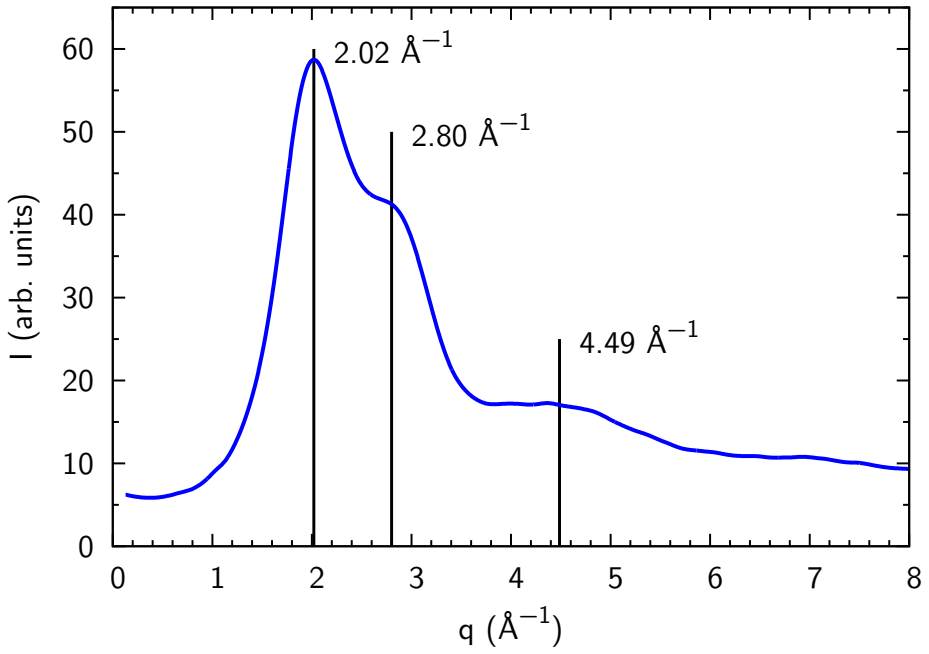

Figure 3.4: Scattered x-ray intensity from a bulk water sample versus momentum transfer.

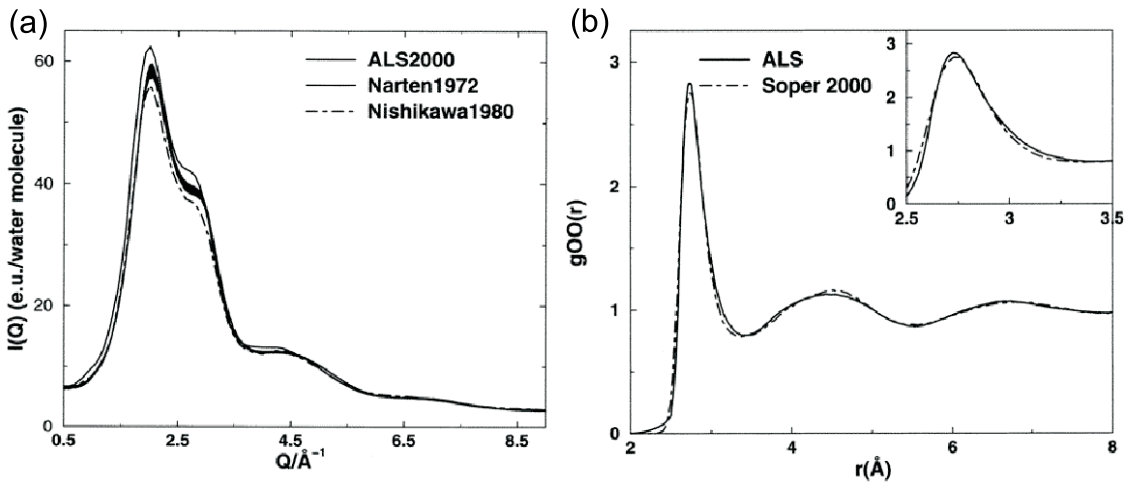

Figure 3.5: Water structure at ambient conditions ($25°\mathrm{C}$, $1\,\mathrm{atm}$) from scattering experiments (compilation from Head-Gordon et al. [54]). (a) Comparison of experimental x-ray scattering data from Hurra et al. [24] (thick solid line), Narten [55] (thin solid line), and Nishikawa et al. [56] (dot-dash line). (b) Oxygen–oxygen correlation function $g_{\mathrm{OO}}(r)$ calculated from x-ray (solid line [24]) and neutron (dot-dash line [23]) scattering data.

3.2 Hydrophobic interfaces

In order to study the intrinsic interfacial structure of water at a hydrophobic interface on a molecular level by x-ray reflectivity, the preparation of well-defined substrates is essential. They have to be flat on a microscopic level influencing both the liquid-wall interaction and the accessible q-range (see 4.2.5). In addition, smoothness on a cm length scale is required by the employed high energy scattering techniques (see Sec. 4.1.3). Their hydrophobic surface properties have to be homogeneous over several mm for reproducible experiments, and a comparison of the microscopic observations with macroscopic quantities such as the contact angle.

Hydrophobic inorganic interfaces are for example provided by hydrogen-terminated silicon in (111) orientation. At ambient conditions, this surface is relatively stable with respect to oxidation when kept under water at. However, under the intense x-ray beam the surface gets rapidly oxidized, exposing strongly hydrophilic silanol (Si-OH) and silicilic acid (Si-O^-) groups to the water interface.

Hydrophobic water interfaces can also be studied at liquid-liquid interfaces[10]. Here, non-polar liquids immiscible with water (e.g. hexane or perfluorohexane) serve as the hydrophobic liquid phase. Due to the presence of capillary waves at liquid-liquid interfaces, the accessible q-range is limited to approximately $0.3\,\text{Å}^{-1}$ [61], which is insufficient for the extraction of real space structures on a molecular level[11].

3.2.1 Organic solid-liquid interfaces

In the group of organic molecules, a broad spectrum of materials with hydrophobic surface properties can be found. All long chain alkanes are hydrophobic non polar molecules leading to a low surface free energy (SFE) γ[12]. Even smaller values of γ can be achieved by substituting hydrogen with fluorine atoms. Perfluorinated materials such as PTFE (Teflon) or PFA[13] , which are used for coatings on pans or for instruments operating in harsh chemical environments, are well known for their hydrophobicity and chemical stability.

All these organic materials are inherently ductile, compared to single crystalline substrates made from semiconductors or metal-oxides such as like silicon, quartz (SiO_2), or sapphire (Al_2O_3). Therefore, it is impossible to prepare flat samples[14] with a RMS rough-

[10] For scattering experiments on liquid interfaces, the x-ray beam must be tilted to keep the sample horizontally while varying the incident angle. At ID15A, this option is available by using the HEMD setup in combination with the liquid monochromator [60].

[11] First experiments on liquid-liquid interfaces were performed in parallel to this work. They showed that the setup at ID15A is highly competitive with other state of the art liquid reflectometers.

[12] Polymers like Polyethylene (PE) and Polypropylene (PP) have surface free energies of $\gamma = 35\,\text{mN}\,\text{m}^{-1}$ and $\gamma = 30\,\text{mN}\,\text{m}^{-1}$, respectively with negligible polar contributions (see Sec. 3.3.1).

[13] The SFE of PTFE is $\gamma = 22.5\,\text{mN}\,\text{m}^{-1}$ (PFA $22\,\text{mN}\,\text{m}^{-1}$) leading to a water contact angle of about 120°.

[14] The variation in the incident and exit angle $\Delta\alpha$ over the beam footprint l on the sample should not exceed the vertical beam divergence β_v (see Sec. 5.4.2 and Sec. 5.1.2). For a spherical sample with radius R the incident angle on different positions of the sample varies by $\Delta\alpha = \frac{l}{R}$.

ness σ_{RMS} in the order of a few angstrom by polishing a piece of bulk material. One solution is to cover a rigid solid substrate such as silicon or glass with a thin layer of typically several hundred nm thickness of the desired hydrophobic substance.

Polymer thin films

Polymer thin films can be deposited on solid substrates by either spin or dip coating. Here the polymer, dissolved in a solvent, is dispersed homogeneously on the substrate by dipping it into the solution or putting a droplet of the solution onto the substrate during rapid rotation. After solvent evaporation, the sample can be annealed to produce a smooth film of homogeneous thickness. Long polymer chains with a typical diameter of 2-$5\,$Å, given by the chemical bond length and angles within the polymers, are used to grow these films. In an amorphous polymer, chains are oriented randomly and overlap each other similar to spaghetti. Intuitively, this leads to pockets between neighboring chains and to a minimal roughness, which is at least a multiple of the chain diameter, i.e. approx. $10\,$Å. The properties of the interfacial water molecules near such a structured wall with a length scale of the average OO distance in water, may differ significantly from the ones at a smooth wall [7,62]. Polymer thin films are therefore not an ideal substrate for experiments addressing the intrinsic properties of hydrophobic solid-liquid interfaces. Nevertheless they are widely used in neutron reflectivity studies [36,63] and AFM experiments [18] on hydrophobic water-solid interfaces.

3.2.2 Self assembled monolayers

Beside thiol based self assembled monolayers (SAMs), molecules with a silane anchor group are prevalent for the preparation of hydrophobic surfaces. Their advantage is that they bond covalently to the substrate and are therefore very stable after deposition. SAMs with a silane anchor group can be prepared either from the vapor phase or from solution. The basic reaction scheme, however, is equivalent. As an example, Fig. 3.6 shows the schematic anchoring reaction of octadecyl-trichlorosilane (OTS) on OH-terminated surfaces. The OTS molecules, strongly diluted in an organic solvent[15] , get hydrolyzed under dissociation of HCl[16] by trace amounts of water present in the deposition solution. These hydrolyzed molecules are adsorbed via hydrogen bonds to the OH-terminated native silicon oxide, quartz, or glass substrate. In the last step, the silane molecules are covalently bonded to the substrate by water condensation. A high degree of cross-linking by polymerization between neighboring molecules is achieved by thermal annealing at approximately $110\,^{\circ}\mathrm{C}$ after removal from the deposition solution. For a detailed recipe for the OTS-SAM preparation see Sec. 5.3.2.

Figure 3.7a shows an AFM measurement of an OTS-SAM from Fujii et al. [64]. Hexagonal arrangement of the alkyl chains is indicated by the local symmetry of the bright

[15] Typical silane concentrations are in the mM regime.

[16] When alcoxy-silanes are used instead of choro-silanes, the by-products of the anchoring reactions are the corresponding alcohols.

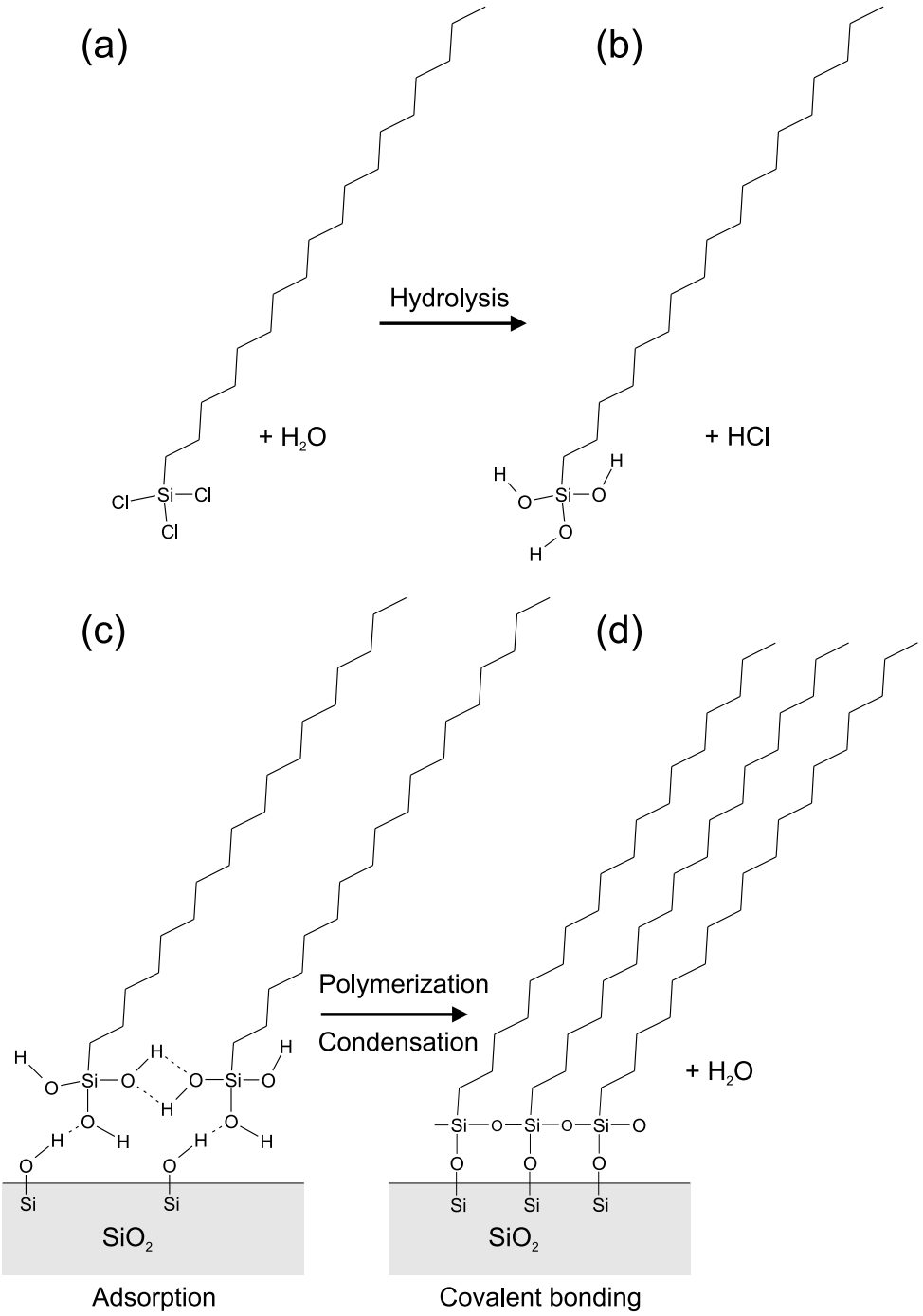

Figure 3.6: Anchoring reaction of the octadecyl-trichlorosilane SAM. The OTS molecule (a) is hydrolyzed by trace amounts of water in the deposition solution (b). After adsorption at the SiO_2 substrate (c) the OTS molecules are covalently bound and cross-linked by H_2O condensation (d).

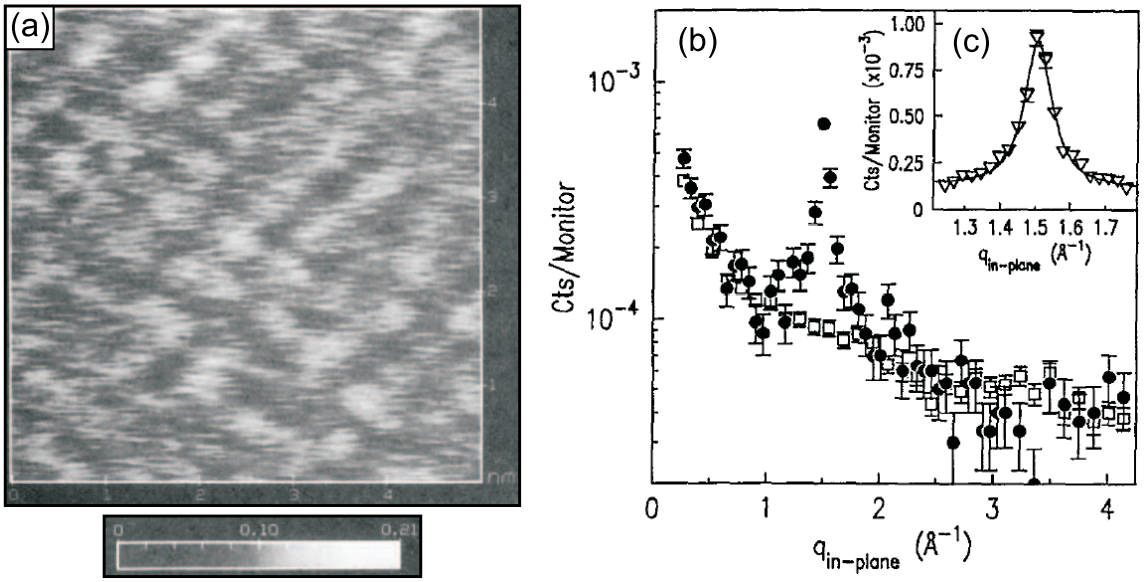

Figure 3.7: (a) AFM measurement on an OTS-SAM on SiO_2 taken from Fujii et al. [64]. (b) GID signal of an uncoated (open squares) and OTS-coated (filled circles) silicon waver taken from Tidswell at al. [65]. The inset (c) shows a magnification at the peak position together with a Lorenzian fit (solid line).

spots. A detailed analysis reveals an average area of $23\,\text{Å}^2$ per OTS molecule [66]. Tilting of the anchored molecules leads to an ellipsoidal shape of the terminal methyl groups, sticking out of the tightly packed layer by approximately $2\,$Å. This AFM data is in agreement with x-ray grazing incidence diffraction (GID) experiments performed by Tidswell at al. [65] (see Fig. 3.7b). The position of the GID peak at $1.5\,\text{Å}^{-1}$ corresponds to an average distance of $4.2\,$Å between neighboring chains. By assuming single hexagonal packing an area of $20\,\text{Å}^2$ per anchored molecule can be estimated. As expected, these values give a slightly less dense packing compared to single crystalline long chain alkanes [67, 68].

From AFM and SFG studies reported in literature it is well known that OTS-SAMs on SiO_2 do not always form homogeneous and smooth monolayers but islands or polymer-like inhomogeneous layers with a surface roughness in the nm regime [69, 70]. Important preparation parameters are, amongst others, the water content in the deposition solution or the concentration of OTS in the solvent. More details on the preparation of OTS self assembled monolayers can be found in Sec. 5.3.2.

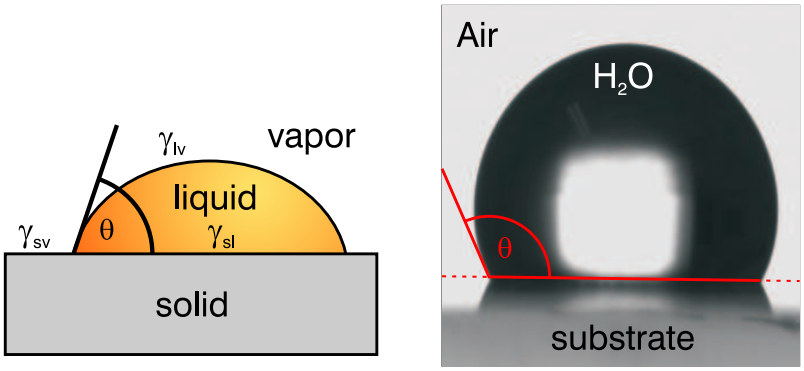

Figure 3.8: The contact angle θ at the three phase contact line of a liquid droplet on top of a solid substrate is determined by the interfacial tensions γ_{sv}, γ_{lv}, γ_{sl}. Schematic view (left), and contact angle measurement of water on top of a hydrophobic substrate (right). The dashed red line indicates the substrate surface. On the lower side, the mirror image of the droplet is clearly visible.

3.3 The solid-liquid interface – Theoretical description

3.3.1 Interfacial tension and contact angle

The interaction between two neighboring materials (A,B) at an interface can be described by their interfacial tension γ_{AB}. The corresponding phases can be either solid (s), liquid (l), or gaseous (v). When one of the two phase is gaseous, also the term surface tension with the formula symbol σ is used. Quantitatively, γ_{AB} describes the energy which has to be applied in order to create a unit area of the A-B interface. When a liquid drop is sitting on top of a solid support as it is shown in Fig. 3.8, the contact angle θ is determined by the ratios of the interfacial tensions of the areas meeting at the three phase contact line. Minimizing the energy of the system (mechanical equilibrium), yields Young's equation [17]

$$\cos\theta = \frac{\gamma_{\mathrm{sv}} - \gamma_{\mathrm{sl}}}{\gamma_{\mathrm{lv}}}\,, \tag{3.1}$$

linking the interfacial tensions to the contact angle θ. Descriptively, θ depicts whether the liquid *likes* or *dislikes* the solid. Therefore, solid surfaces exhibiting a contact angle with respect to water which is larger than 90° are called hydrophobic ($\gamma_{\mathrm{sv}} < \gamma_{\mathrm{sl}}$), whereas materials with $\theta < 90°$ are called hydrophilic ($\gamma_{\mathrm{sv}} > \gamma_{\mathrm{sl}}$).

The origin of the interfacial tension describing the macroscopic contact angle are forces acting on a molecular level between the two phases in contact with each other. For the further discussion, these forces can be separated into a contribution from dispersive

[17] Thomas Young (1773-1829)

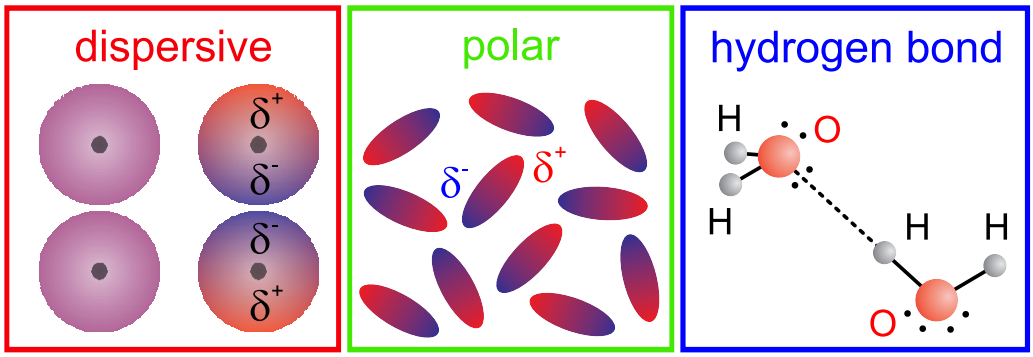

Figure 3.9: Sketch of the molecular forces contributing to the interfacial tension.

VdW, γ^{D}) and polar (γ^{P}) interactions plus hydrogen bonding (γ^{H}).

$$\gamma = \gamma^{\mathrm{D}} + \gamma^{\mathrm{P}} + \gamma^{\mathrm{H}} \tag{3.2}$$

In contrast to dispersive VdW forces, applying to all atoms and molecules, polar interaction and hydrogen bonding depend strongly on the molecular arrangement (see Fig. 3.9). The intermolecular forces of the polar water molecule are for example dominated by the strong hydrogen bonds while aliphatic hydrocarbons interact only via the weak dispersive forces. By analysis of experimental data and inspired by an earlier work of Fowkes [71], Owens and Wendt [72] showed that in many cases the interfacial tension between two phases can be calculated by

$$\gamma_{\mathrm{AB}} = \gamma_{\mathrm{A}} + \gamma_{\mathrm{B}} - 2\left(\sqrt{\gamma_{\mathrm{A}}^{\mathrm{D}}\gamma_{\mathrm{B}}^{\mathrm{D}}} + \sqrt{\gamma_{\mathrm{A}}^{\mathrm{P}}\gamma_{\mathrm{B}}^{\mathrm{P}}} + \sqrt{\gamma_{\mathrm{A}}^{\mathrm{H}}\gamma_{\mathrm{B}}^{\mathrm{H}}}\right) . \tag{3.3}$$

Here, the various forces acting in the two materials interact only with the same types. In the formula, this is expressed by summing up the geometric means of the relevant contributions. Therefore, Eq. (3.3) reflects the idea of sorting materials in hydrophilic and hydrophobic or lipophilic and lipophobic categories. When both phases dominantly interact via the same type of forces, the interfacial energy decreases due to the cross terms and the liquid wets the surface. In analogy, two liquids exhibit a mixing tendency for like interactions (e.g. water and formic acid) whereas phase separation occurs for unlike forces (water and hexane). Thus, by measuring the contact angle of a solid in contact with different probe liquids with known molecular interactions, one gains information about its surface chemistry.

3.3.2 Density Functional Theory of classical fluids

For a deeper understanding and interpretation of the x-ray scattering data, which is discussed in detail in Sec. 6, R. Roth[18] developed a simple Density Functional Theory (DFT)

[18] Dr. Roland Roth, Max Planck Institute for Metals Research, Department: Theory of inhomogeneous condensed matter, Roland.Roth@mf.mpg.de

model to calculate the density distribution of a classical square well fluid adjacent to a solid interface. Details on DFT in classical fluids can be found in the work of Evans and Swol [73–75].

The liquid system, which can undergo a phase transition, is considered in the grand canonical ensemble with the system volume V, temperature T, and chemical potential μ fixed. Taking into account these constraints, the corresponding thermodynamic potential is the grand canonical potential Ω. In an unconfined bulk system Ω is given by

$$\Omega_{\mathrm{bulk}} = -p_{\mathrm{l}} V \,, \tag{3.4}$$

with the pressure p_{l} in the liquid. Introducing a solid wall to the system extends Eq. (3.4) by the interfacial energy term $\gamma_{\mathrm{sl}} A$ (solid s, liquid l) to

$$\Omega_{\mathrm{wall}} = -p_l V + \gamma_{\mathrm{sl}} A \,. \tag{3.5}$$

In the DFT ansatz, the corresponding functional of the density distribution in the liquid $\rho\,(z)$[19] is given by

$$\Omega\left[\rho\,(z)\right] = F\left[\rho\,(z)\right] + \int_{z=0}^{\infty} \mathrm{d}z \rho\,(z)\left[V_{\mathrm{ext}}\,(z) - \mu\right] . \tag{3.6}$$

Here, the first term $F\left[\rho\,(z)\right]$ describes the internal interaction within the fluid while $V_{\mathrm{ext}}\,(z)$ takes into account the external interaction of the liquid with the wall. The internal interaction of the fluid can be divided in tree parts:

$$F\left[\rho\,(z)\right] = F_{\mathrm{IG}}\left[\rho\,(z)\right] + F_{\mathrm{HS}}\left[\rho\,(z)\right] + F_{\mathrm{AT}}\left[\rho\,(z)\right] \tag{3.7a}$$

$$F_{\mathrm{IG}}\left[\rho\,(z)\right] = \int \mathrm{d}z \rho\,(z)\left[\ln \lambda^3 \rho\,(z) - 1\right] \tag{3.7b}$$

$$F_{\mathrm{AT}}\left[\rho\,(z)\right] = \int \mathrm{d}z \int \mathrm{d}z' \rho\,(z)\,\rho\,(z')\,V_{\mathrm{AT}}\left(|z - z'|\right) \tag{3.7c}$$

F_{IG} denotes the contribution of an ideal gas with the thermal wavelength $\lambda = \frac{2\pi\hbar}{\sqrt{2\pi m k_{\mathrm{B}} T}}$. The second term takes into account the excluded volume of the hard spheres, which corresponds to the *co-volume* b in the VdW equation of state[20]. For the existence of a solid-liquid phase transition, an attractive interaction V_{AT} between the particles is essential. This is included by F_{AT} corresponding to the *binnendruck* a in the VdW equation. Numerical minimization of Eq. (3.6) with respect to the density distribution $\rho\,(z)$ gives solution for the grand canonical potential Ω_{wall} of Eq. (3.5) and the interfacial profile of the liquid at the wall.

The water-water interaction can be modeled with a square well potential. In order to determine appropriate parameters for the fluid-fluid (model) interactions, certain values

[19] For simplicity, the spacial coordinates parallel to the interface are omitted.

[20] The expression for F_{HS} is much more complicated than the expressions shown in Eq. (3.7b) and Eq. (3.7c). Details can be found in the work of Roth [76].

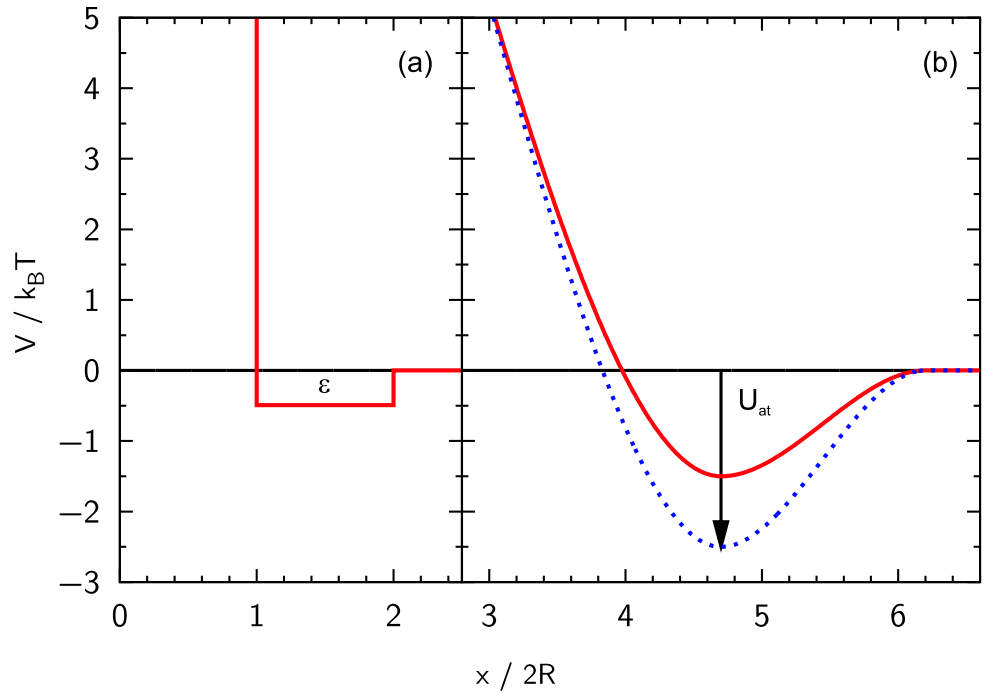

Figure 3.10: (a) Hard sphere potential for the water-water interaction including the attractive part V_{AT}. (b) Water-wall interaction V_{ext} for a hydrophilic ($\Theta = 80°$, dashed blue line) and a hydrophobic wall ($\Theta = 120°$, solid red line)

deduced from Ω have to match the experimental data. The radius of the hard spheres can be chosen to $2R = 2.8\,\text{Å}$ in accordance to the average distance between two molecules in bulk water (see Sec. 3.1). The packing fraction of the spheres is given by

$$\eta = \frac{NV_0}{V_N} = \rho_{\mathrm{mol}} \frac{4\pi}{3} R^3 = 0.38 \tag{3.8}$$

and fixed by the molar density of water ($\rho_{\mathrm{mol}} = 55\,\mathrm{mol\,l^{-1}}$). Another condition is that the distance $\Delta\rho = \rho_{\mathrm{l}} - \rho_{\mathrm{cl}}$ between the density of the liquid ρ_{l} and the density ρ_{cl} at the liquid–vapor coexistence line in the T–ρ diagram has to reproduce the experimental value. Since the isothermal compressibility[21] of liquid water at room temperature is very low, $\Delta\rho = 5 \cdot 10^{-5}\mathrm{g\,cm^{-3}}$ is a rather small quantity. Figure 3.10a shows the water-water interaction potentials which was used for the DFT calculations, matching the boundary conditions discussed above. The depth of the attractive part in the square-well is $\varepsilon = 0.49\,k_{\mathrm{B}}T$ with total extent of $R_{\mathrm{sw}} = 2R = 5.6\,\text{Å}$. The liquid-wall interaction shown in Fig. 3.10b was modeled by an attractive potential with a depth of $U_{\mathrm{at}} = 1.5\,k_{\mathrm{B}}T$ for the hydrophobic wall (contact angle $\Theta = 120°$, solid line) and $U_{\mathrm{at}} = 2.5\,k_{\mathrm{B}}T$ (vertical arrow) for the hydrophilic wall (contact angle $\Theta = 80°$, dashed line). The slope of the liquid-wall potential for small distances (repulsive part) was chosen such that it mimics an atomic roughness.

[21] The bulk modulus of liquid water at $4\,°\mathrm{C}$ is $2.06 \cdot 10^9\mathrm{Pa}$

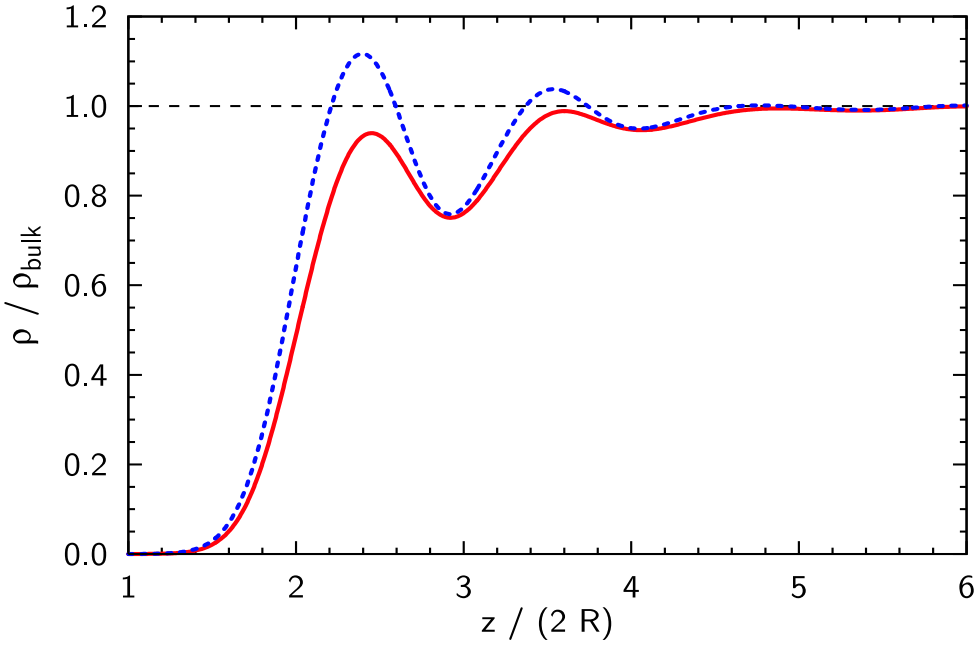

Figure 3.11: Density profiles of a square-well fluid at a hydrophobic ($\Theta = 120^{\circ}$, dashed line) and at an hydrophilic wall ($\Theta = 80^{\circ}$, solid line). The horizontal dashed line denotes the bulk density.

As an illustration, Fig. 3.11 shows the density profiles of this square-well fluid close to a hydrophobic (solid line) and a hydrophilic wall (dashed line) obtained by density functional theory. Both profiles exhibit a smooth decay towards vanishing density close to the interface and an oscillatory structure at small separations from the wall. After approximately $6\,$Å the density approaches asymptotically the bulk value. The decay length of the density modulations is of the order of twice the correlation length of bulk water ($\xi = 4\,$Å) [23]. Similar behavior was also found experimentally by Cheng et al. on hydrophilic mica surfaces[22] [77]. An open question is as to which extent a simple DFT model with a generic water-water interaction potential can describe the phenomena at a solid-water interface correctly. During the last decades, the predominant opinion in the scientific water community was that theoretical approaches on the water-solid interface have to be based on molecular dynamic (MD) simulations, incorporating all the details of the water interaction potential. Today, it seems that also continuous models with model potentials adjusted to the correct contact angle (i.e. the ratio between the surface and interfacial tension) can explain many of the relevant interfacial phenomena.

[22] Since the mica surface immersed in water is electrically charged the results can not directly be compared with each other.

3.3.3 Molecular dynamic simulations

Another theoretical approach to gain information on the microscopic structure at solid-liquid interfaces is based on MD simulations. Supported by the rapid increase in computer power during the last decades they became a major tool to predict the structure and dynamics of water at interfaces [25–29, 78]. However, the complex nature of the polar water molecules leads to complicated interaction potentials. Small details on the employed force model may result in remarkable differences in the calculated density profiles which can explain the different results published. MD simulations have shown that beside the liquid-wall interaction curvature effects play also an important role [62]. The interfacial structure of water in contact with small objects of nanometer size (pores or small particles) and its thermodynamic properties are quite different from the water structure at flat extended surfaces [79, 80].

Recently, an extensive study by Janecec and Netz of interfacial water at hydrophobic and hydrophilic surfaces, has revealed many details on the orientation and density distribution at solid-water interfaces [30]. Figure 3.12 shows a snapshot of the simulation box together with the laterally averaged density deficit function. The observed density oscillations of the liquid close to the interface agree qualitatively with the DFT results discussed in Sec. 3.3.2. A particular interesting result of this study is shown at the bottom of Fig. 3.12. The contact angle θ of the water seems to be in an universal relation with the interfacial density depletion. This gives a direct connection between a macroscopic quantity and the associated interfacial structure on a molecular level.

3.4 The solid-liquid interface – Experimental results

Since the interfacial structure of water at hydrophilic and hydrophobic solid-water interfaces is of fundamental interest, different experimental techniques have been employed in order to study their properties. Many surface science techniques (e.g. electron and ion scattering) require UHV conditions. Since the vapor pressure of water at ambient temperature is around $30\,\mathrm{mbar}$ these techniques are not applicable for experiments involving water. Studies at cryogenic temperatures [81] and on adsorbed monomolecular layers [82–84] cannot be compared with solid interfaces to bulk water. Therefore, these experiments are not discussed in this thesis. An overview of the experimental work performed on water-vapor and water-solid interfaces can be found in the review article of Verdauger et al. [85] published in 2006.

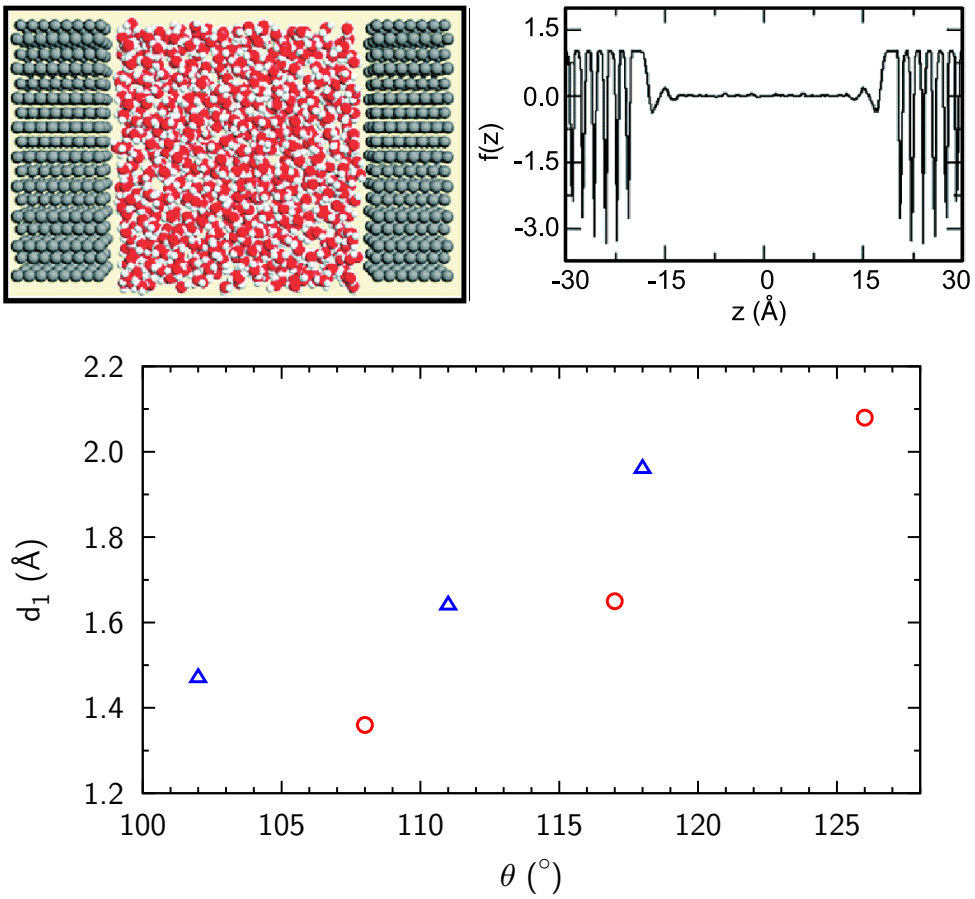

Figure 3.12: Results from MD simulations compiled from the work of Janecec and Netz [30]. (top left) Snapshot of the simulation box. (top right) Density deficit function $f(z) = 1 - \rho_{\mathrm{w}}(z)/\rho_{\mathrm{w}}^{\mathrm{bulk}} - \rho_{\mathrm{s}}(z)/\rho_{\mathrm{s}}^{\mathrm{bulk}}$ of a water slab between two hydrophobic substrates ($\Theta = 111^{\mathrm{o}}$). (bottom) Depletion thickness d_1 as a function of the contact angle θ for tetragonal (circles) and hexagonal arrangements of sites (triangles) in the solid phase.

3.4.1 Scattering techniques

Ellipsometry

Ellipsometry is the corresponding scattering technique to x-ray reflectivity in the optical wavelength regime. In contrast to x-ray scattering methods, additional information is obtained by analyzing the polarization dependence of the reflected wave. Similar to reflectivity, it is a very sensitive technique for the detection of interfacial structures on the length scale of the wavelength used. From layers much smaller than the optical wavelength, only the product of the refractive index difference to the substrate and the layer thickness can be determined.

While in the work of Castro et al. [86] a gas-like layer of 5 Å to 10 Å was detected at the

polystyrene-water interface, Mao et al. [87], and more recently Takata et al. [88] found no indications of a density depletion at hydrophobic water interfaces. However, the authors claim an experimental resolution allowing for an integrated density deficit corresponding to $1\,\text{Å}\,\text{g}\,\text{cm}^{-3}$.

Neutron reflectivity

Scattering techniques such as x-ray and neutron reflectivity are directly sensitive to the interfacial scattering length density profile at an interface. A big advantage of neutron over x-ray scattering techniques is that in many systems the scattering contrast can be tuned by changing the isotope ratio of the sample. Furthermore, the absorption of neutrons is very small in many materials and in the energy range relevant for reflectivity experiments (typically $4 - 5\,\text{Å}$)[23]. Therefore, neutron scattering methods might be seen as ideal tools to probe deeply buried structures and interfaces. The main disadvantage, however, is the low neutron flux and the high background signal, limiting the dynamic range to 5-6 orders of magnitude compared to 9 orders in a standard x-ray reflectivity study at a 3rd generation synchrotron source. This restricts the accessible q-range and therefore the real space resolution.

Figure 3.13 shows the results of a recent neutron reflectivity study performed by Doshi et al. [38]. The observed density profiles across the hydrophobic OTS-water interface exhibit an interfacial region of vanishing water density with a thickness between $2\,\text{Å}$ and $11\,\text{Å}$, depending strongly on the water preparation. The extracted information on the interfacial structure observed in various other neutron reflectivity experiments on hydrophobic substrates is quite inconsistent and sometimes unphysical. The width of the depletion zone ranges from no gap [63] over $20\,\text{Å}$ regime [37] up to several nanometers [36]. In a very recent paper from Maccarini et al. [89], the temperature dependence of the interfacial gap was studied, and an increase in the depletion distance from $D = 1.40\,\text{Å}$ at $6\,^{\circ}\text{C}$ to $1.73\,\text{Å}$ at $50\,^{\circ}\text{C}$ was found. In contrast to these studies, no interfacial gap was found in a recent work by Seo et al. [63].

X-ray reflectivity

Unlike to neutron reflectivity studies there are only a few publications on x-ray scattering experiments at hydrophobic solid-water interfaces. In 2003 Jensen et al. [27] studied the interface at a paraffin monolayer floating on top of bulk water. Due to the intrinsic capillary roughness at liquid surfaces, their spatial resolution is limited giving an upper limit of $15\,\text{Å}$ for the interfacial gap width. The quantity that could be determined very precisely was the integrated density deficit $D = d_{\text{w}}\,(\rho_{\text{H}_2\text{O}} - \rho_{\text{w}})$. Depending on temperature, values between $D = 0.8$ and $1.5\,\text{Å g cm}^{-3}$ were found, corresponding very well to the results obtained within this thesis [39], which was the first published x-ray reflectivity study on

[23] Strongly absorbing hydrogen ^{1}H has to be replaced with deuterium ^{2}D where the incoherent neutron scattering is negligible, when bulk material is penetrated.

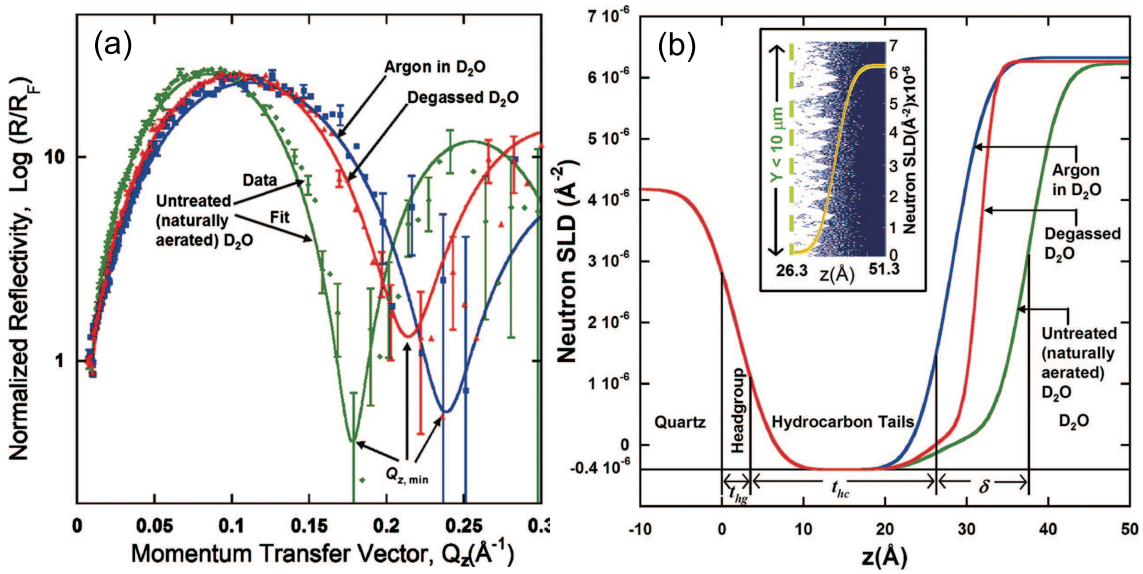

Figure 3.13: Neutron scattering experiments at the OTS–water (D_2O) interface (compilation from Doshi et al. [38]). (a) Neutron reflectivity R normalized by the Fresnel reflectivity R_F together with calculated curves (solid lines) from the parameter refinement of a slab model versus the vertical momentum transfer q_z. Doshi et al. found a strong dependence on the gas content in the water (naturally, green; degassed, red; argon, blue). (b) Scattering length density (SLD) profiles obtained from the neutron reflection pattern. The extracted structure depends highly on the water preparation.

hydrophobic bulk solid-liquid interfaces. In the work of Poynor et al. [90] an integrated gap size of approximately $2\,\text{Å g cm}^{-3}$ was found.

Density oscillations of interfacial water adjacent to hydrophilic mica surfaces were observed by Cheng et al. in 2001 employing x-ray reflectivity [77]. Measuring the specular rod up to $5.5\,\text{Å}^{-1}$, structural information with Å resolution could be observed. The mica surface immersed in water is negatively charged leading to adsorption of H_3O^+ ions at the solid-liquid interface. Therefore, their results cannot be compared directly with the findings on neutral interfaces. In 2004 Geissbühler et al. investigated the three-dimensional structure of the calcite-water interface by surface X-ray scattering [91]. They show that the molecules of the first two water layers arrange in ordered lattice created by the interacting with the calcite surface. Toney et al. investigated the voltage dependent ordering of water molecules on a silver electrode by x-ray scattering [92]. They interpret the significantly altered electron density profile for positively and negatively charged electrode-electrolyte interfaces by orientational ordering of dipole moment from the water molecules adjacent to the silver electrode.

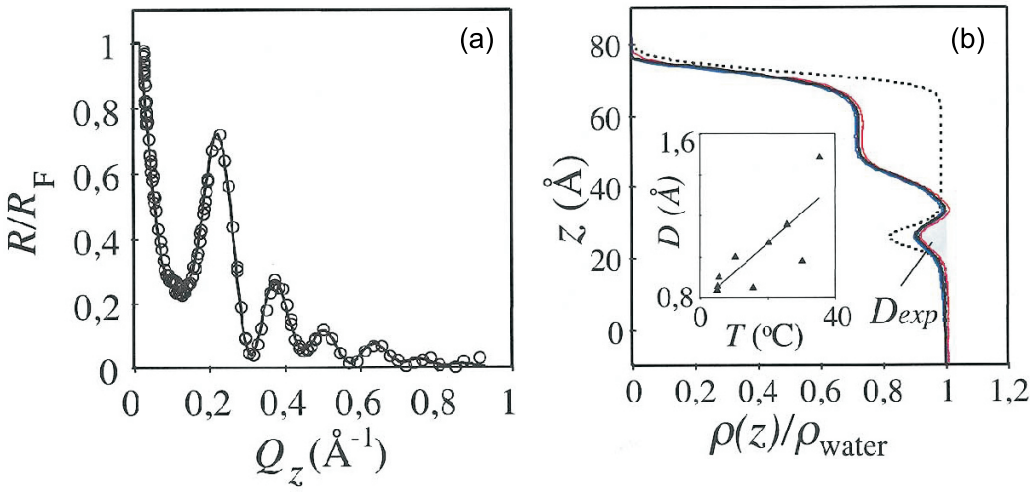

Figure 3.14: Compilation of a x-ray reflectivity experiment by Jensen et al. [27], addressing the structure of a paraffin monolayer on water. (a) X-ray reflectivity normalized by Fresnel reflectivity. (b) Vertical density profile calculated from parameter refinement of a slab model. The inset shows the integrated density deficit D versus the temperature.

3.4.2 Non-scattering techniques

Sum frequency generation spectroscopy

Sum frequency generation (SFG) spectroscopy provides insight in the molecular orientation at an interface. Therefore, it offers complementary information to x-ray reflectivity measurements essentially insensitive to the light hydrogen atoms. An overview on SFG studies of water at hydrophilic as well as hydrophobic interfaces can be found in the review articles of Hopkins et al. [93] and Shen et al. [33]. Summarizing the main features, the SFG signal from the OH-bonds at an interface can be separated into a liquid-like (hydrogen bond disordered structure, broad peak at $\approx 3400\,\mathrm{cm}^{-1}$) and an ice-like (hydrogen bond ordered structure, broad peak at $\approx 3200\,\mathrm{cm}^{-1}$) component plus the contribution from free dangling hydrogen bonds (sharp peak at $\approx 3680\,\mathrm{cm}^{-1}$). On hydrophilic surfaces, the interfacial structure was found to depend significantly on the specific substrate and the pH reflecting protonation and surface charge as well as quasi-epitaxial lattice matching of the partially ordered water with the substrate [32,94]. However, a common feature for all SFG spectra recorded from hydrophilic substrates is the absence of the sharp peak originating from the dangling hydrogen bonds.

Figure 3.15 shows SFG spectra from measurements at water interfaces performed by Du et al. [35]. The spectra from both the hydrophobic water-OTS interface (a) and the free water surface (b) show a pronounced peak at $\approx 3680\,\mathrm{cm}^{-1}$. This signal is assigned to stretch vibrations from dangling OH-bonds, with the H atom pointing towards the solid

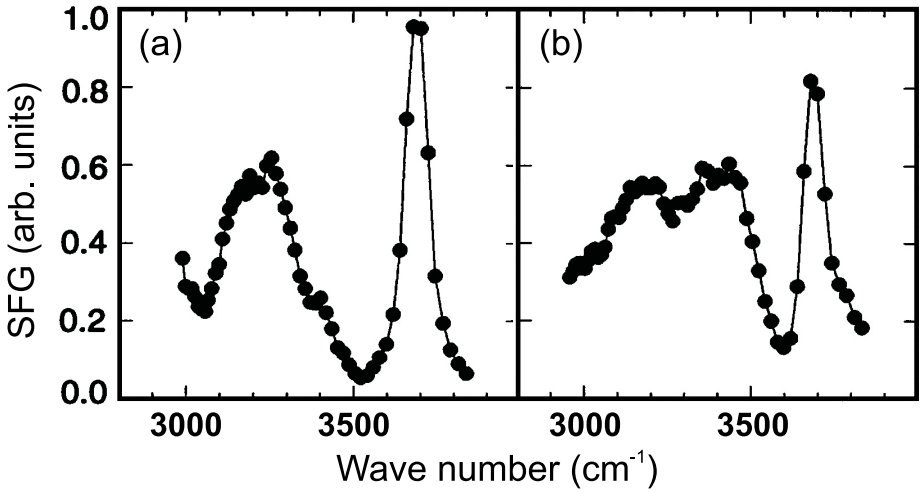

Figure 3.15: Compilation of SFG spectra from water interfaces measured by Du et al. [35]. (a) The quartz-OTS-water interface; (b) the air-water interface.

wall. A semi-quantitative analysis reveals an amount of approximately 25% non hydrogen bonded bonds at the interface. A comparison between the peak positions from the water-solid and the water-vapor interfaces shows only a slight red shift of the water-OTS signal [33]. This confirms that there is no strong interaction but only weak VdW forces in between the solid hydrophobic substrate and the water molecules. Thus, the water-solid and the water-vapor SFG spectra are very similar with respect to the OH dangling bond peak serving as a fingerprint of hydrophobic interfaces. In contrast, remarkable differences occur in the bonded OH-region. For the solid-liquid interface, the absence of SFG intensity in the less ordered water-like region around $3400\,\mathrm{cm}^{-1}$ indicates a more ordered interfacial hydrogen bond network compared to liquid-vapor or liquid-liquid (hexane-water, CCl_4-water) interfaces [34]. Apparently, packing effects at the solid wall force the interfacial water molecules in a more ordered ice-like structure.

Heat conductance across the interface

Thermoreflectance measurements across solid-water interfaces were performed by Ge et al. [31] in 2006. They found a significantly reduced heat conductance at hydrophobic substrates compared to hydrophilic samples. Assuming that the thermal conductance of an interfacial depletion layer is similar to water-vapor, an upper limit of $2.5\,\text{Å}$ for the size of the interfacial gap could be determined.

Experiments on confined water

Apart from experiments on free solid-water systems, various other techniques have been employed in order to study solid-water interfaces. In many of those techniques, the liquid

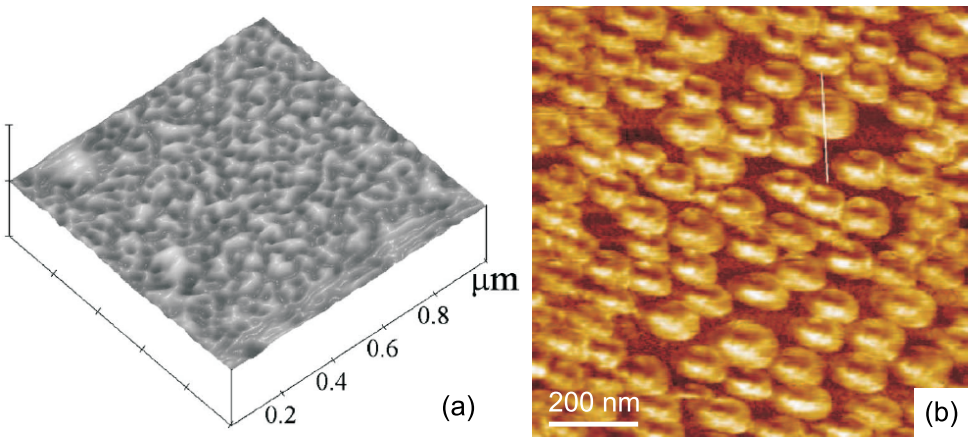

Figure 3.16: Compilation of tapering-mode AFM measurements on hydrophobic solid substrates immersed in water. (a) Hydrophobic glass surface in water taken from Tyrrell et al. [14] (height image, peak-to-valley scale: $30\,\mathrm{nm}$). (b) AFM phase image of the polystyrene-water interface taken from Simonsen et al. [18].

is strongly confined between two objects. Examples are experiments using the surface-force-apparatus (SFA) [6, 95–97], studies on colloidal stability [98], and infrared spectroscopy measurements (ATR-FTIR) on the aggregation of hydrophilic and hydrophobic particles [99]. These experiments probe a completely different situation. Their results can therefore not be compared with studies on single smooth solid-liquid interfaces. Due to capillary evaporation, the dominating length scale in these confined geometries is in the $10\,\mathrm{nm}$ to $100\,\mathrm{nm}$ regime [97] whereas the length scale at a single interface is given by the molecular diameter and the bulk correlation length which are both approximately two orders of magnitude smaller [100].

Atomic force microscopy (AFM)

Nevertheless, especially atomic force microscopy AFM experiments [14–19, 101, 102] are often assumed to probe the intrinsic structure of a free solid-liquid interface. Operating in *non-contact* or *tapering*mode, the tip is separated from the substrate by typically $1\,\text{Å}$ to $20\,\text{Å}$, and thus exactly in the range where the confinement effects observed in SFA measurements are dominant.

Figure 3.16 shows a compilation of AFM measurements performed by Tyrrell et al. and a more recent study from Simonsen et al. [18]. The observed gas nanobubbles exhibit a base area of approximately $0.1\,\mu\mathrm{m}^2$, and a height of several nm [18]. Holmberg et al. showed that they can be manipulated by experimental parameters such as the tapering amplitude [19]. The gas nanobubbles preferentially form on heterogeneous solid-liquid interfaces, i.e. with a patchy surface coverage, exhibiting a roughness in the nm regime [102].

Chapter 4

X-Ray scattering and data analysis methods

4.1 Introduction to x-ray reflectivity

X-ray reflectivity experiments probe the vertical structure of an interface. An inhomogeneous distribution of the refractive index, which is related to the electron density $\rho_{\mathrm{e}}(z)$, leads to scattering of the incident x-ray wave from the density gradient $\frac{\mathrm{d}\rho_{\mathrm{e}}(z)}{\mathrm{d}z}$. The coherent sum of these scattered waves gives rise to the interference pattern measured in reflectivity experiments. Thus, these data carries structural information about the density profile, which can be reconstructed by different analysis methods described in Sec. 4.2.

4.1.1 Scattering geometry

Figure 4.1 shows a sketch of a surface or interface sensitive elastic x-ray scattering experiment on a vertically isotropic sample (gray box). An incident wave with wave vector $\boldsymbol{k}_{\mathrm{i}}$ and a corresponding modulus $k = 2\pi/\lambda$ hits the sample surface under an incident angle α_{i}.

The difference between incident and exit wave vector determines the momentum transfer $\boldsymbol{q} = \boldsymbol{k}_{\mathrm{f}} - \boldsymbol{k}_{\mathrm{i}}$. The total angle 2ϑ between $\boldsymbol{k}_{\mathrm{f}}$ and $\boldsymbol{k}_{\mathrm{i}}$ can be divided into vertical and horizontal components, denoted by δ and χ, respectively. In a coordinate system with the z-axis parallel to the surface normal, and an incident wave traveling in the xz-plane, the components of the momentum transfer $\boldsymbol{q}$ are given by

$$q_x = k\left(\cos\alpha_{\mathrm{f}}\cos\chi - \cos\alpha_{\mathrm{i}}\right) \tag{4.1a}$$

$$q_y = k\cos\alpha_{\mathrm{i}}\sin\chi \tag{4.1b}$$

$$q_z = k\left(\sin\alpha_{\mathrm{f}} + \sin\alpha_{\mathrm{i}}\right)\ . \tag{4.1c}$$

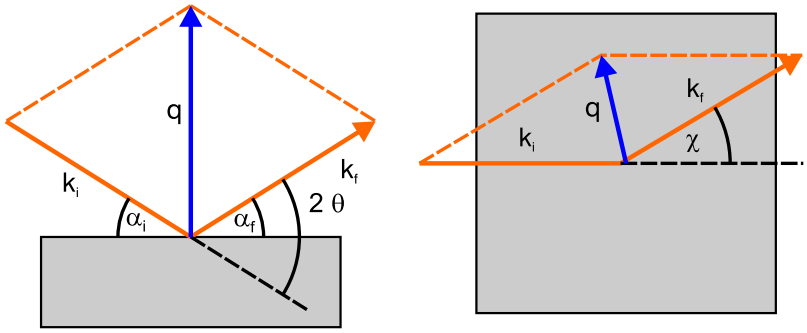

Figure 4.1: Sketch of a surface or interface sensitive x-ray scattering experiment in side (left) and top view (right). The total momentum transfer $\boldsymbol{q}$ to the sample (blue arrow) is given by the difference between the incident and exit wave vectors $\boldsymbol{k}_\mathrm{i}$ and $\boldsymbol{k}_\mathrm{f}$ (orange lines). α_i and α_f are the angles between the surface and the incident and exit beam, respectively. They lead, together with the horizontal component χ (the angle between their projections onto the surface), to the total scattering angle 2ϑ.

4.1.2 Experimental resolution

The x-ray intensity $I\,(\boldsymbol{q})$, measured in an scattering experiment, is an integrated quantity of the differential scattering cross section over the resolution element. The resolution element is spanned by the partial derivatives of the scattering vector $\boldsymbol{q}$, introduced in Eq. (4.1), with respect to the input parameters $\boldsymbol{k}_\mathrm{i}$ and $\boldsymbol{k}_\mathrm{f}$ or, thereto equivalent, with respect to E, α_i, α_f, and χ.

$$\begin{aligned}\delta q_\mathrm{j} \;=\; & \frac{\partial q_\mathrm{j}}{\partial E}\Delta E + \frac{\partial q_\mathrm{j}}{\partial \alpha_\mathrm{i}}\Delta\alpha_\mathrm{i} + \\ & \frac{\partial q_\mathrm{j}}{\partial \alpha_\mathrm{f}}\Delta\alpha_\mathrm{f} + \frac{\partial q_\mathrm{j}}{\partial \chi}\Delta\chi\end{aligned} \tag{4.2}$$

The energy resolution $\frac{\Delta E}{E}$ of the monochromator defines the range for the modulus of the incident wave vector $\Delta k = \frac{\Delta E}{c\hbar}$. The intervals $\Delta\alpha$ of the incidence and exit angle are affected by beam properties, the experimental setup, and the sample. While the divergence of the incidence beam and the sample curvature influence α_i and α_f in the same way, the solid angle, defined by the vertical detector slits, gives an additional contribution to $\Delta\alpha_\mathrm{f}$. In the same way $\Delta\chi$ is defined by the horizontal detector slit[1]. For shallow incidence and exit angles the effect of sample curvature on $\Delta\chi$ is much smaller than on the vertical components $\Delta\alpha_\mathrm{i}$ and $\Delta\alpha_\mathrm{f}$.

[1] In the following, the term taking into account the horizontal divergence of the x-ray beam is omitted. Since the horizontal detector slits are wide open to integrate over the entire reflected beam (see Sec. 5.4.1), β_h has no relevance for the data analysis discussed in chapter 6.

4.1.3 The reflectivity scan

Reflectivity experiments probe the structure perpendicular to an interface or surface, i.e. along the z-direction. Vanishing in-plane components of $\boldsymbol{q}$ can be achieved by keeping the incident and exit angles equal ($\alpha_\mathrm{i} = \alpha_\mathrm{f} = \vartheta$) and $\chi = 0$. This results in a total momentum transfer $\boldsymbol{q} = \boldsymbol{e}_z q_z$ along the z-axis, and Eq. (4.1) simplify to

$$q_x = 0, \quad q_y = 0, \quad q_z = 2k \sin\vartheta \; . \tag{4.3}$$

Experimental resolution

The experimental resolution in a reflectivity experiment is obtained from Eq. (4.2) and the constraints from the reflectivity geometry to

$$\delta q_x = q_z \left(\Delta\alpha_\mathrm{i} + \Delta\alpha_\mathrm{f}\right) \tag{4.4a}$$

$$\delta q_z = \frac{\Delta\lambda}{\lambda} q_z + k \left(\Delta\alpha_\mathrm{i} + \Delta\alpha_\mathrm{f}\right) \; . \tag{4.4b}$$

To extract density profiles from the acquired data, the entire reflected beam has to be measured[2]. Technically, this is achieved by an integration in the (q_x, q_y) plane. Experimentally, it is realized by adjusting the detector slits in such a way, that all the intensity reflected within the range defined by δq_x and δq_y is recorded by the detector. More details on x-ray reflectivity measurements can be found in literature [12, 107].

4.1.4 The rocking scan

A rocking scan is one type of an in-plane scan. In contrast to a reflectivity scan, measuring the integrated reflected intensity, here the angular distribution around the nominal position ($q_x = 0$, i.e. $\alpha_\mathrm{i} = \alpha_\mathrm{f} = \vartheta$) is determined. A rocking scan keeps the vertical component q_z constant[3] by counter-wise changing α_i and α_f.

$$q_x = \left(\alpha_\mathrm{f} - \alpha_\mathrm{i}\right) q_z \tag{4.5a}$$

$$\delta q_x = \left(\Delta\alpha_\mathrm{i} + \Delta\alpha_\mathrm{f}\right) q_z \tag{4.5b}$$

Since rocking scans are highly sensitive to sample movements, they are routinely used for alignment purpose and stability tests. They also allow for checking the sample quality as well as proper mounting with respect to the surface topography of the substrate on a millimeter length scale. Uneven surfaces are amongst others caused by deformations while mounting the sample (see Sec. 5.2.3) or improper polishing which often leads to a convex shape. Especially for small scattering angles 2θ, where the beam footprint spreads over the

[2] When correlations in the interfacial roughness are present, the reflected beam may have a Lorentzian profile. In this case a more elaborated way of measuring reflectivity has to be used [103]. Examples are experiments on rough substrates [104] and from liquid surfaces [105, 106] and interfaces [61].

[3] In first order approximation, the vertical momentum transfer q_z in a rocking scan is constant. Within the relevant scan range $|q_x| \ll q_z$, or equivalently for $\alpha_\mathrm{i} - \alpha_\mathrm{f} \ll \vartheta$, second order terms can be neglected.

entire sample length, wavy surfaces show broad or even splitted peaks, corresponding to the wide distribution of the local surface normal. Furthermore, on horizontally structured interfaces rocking scans carry information on the in-plane correlations [12, 103, 104].

4.2 Calculation of the x-ray reflection pattern

4.2.1 The refractive index

The spatial variation of the electric field of an electromagnetic wave traveling through a homogeneous medium m in z-direction is described by $E = E_0 \mathrm{Re}\left[\exp\left(ik_\mathrm{m} z\right)\right]$. In a linear medium, the modulus of the associated wave vector $\boldsymbol{k}_\mathrm{m}$ is given by $|\boldsymbol{k}_\mathrm{m}| = n\,|\boldsymbol{k}_\mathrm{v}|$ with $\boldsymbol{k}_\mathrm{v}$ denoting the wave vector in vacuum. The complex refractive index n of the medium can be divided into its real part $\mathrm{Re}\,(n) = 1 - \delta$ associated with a modified phase velocity and a complex contribution $\mathrm{Im}\,(n) = \beta$, accounting for absorption [108]:

$$n = 1 - \delta + i\beta \tag{4.6}$$

For x-rays, n can be calculated from the energy-dependent form factors $f^{(1)}(E)$ and $f^{(2)}(E)$ for forward scattering [109][4] via

$$\delta = \frac{\lambda^2}{2\pi} r_\mathrm{e} \rho_\mathrm{e} \frac{f^{(1)}(E)}{Z} \approx \frac{\lambda^2}{2\pi} r_\mathrm{e} \rho_\mathrm{e} \tag{4.7a}$$

$$\beta = \frac{\lambda^2}{2\pi} r_\mathrm{e} \rho_\mathrm{e} \frac{f^{(2)}(E)}{Z} = \frac{\lambda}{4\pi} \mu\,. \tag{4.7b}$$

Far away from absorption edges, the real part δ can be approximated using the electron density ρ_e. The imaginary component β is directly related to the absorption coefficient μ. Tabulated values for $f^{(1)}(E)$ and $f^{(2)}(E)$ as calculated numerically from ab-initio models and are available in the relevant energy range for all elements used in this work [110, 111].

4.2.2 The phase problem in x-ray scattering

Since in x-ray scattering experiments the intensity $I \propto E^2$ of the scattered wave field is recorded, any phase information is missing. Therefore a straight forward Fourier back transformation of the experimentally observed pattern, which would allow an unambiguous reconstruction of the electron density profile $\rho_\mathrm{e}(\boldsymbol{x})$, is impossible. The analysis of a coherent scattering signal thus always requires additional knowledge about the structure, like the atomic composition, the mass density, or the generic type of the interfacial profile. This information can be included in a model, as described in the following sections. An alternative approach is an analysis based on phase retrieval algorithms. More details on this method can be found in literature [12].

[4] The definition of $f^{(1)}$ is inconsistent in literature [109–111]. Here $f^{(1)}$ is defined by the real part of the total x-ray form factor in forward scattering ($q = 0$) as $f^{(1)}(E) = \mathrm{Re}\left[f(E, q=0)\right] = Z + f'(E) + f_\mathrm{NT} + f_\mathrm{rel}$ including the resonances of the electronic system $f'(E)$, as well as the small relativistic (f_rel) and nuclear Thompson (f_NT) corrections.

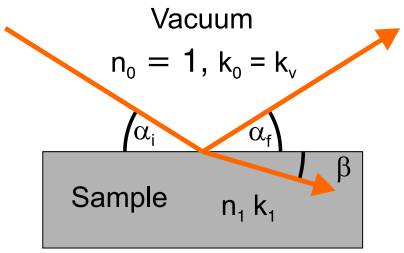

Figure 4.2: Reflection $\alpha_\mathrm{i} = \alpha_\mathrm{f}$ and transmission at a free surface. The incident x-ray beam with a wave vector modulus k_0 impinges from the vacuum side ($n_0 = 1$) on the sample surface ($\mathrm{Re}\,(n_1) < 1$). The transmitted beam with $k_1 = n_1 k_0$ is refracted towards the surface in accordance to Snell's law.

4.2.3 Reflection from one single free interface

Reflection (r) and transmission (t) coefficients of an electromagnetic wave with amplitude E_i at a single sharp interface ($\rho\,(z) = \rho_{-\infty} + (\rho_{+\infty} - \rho_{-\infty})\,\Theta\,(z)$) are calculated from Fresnel formulae[5]:

$$r = \frac{E_\mathrm{r}}{E_\mathrm{i}} = \frac{\sin\,(\alpha - \beta)}{\sin\,(\alpha + \beta)} \tag{4.8a}$$

$$t = \frac{E_\mathrm{t}}{E_\mathrm{i}} = \frac{2\cos\beta\sin\alpha}{\sin\,(\alpha + \beta)} \tag{4.8b}$$

They follow directly from the boundary conditions for the electric field $E\,(\boldsymbol{x})$ and the electric displacement field $D\,(\boldsymbol{x})$ between two semi-infinite materials. Experimentally, the Fresnel reflectivity $R_\mathrm{F}^2 = r^2$ is the measurable quantity.

$$R_\mathrm{F}^2\,(q) = \left|\frac{k_{\mathrm{i},z} - k_{1,z}}{k_{\mathrm{i},z} + k_{1,z}}\right|^2 \tag{4.9a}$$

$$\approx \left(4\pi r_\mathrm{e}\rho_\mathrm{e}\right)^2 \frac{1}{q^4} \quad \text{for } q \gtrsim 3q_\mathrm{c} \tag{4.9b}$$

Here, $k_{\mathrm{i},z} = k_{0,z} = -k\sin\alpha_\mathrm{i}$ and $k_{j,\mathrm{z}} = -k\sqrt{n_j^2 - \cos^2\alpha_\mathrm{i}}$ denote the complex z-components of the incident wave vector and of the transmitted wave vector in medium j with a refractive index n_j[6]. In the visible range of the electromagnetic spectrum the reflectivity depends strongly on the polarization. For x-rays, the probed angles α are very small, thus the polarization dependence is negligible.

Due to multiple scattering effects, the reflected intensity is almost unity for incident angles smaller than the critical angle of total reflection $\alpha_\mathrm{c} \approx \sqrt{2\delta}$[7]. After this plateau, the reflectivity drops rapidly, following asymptotically a q^{-4} decay. In the regime $q \gtrsim 3q_\mathrm{c}$, which is equivalent to $R_\mathrm{F}^2 \lesssim 10^{-3}$, the exact expression Eq. (4.9a) coincides very well with the kinematical approximation Eq. (4.9b), omitting multiple scattering effects (see Sec. 4.2.7).

[5] Equation (4.8) is valid for σ polarization. The corresponding relation for π polarization can be found in [108].

[6] For a single interface the refractive index of the semi-infinite bulk substrate is denoted by n_1, i.e. $j = 1$.

[7] Due to absorption, ($\beta > 0$) the reflected intensity is always less than unity, even for angles smaller than the critical angle of total reflection.

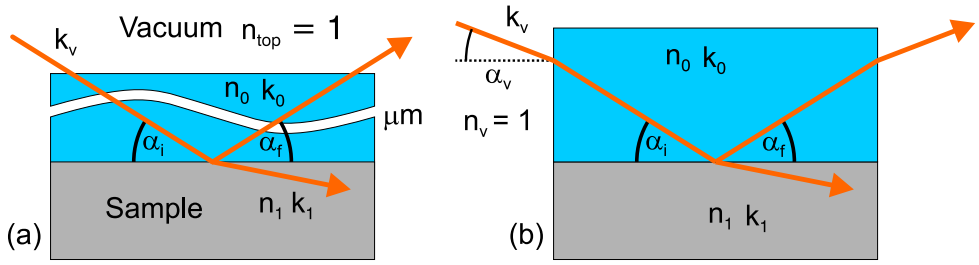

Figure 4.3: (a) Conventional setup of a scattering experiment for a buried interface. The x-ray beam enters the sample through the top surface and travels through a thick layer of material before reaching the interface of interest. (b) Scattering from a deeply buried interface in transmission-reflection geometry. The incident x-ray beam hits the top material with a refractive index $n_0 \neq 1$ at almost normal incidence from the side.

4.2.4 Reflection from buried interfaces

Equations (4.9) describe the reflection pattern $R^2\left(q_\mathrm{z}\right)$ from a sample with refractive index $n_\mathrm{top} = 1$ for the top layer (vacuum or in good approximation also air, see Fig. 4.3a). In contrast, the analysis of reflectivity data from buried interfaces, recorded in transmission-reflection geometry, requires some slight modifications in the z-components of the wave vectors $k_{\mathrm{j,z}}$. Figure 4.3b shows a sketch of the scattering geometry corresponding to the experimental setup used in this work. The incident beam $\boldsymbol{k}_\mathrm{v}$ (vacuum, $n_\mathrm{v} = 1$) penetrates the top material with the complex refractive index n_0 (in this case water) from the side at almost normal incidence ($90° - \alpha_\mathrm{v}$), i.e. $\sin\left(\alpha_\mathrm{v}\right) \ll 1$). Since the incident beam hits the side interface almost perpendicular, the refraction $\alpha_\mathrm{i} - \alpha_\mathrm{v} \approx \delta_\mathrm{top}\alpha_\mathrm{i}$ at this interface is negligible compared to the beam divergence[8]. In according to Snell's law, the component $k_{j,\mathrm{z}}$ of the wave vector parallel to the interface normal, travelling in medium j with an refractive index n_j, is given by

$$k_{j,\mathrm{z}} = -\frac{E}{c\hbar}\sqrt{n_j^2 - n_0^2\cos^2\alpha_\mathrm{i}} \tag{4.10a}$$

$$\approx -\frac{E}{c\hbar}n_0\sqrt{\left(1 + n_j - n_0\right)^2 - \cos^2\alpha_\mathrm{i}}\,. \tag{4.10b}$$

Here, n_0 denotes the index of refraction in the top material. The Fresnel reflectivity $R_\mathrm{F}^2\left(q\right)$ from a buried interface can now be calculated from Eq. (4.9a) by simply exchanging the z-components of the wavevectors $k_{0,z}$ and $k_{1,z}$ with their corresponding expressions for transmission-reflection geometry taken from Eq. (4.10a). Likewise, for more complex structures described in the following section, all reflectivity formulae from standard textbooks [12], formulated for the conventional geometry shown in Fig. 4.3a, can be adopted

[8] For water as top material ($\delta_{\mathrm{H_2O}} = 4.37 \cdot 10^{-8}$) and an incident angle of $\alpha_\mathrm{v} = 1°$ the refraction is $\alpha_\mathrm{i} - \alpha_\mathrm{v} = 3 \cdot 10^{-4}\,\mu$rad. Compared to the vertical beam divergence of $\beta_\mathrm{v} = 25\,\mu$rad (see Sec. 5.1.1) this contribution is negligible. Inhomogeneities in the top layer and the x-ray windows have much larger effects.

to the transmission-reflection scheme by use of Eq. (4.10). Equation (4.10a) can be approximated to second order in δ and β by Eq. (4.10b). This shows, that in the case of a buried interface, the reflection pattern is similar to the one obtained from a refractive index profile[9] n'_j with the top layer subtracted from all of the underlying material ($n'_j = 1 + n_j - n_0$). For a single interface in the kinematical approximation this leads to a reflectivity of

$$R_{\mathrm{F}}^2(q) \approx \left[4\pi r_{\mathrm{e}} \left(\rho_{+\infty} - \rho_{-\infty}\right)\right]^2 \frac{1}{q^4} \,. \tag{4.11}$$

4.2.5 Multiple interfaces and the slab model

More complex systems than the ones shown in Fig. 4.3 may exhibit a rich vertical structure at the interface. Such a profile can often be divided in a series of slabs with well defined interfaces. For each single interface $(j, j+1)$ the amplitudes of the reflected and transmitted wave can be calculated using Fresnels formulae (see Eq. (4.8) and Fig. 4.4). A consistent solution of the associated slab profile combines these independent reflection coefficients $r_{j,j+1}$ by including the respective retardations between the different layers.

Recursive Parratt formalism

A layered structure of N slabs, including the top layer ($j = 0$) and the bulk substrate ($j = N-1$), each with a refractive index n_j, is shown in Fig. 4.4[10]. One possible implementation for solving the reflection problem from multiple interfaces consistently, is the recursive Parratt formalism [10, 12, 112]. The reflectivity $R^2 = |X_0|^2$ is calculated from the squared modulus of the transition coefficient[11] X_0, which can be derived, starting from the vanishing coefficient at the semi-infinite bulk substrate ($X_{N-1} = 0$), recursively via

$$X_j = \varphi_{j,j} \frac{(r_{j,j+1} + X_{j+1}\varphi_{j+1,j})}{(1 + r_{j,j+1} X_{j+1}\varphi_{j+1,j})} \tag{4.12a}$$

$$r_{j,j+1} = \frac{(k_{j,\mathrm{z}} - k_{j+1,\mathrm{z}})}{(k_{j,\mathrm{z}} + k_{j+1,\mathrm{z}})} \tag{4.12b}$$

$$\varphi_{l,m} = \exp\left(-2ie^{i(l+m)\pi} k_{l,\mathrm{z}} z_m\right) . \tag{4.12c}$$

Interfacial roughness and Parratt formalism

In a real system, the electron density profile $\rho_{\mathrm{e}}(z)$, and therefore also the refractive index profile $n(z)$ at an interface never follows a Heaviside step function $\Theta(z - z_0)$ as assumed

[9] Far away from absorption edges, the refractive index is directly related to the electron density profile via Eq. (4.7).

[10] The indexation of the slabs is arbitrary and inconsistently used in literature. Here, the notation of the program for data analysis, which was developed within this thesis, is used. The C++ syntax suggests arrays of N elements labeled from 0 to $N-1$.

[11] The transition coefficient $X_j = \frac{R_j}{T_j}$ is the ratio between the reflected and transmitted wave amplitudes at the interface j, in accordance to Fig. 4.4.

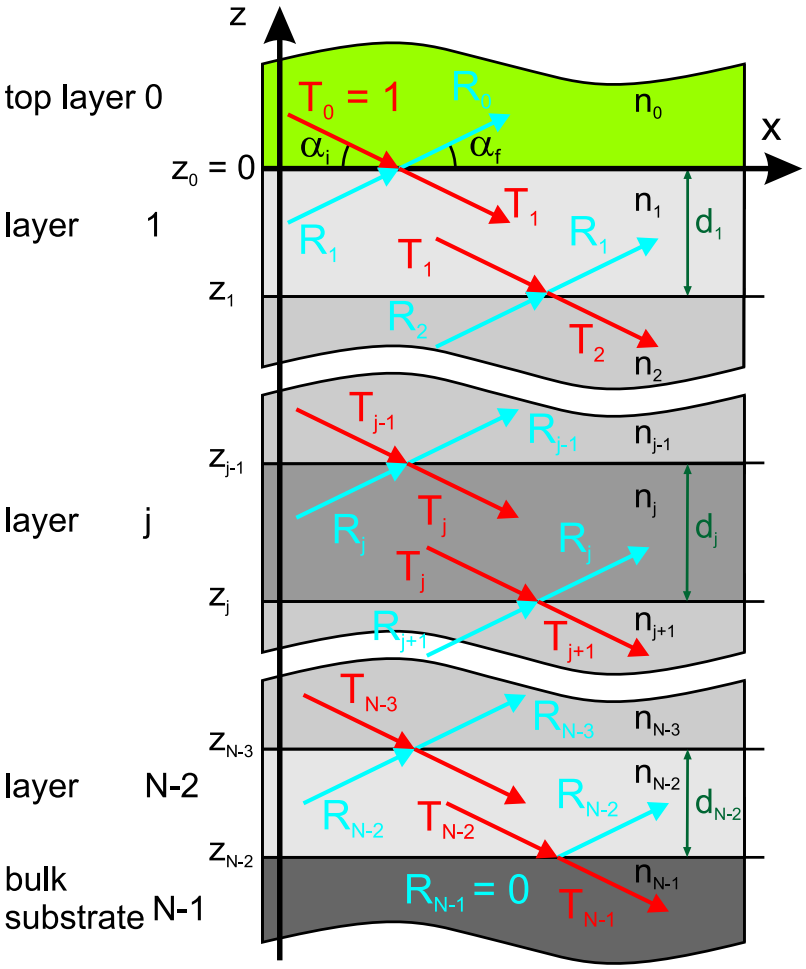

Figure 4.4: Model profile with N slabs, including the top layer ($j = 0$) and the semi-infinite bulk substrate ($j = N - 1$).

in Sec. 4.2.3. At least atomic corrugation in the 1 Å regime is present.

For a single interface, following an error function or hyperbolic tangent profile, the reflected and transmitted wave amplitudes can be calculated analytically by solving Maxwell's equations [108, 113]. For an error function profile $n(z) \propto \frac{1}{2}[1 + \mathrm{erf}(z)]$ a reflection coefficient $r'_{0,1} = r_{0,1}e^{-k_z^2}$ is obtained. The reflection coefficient at a rough interface is modified from $r_{0,1}$ introduced in Eq. (4.12b) by an exponential damping term. A more detailed analysis in second order DWBA[12] theory performed by de Boer [114] shows that not only the averaged vertical profile, but also the in-plane correlations of the roughness determine the exact form of the damping factor. For uncorrelated roughness, the Nevot-Croce (NC) result is valid, whereas for an interface with correlated roughness the Beckmann-Spizzichino (BS) form has to be applied:

$$r'_{j,j+1} = r_{j,j+1}e^{-2k_{j,z}k_{j+1,z}\sigma_j^2} \quad \text{NC} \tag{4.13a}$$

$$r'_{j,j+1} = r_{j,j+1}e^{-2k_{j,z}^2\sigma_j^2} \quad \text{BS} \tag{4.13b}$$

[12] Distorted Wave Born Approximation

The roughness parameter σ_j^2 denotes the width of the Gaussian associated to the error function.

A refractive index profile, modeled by a series of slabs including interfacial roughness, is described by

$$n(z) = \sum_{j=0}^{N-1} n_j(z) \tag{4.14a}$$

$$n_j(z) = n_j \left[\operatorname{erf}\left(\frac{z - z_{j-1}}{\sqrt{2}\sigma_{j-1}} \right) - \operatorname{erf}\left(\frac{z - z_j}{\sqrt{2}\sigma_j} \right) \right] . \tag{4.14b}$$

In the case of well separated interfaces with

$$\sigma_j \ll d_j \quad \text{and} \quad \sigma_j \ll d_{j-1} \quad \text{for all slabs } j, \tag{4.15}$$

the modified reflection coefficients $r'_{j,j+1}$ can be used to calculate the reflection pattern from the slab model Eq. (4.14) within the Parratt formalism Eq. (4.12).

The reflection coefficients $r'_{j,j+1}$ were derived for a single independent interface between two semi-infinite slabs (i.e. $n(z)$ asymptotically approaches a constant value in the limit $z \to \pm\infty$). As soon as the condition Eq. (4.15) is violated, i.e. the slab thickness approaches the roughness of at least one of the associated interfaces, $n(z)$ does not show distinct slabs anymore, but a smeared out structure, where different layers interfuse with each other. In this case the analytically obtained damping factors Eq. (4.13) are not applicable any more [12] and other analysis methods have to be used.

Nevertheless, in some cases the reflectivity calculated with the exponential damping factors Eq. (4.13) still gives a good approximation to the real pattern, even in cases where Eq. (4.15) is strongly violated. The reason is that the intensity from a rough interface decays rapidly, while the contribution from of a thin layer is relevant mainly for large momentum transfers q_z. In order to detect a layer of $d = 5\,\text{Å}$ thickness unambiguously, the reflection pattern has in general to be analyzed at least up to a vertical momentum transfer of $q_z = \pi/d \approx 0.6\,\text{Å}^{-1}$. On the other hand, a roughness of $\sigma = 3\,\text{Å}$ results in a damping of the reflected intensity of more than 6 orders of magnitude below the Fresnel curve in the relevant q range. This example shows that the scattering signal from such a profile often decays so rapidly that the background level is reached before sensitivity to the detailed structure is achieved, and limitations of the model become relevant.

4.2.6 Arbitrary profiles – Slicing

Profiles which cannot be described by Eq. (4.14) or do not fulfill the requirements Eq. (4.15) can be treated by slicing [12]. Here, an arbitrary profile is sliced into equidistant slabs with a thickness much smaller than the vertical structure. Taking into account that the natural length scale of an atomic profile is given by at least the Bohr radius, slices of $0.2\,\text{Å}$ are in general sufficient to treat most reflectivity problems.

Using the recursive Parratt formalism Eq. (4.12), the reflection pattern from profiles extending over $4\,\mathrm{nm}$ (which requires the consideration of 200 independent interfaces) can be calculated on a modern PC within some $100\,\mu\mathrm{s}$.

4.2.7 Kinematical approximation and master formalism

Master formula

In the framework of the kinematical approximation, the x-ray reflectivity $R^2(q_z)$ from a given continuous electron density profile $\rho_\mathrm{e}(z)$ can be calculated by the so-called master formula [11, 12]

$$R^2(q) = R_\mathrm{F}^2(q)\,|F(q)|^2 \tag{4.16a}$$

$$F(q) = \frac{1}{\rho_{-\infty}-\rho_{+\infty}}\int_{-\infty}^{+\infty}\mathrm{d}z\,\frac{\mathrm{d}\rho(z)}{\mathrm{d}z}e^{iqz}\,. \tag{4.16b}$$

In the region of the critical angle where multiple scattering effects are dominant the kinematical approximation is not applicable. On the other hand, Eq. (4.16) is an excellent approximation in the regime well above the critical angle of total reflection, where the reflectivity drops below 10^{-3}, i.e. $q_z > 3q_\mathrm{c} = 6\lambda^{-1}\sqrt{\pi r_\mathrm{e}(\rho_{-\infty}-\rho_{+\infty})}$. $R^2(q)$ can be separated into the smooth and rapidly decaying Fresnel reflectivity $R_\mathrm{F}^2(q)$ (see Eq. 4.9), representing the reflection from a sharp step of the height $h = (\rho_{+\infty}-\rho_{-\infty})$, and the structure factor $F(q)$, describing the interference pattern caused by the specific electron distribution $\rho_\mathrm{e}(z)$.

Refraction corrections

The presence of the total reflection plateau extending up to the critical angle shifts all the features in the reflection pattern to slightly higher angles than predicted by the master formalism. This can be taken into account by the refraction corrections, modifying the wave vectors q_z from Eq. (4.3) to

$$q_z' = 2k_0\sin\sqrt{\vartheta^2-\alpha_\mathrm{c}^2}\,. \tag{4.17}$$

In general, the exact reflectivity falls somewhere in between the values calculated within master formalism and the ones obtained by including the refraction corrections.

The slab model within the master formalism

Equation (4.16) provides an alternative approach to handle density profiles $\rho_\mathrm{e}(r)$ constructed with Eq. (4.14). Especially for profiles where the thickness d_j of each slab is not significantly larger than the respective roughness σ_j and σ_{j-1}, an independent formalism is strongly desired. Inserting the profile Eq. (4.14) into Eq. (4.16), the structure factor

$F(q_z)$ can be calculated analytically:

$$F(q_z) = \frac{1}{\rho_{\mathrm{e},N-1} - \rho_{\mathrm{e},0}} \sum_{j=0}^{N-2} (\rho_{\mathrm{e},j+1} - \rho_{\mathrm{e},j})\, e^{\frac{1}{2}\sigma_j^2 q_z^2} e^{iq_z z_j} \tag{4.18}$$

In analogy, the reflectivity for many other relevant structures such as layering at interfaces and surfaces, can be calculated directly with Eq. (4.16) within the kinematical approximation [106, 115, 116].

4.3 From scattering data to real space information

4.3.1 Reconstruction of $\rho_{\mathrm{e}}(r)$ by parameter refinement

Setting up an adequate model

Due to the loss of phase information a unique inversion of the reflectivity is not possible without additional information about the studied system (see Sec. 4.2.2). The different models described in the previous sections offer a way to include this knowledge in the analyses. The free model parameters are then determined by fitting the model reflectivity to the experimental data points. As a rule of thumb, the number of independent free fitting parameters to be determined by parameter refinement is limited to the number of independent features visible in the data set. In a reflectivity measurement, such features can be, amongst others, the oscillation period, the oscillatory strength and its modulation and decay, asymmetry and deviation from an equidistant pattern, the widths and smearing out of the minima, and the overall decay of the reflectivity with respect to the Fresnel curve. More fitting parameters may give a better reproduction of the experimental data but at the expense of a physically meaningful parameter set.

From Eq. (4.16) and Eq. (4.11) it can be directly deduced that at least one of the values $n(z = \pm\infty)$ has to be known independently. If the atomic composition of a layer is known, δ and β of the refractive index are coupled via the respective atomic form factors leading to a drastic decrease in the number of free parameters. If the total quantity of material, i.e. the product of thickness times density within one slab, is known, another parameter drops out. The vertically projected electron surface density of two or more neighboring slabs can be linked to each other. This is often the case for large organic molecules. They can be modeled as different sub-layers (e.g. head and tail group) of anchored molecules which are deposited in an ordered monolayer on top of a substrate. The ratio between the number of electrons within each sub-layer is fixed by their molecular composition.

For simple profiles, as found in smooth films or multi-layers with significant contrast, there are several open source programs published [117] which can be readily used and are available for different platforms. They are ideal tools for the analysis of the problems they were developed for. But they cannot provide the flexibility needed for a convenient implementation of the required constraints mentioned above. In general, the in-depth analysis of

cutting edge experiments in x-ray reflectivity depends strongly on a custom-made program which incorporates all the specific knowledge about the system [104, 118, 119].

The deviation χ

In order to refine a set of parameters to fit a given model, a scalar quantity χ, also called *cost function*, has to be defined. χ describes the deviation between the given experimental data set and the model as a function of the free parameters. Subsequently, the minimum of χ has to be found by a suitable numeric algorithm as described in the following paragraph.

As the reflection pattern from a state of the art experiment at a 3$^{\mathrm{rd}}$ generation synchrotron source typically covers a dynamic range of more than nine orders of magnitude, an adequate scaling is essential. This allows to take into account the low intensity parts in the high-q regime. This is of particular importance as these data points are most sensitive to real space features on small length scales.

Dividing the measured reflectivity R^2 by the Fresnel reflectivity R_{F}^2, i.e. the pattern corresponding to a sharp interface, leads to a significant reduction in the dynamic range[13]. Within this approach, the cost function χ_{F} between the experimental data points $I_{i,\mathrm{exp}}$[14] and the calculated pattern $I_{i,\mathrm{cal}} = R^2(q_i)$ is given by

$$\chi_{\mathrm{F}} = \min_{\alpha} M^{-1} \sum_{i=1}^{M} \frac{\left(\alpha I_{i,\mathrm{exp}} - I_{i,\mathrm{cal}}\right)^2}{R_{\mathrm{F}}^2(q_i)} \,. \tag{4.19}$$

Here, α denotes a constant scaling factor which can be determined from the primary beam intensity or the reflected intensity below the critical angle of total reflection. On the other hand, the considerable beam hardening due to the high attenuation factor of the absorber in the low angle part renders absolute measurements quite inaccurate (see Sec. 5.1.5). Therefore it is preferable to adjust α in such a way that the deviation χ reaches a minimum. Further improvements can be achieved by adding an additional damping term $\exp(-q^2\sigma^2)$ taking into account the overall roughness σ of the interface[15].

However, well-defined layered structures with a small interfacial roughness, such as the hydrophobic surface coating used in this work, give rise to oscillatory patterns spanning up to three orders of magnitude in R^2/R_{F}^2. To overcome this problem, an alternative way of defining a cost function is the logarithmic deviation

$$\chi_i = \ln \alpha I_{i,\mathrm{exp}} - \ln I_{i,\mathrm{cal}} \tag{4.20a}$$

$$= \ln \alpha + \delta_i \tag{4.20b}$$

in each data point i, with $\delta_i = \ln I_{i,\mathrm{exp}} - \ln I_{i,\mathrm{cal}}$. Logarithmic scaling provides an equal weighting of the various features in the reflection pattern with respect to their relative

[13] In a simplified approach, the reflectivity is scaled with q^{-4}, i.e. the high-q approximation for $R_{\mathrm{F}}^2(q)$.

[14] The measured count rates have to be corrected for the beam footprint (Sec. 5.4.2), the detector dead time constant (Sec. 5.1.4), and the attenuation of the absorber (Sec. 5.1.5) in order to obtain $I_{i,\mathrm{exp}}$.

[15] As there is no unique method for the *a priori* determination of the overall roughness σ, this damping term introduces a large degree of ambiguity in the data analysis.

intensity. Based on Eq. (4.20), the overall deviation between the calculated and the experimentally obtained reflection pattern is given by

$$\begin{aligned} \chi^2 &= \min_{\alpha} M^{-1} \sum_{i=1}^{M} \chi_i^2 && \text{(4.21a)} \\ &= \min_{\alpha} \left[(\ln \alpha)^2 + 2 \ln \alpha \langle \delta \rangle + \langle \delta^2 \rangle \right] && \text{(4.21b)} \\ &= \langle \delta^2 \rangle - \langle \delta \rangle^2 \, . && \text{(4.21c)} \end{aligned}$$

The constant $\ln \alpha = -\langle \delta \rangle$ in Eq. (4.21b) is determined by the condition that χ approaches a minimum for the correct normalization/scaling factor α. This has the advantage that α is not a free fitting parameter but can be determined directly in each refinement step. In order to avoid numerical errors, the experimental data are pre-normalized iteratively with the α of the preceding fitting step. This ensures that in the final phase of the refinement procedure $\langle \delta \rangle^2$ is small compared to $\langle \delta^2 \rangle$.

Fit algorithms

The minimum of the cost function χ has to be determined numerically in a multi-dimensional parameter space. In general, χ exhibits several local minima. Deterministic algorithms, such as the simplex method, find a minimum close to the given starting values very efficiently, but they likely fail reaching the global minimum in a complex multi-parameter problem. The idea behind stochastic Monte Carlo fitting algorithms is that they are quasi ergodic, i.e. they explore the entire parameter space in order to find the global minimum[16]. In this work the Adaptive Simulated Annealing algorithm developed by Ingber [13, 120] was used.

4.3.2 Semi-quantitative analysis – The gap-step model

In this section, a model reduced to the most fundamental features of the water-OTS system is discussed. For this specific model profile, the x-ray reflectivity can be calculated analytically in the kinematic approximation. This solution offers a direct interpretation of selected features in the manifold interference pattern observed in a x-ray reflectivity experiment. It provides not only a straightforward way for semi-quantitative data analysis, but also gives a deeper insight into the sensitivity of the measurement to certain features in the real space density profile $\rho_{\mathrm{e}}(z)$. It is therefore not a substitutional but important complementary tool to the parameter refinement discussed in section 4.3.1.

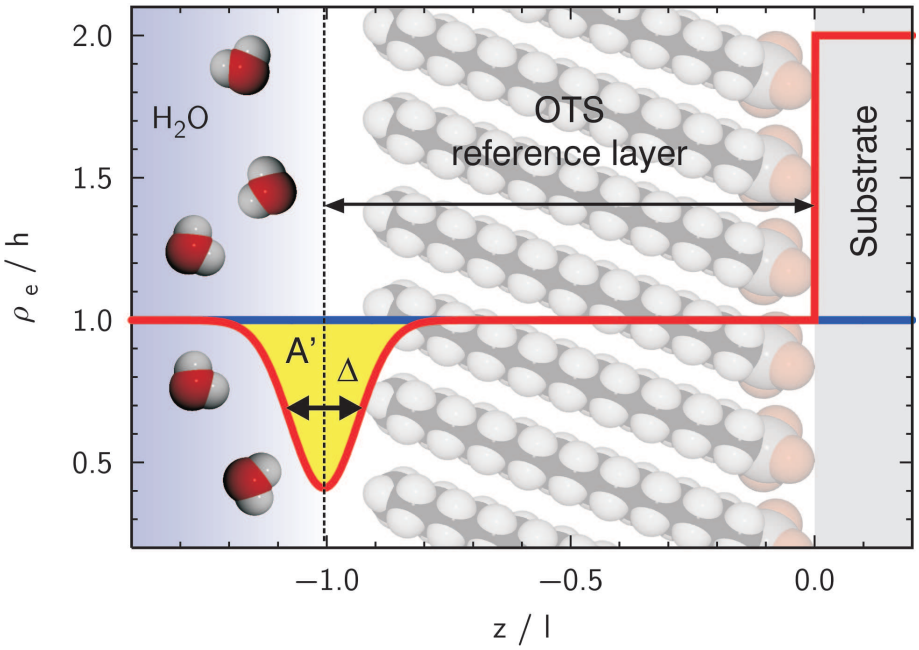

Figure 4.5: Normalized electron density profile ρ_e/h against z/l for the gap-step model calculated from Eq. (4.22). The dimensionless model parameters are $A' = 1$ for the integrated density deficit and $\Delta' = 9$ determining the width of the gap.

The gap-step profile

A basic model of the water-OTS system must include at least a thin layer of decreased or increased water density (depletion gap or compression peak) on top of a contrast matched reference layer ($\rho_{\mathrm{rl}} = \rho_{-\infty} = \rho_0$) deposited on a semi-infinite substrate ($\rho_{\mathrm{s}} = \rho_0 + h$). One possible realization of the associated electron density profile is given by

$$\rho_{\mathrm{e}}(z) = \rho_0 + \underbrace{\frac{A}{\sqrt{2\pi}\Delta_{\mathrm{g}}} e^{-\frac{(z+l)^2}{2\Delta_{\mathrm{g}}^2}}}_{\text{gap}} + \underbrace{\frac{h}{2}(1+\Theta(z))}_{\text{step}}, \tag{4.22}$$

which is illustrated in Fig. 4.5. The gap (yellow area) in between the contrast matched reference layer and the top material (in this case the H_2O bulk) with density ρ_0, can be

[16] An ergodic track through parameter space approaches any parameter set arbitrarily close in a finite time. In the implementation on a computer, the refinement process has to be stopped at a certain point. Thus, also for stochastic fitting algorithms there is a non-zero probability to get stuck in a local minimum.

modeled as a Gaussian with an integral density deficit A and a FWHM of $2\sqrt{2\ln 2}\Delta_\mathrm{g}$. It is spaced from the substrate by the thickness l of the reference layer. The interface to the substrate, with an electron density of $\rho_\mathrm{s} = \rho_0 + h$, is represented by a step function.

Reflectivity from the gap-step model in the kinematic approximation

Combining the density profile $\rho_\mathrm{e}(z)$ of the gap step model introduced in Eq. (4.22) with the master formalism Eq. (4.16) leads to an analytic expression for the structure factor $F(q_z)$ in the kinematic approximation.

$$F(q) = 1 - \frac{A}{h} q e^{-\frac{1}{2}\Delta_\mathrm{g}^2 q^2} e^{i\left(ql - \frac{\pi}{2}\right)} . \tag{4.23}$$

Due to the derivative in Eq. (4.16) the structure factor $F(q)$ does not depend on the bulk density ρ_0 of the material on top of the reference layer but only on the difference h with respect to the semi-infinite substrate. By introducing the dimensionless variables $q' = \frac{ql}{2\pi}$, $\Delta' = \frac{2l}{\pi\Delta_\mathrm{g}}$, and $A' = e^{-\frac{1}{2}}\frac{|A|}{h\Delta_\mathrm{g}}$ Eq. (4.23) transforms into

$$F(q') = \underbrace{1}_{\text{step}} + \underbrace{\frac{4\sqrt{e}A'}{\Delta'} q' e^{-\frac{1}{2}\left(4\frac{q'}{\Delta'}\right)^2}}_{\text{gap amplitude}} \underbrace{e^{2\pi i\left(q' \pm \frac{1}{4}\right)}}_{\text{gap phase}} . \tag{4.24}$$

As the Fourier transformation is linear, the different terms in Eq. (4.24) can directly be assigned to the corresponding features in real space (see Eq. (4.22)). The sharp step of the electron density at the OTS-SiO_2 interface leads to a constant in the structure factor (solid black line in Fig. 4.6 and horizontal arrow in Fig. 4.7). This constant part interferes with the contribution from the interfacial density depletion with a q'-dependent gap amplitude (purple envelope in Fig. 4.6) and a oscillating phase factor, governed by the distance l between the substrate and the gap. The density model Eq. (4.22) can be extended by adding a roughness σ to the substrate interface, i.e. replacing the step function $\theta(z)$ with an error-function $\mathrm{erf}\left(\frac{z}{\sqrt{2}\sigma}\right)$. This modification in the real space electron density profile $\rho_\mathrm{e}(z)$ adds an exponential decay factor $e^{-\sigma^2 q^2}$ to the constant step amplitude $F_\mathrm{step} = 1$ in Eq. (4.23). A positive shift in the phase factor denotes a density depletion as shown in the real space profile of Fig. 4.5. A density increase at the water-OTS interface would in turn lead to a negative shift in the phase factor. Thus, a shift of the oscillations in the structure factor with respect to integer values of q' allows to determine unambiguously a density depletion or increase at the water-OTS interface.

Figure 4.8 shows two structure factors calculated from Eq. (4.24). A ratio of step height h and gap amplitude A corresponding to $A' = 1$ produces pronounced oscillations in the structure factor. For a gap width of $\Delta' = 7$ the maximum oscillation amplitude appears around $q' = 7/4$. A more narrow gap in the electron density profile ($\Delta' = 9$) produces its strongest modulations in the structure factor at $\Delta' = 9/4$. In the case of a density depletion ($A < 0$, Fig. 4.8 solid line) at the interface, the structure factor is shifted by $-1/4$, for a density increase ($A > 0$, Fig. 4.8 dashed line) by $+1/4$, respectively.

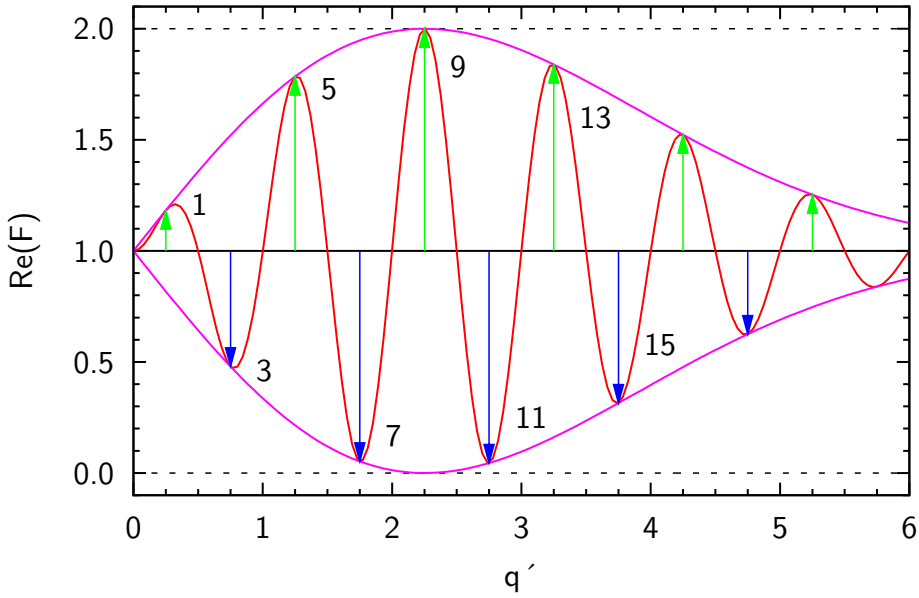

Figure 4.6: Interference pattern of the different terms of Eq. (4.24) for the dimensionless parameters $A' = 1$ and $\Delta' = 9$. The envelope function is denoted by the solid purple line, and the real part $\mathrm{Re}\,(F)$ of the structure factor is shown as the oscillating solid red line. Arrows indicate the positions where the phase factor leads to constructive (arrows pointing upwards) or destructive (arrows pointing downwards) interference with the constant originating from the step. The maximum value is determined by A' at the position $q' = \Delta'/4$.

4.3.3 Gauss dip versus slab model

In this section, the sensitivity of the x-ray reflectivity measurements to the shape of the depletion gap is discussed. As alternatives a Gaussian depletion profile $G\,(z)$ and a gap profile given by

$$E\,(z) = \frac{\sigma}{2d}\left[\mathrm{erf}\left(\frac{d+2z}{\sqrt{8}\sigma}\right) + \mathrm{erf}\left(\frac{d-2z}{\sqrt{8}\sigma}\right)\right], \tag{4.25}$$

which mimicks a Gaussian by a series of consecutive slabs in the limit $d \to 0$, is used. The profile $E\,(z)$ is described by two error function profiles with a width σ, spaced from each other by d. From the two constraints that the area A and the peak value $E\,(z=0)$ have to coincide for both models, one gains a relation between the width Δ_{g} in the Gaussian model

$$G\,(z) = \frac{1}{\sqrt{2\pi}\Delta_{\mathrm{g}}\,(d,\sigma)} e^{-\frac{z^2}{2\Delta_{\mathrm{g}}(d,\sigma)^2}} \tag{4.26}$$

and the parameters d and σ in the model profile described by Eq. (4.25). For clarity, the area A and the value for $z \to \pm\infty$ have been set to 1 and 0, respectively. $\Delta_{\mathrm{g}}\,(d,\sigma)$ can be

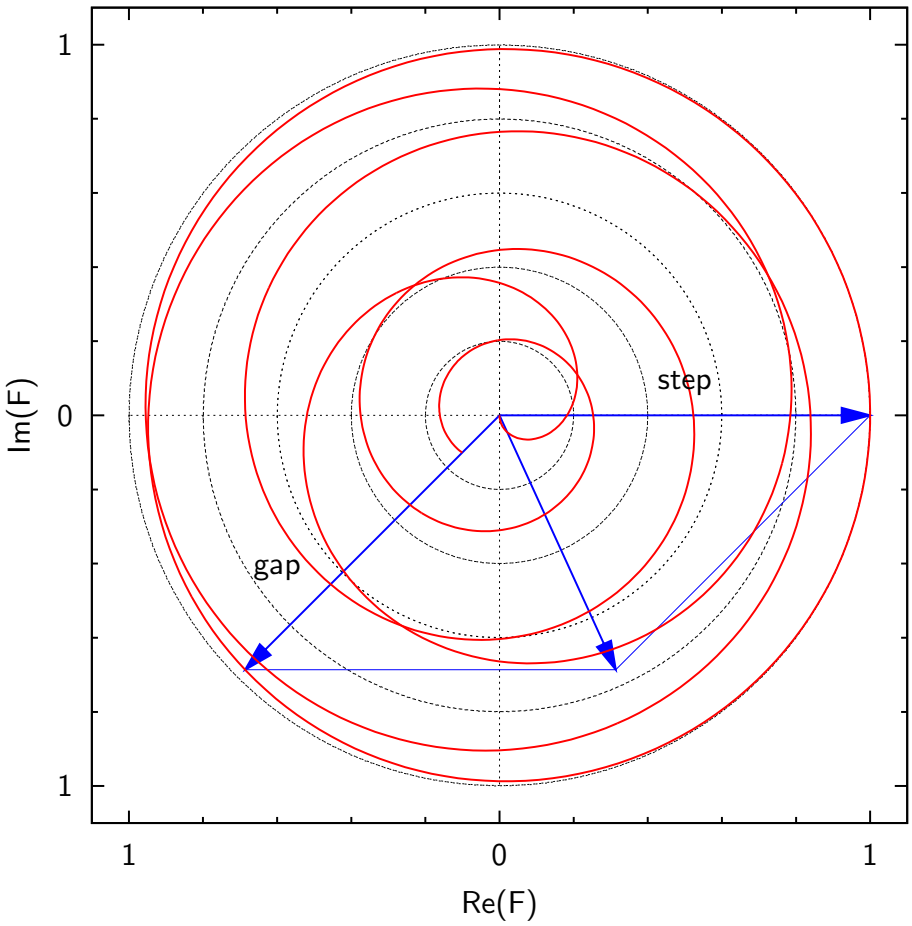

Figure 4.7: 2-D visualization in the complex plane of the superposition of the gap ($F^{\mathrm{gap}} = 1$) and step ($F^{\mathrm{step}}(q')$) terms in Eq. (4.23) for the parameter set ($A > 0$, $A' = 1$, $\Delta' = 9$). The blue arrows depict the interference for $q' = \frac{7.5}{4}$.

expanded in a Taylor series:

$$\Delta_{\mathrm{g}}(d,\sigma) = \frac{d}{\sqrt{2\pi}\sigma \mathrm{erf}\left(\frac{d}{\sqrt{8}\sigma}\right)} \tag{4.27a}$$

$$= \sigma\left[1 + \frac{1}{24}\left(\frac{d}{\sigma}\right)^2 + \frac{1}{5760}\left(\frac{d}{\sigma}\right)^4 \ldots\right] \tag{4.27b}$$

Figure 4.9a shows a selection of profiles calculated from Eq. (4.25) together with the associated Gaussian profiles $G(z)$. The corresponding Gaussian width $\Delta_{\mathrm{g}}(d,\sigma)$ is shown in Fig. 4.9b (solid line) together with the approximation in a third order Taylor expansion (dashed line). For a slab d, which is thin compared to the interfacial roughness σ (i.e.

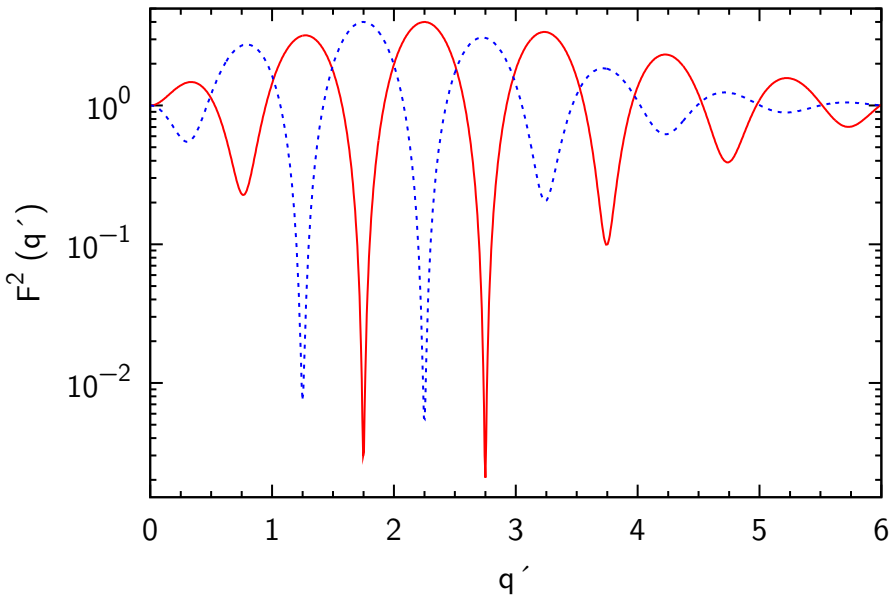

Figure 4.8: Normalized reflection pattern $F^2 = R^2/R_\mathrm{F}^2$ from the gap-step model for the parameter sets $A < 0$, $A' = 1$, $\Delta' = 9$ (solid line) and $A > 0$, $A' = 1$, $\Delta' = 7$ (dashed line).

$\frac{d}{\sigma} \lesssim 1$), both profiles coincide almost perfectly. For larger values (e.g. $\frac{d}{\sigma} = 4$) significant deviations in the profile shape occur (see Fig. 4.9c). A quantitative measure for the match between the two models is given by the integrated quadratic deviation χ^2_GE:

$$\chi_\mathrm{GE}\left(d,\sigma\right)^2 = \int_{-\infty}^{+\infty} \left[E\left(z\right) - G\left(z\right)\right]^2 \mathrm{d}z \tag{4.28a}$$

$$\approx \chi_0^2 \left(\frac{d}{\sigma}\right)^8 \tag{4.28b}$$

$$\text{for} \quad \frac{d}{\sigma} \lesssim 1, \quad \chi_0 \approx 6.12 \cdot 10^{-8}$$

Note that the parameters d and σ are represented by one single parameter $\Delta_\mathrm{g}\left(d,\sigma\right)$ in the Gaussian model. In return, for a slab model as discussed here it is not possible to determine the two parameters d and σ independently from each other in the case of $\frac{d}{\sigma} \lesssim 1$ as there is an infinite set of parameters resulting in almost the same electron density profile $\rho_\mathrm{e}\left(z\right)$. This confirms that it is not possible to determine details of the density profile beyond a lower boundary of approximately 2σ.

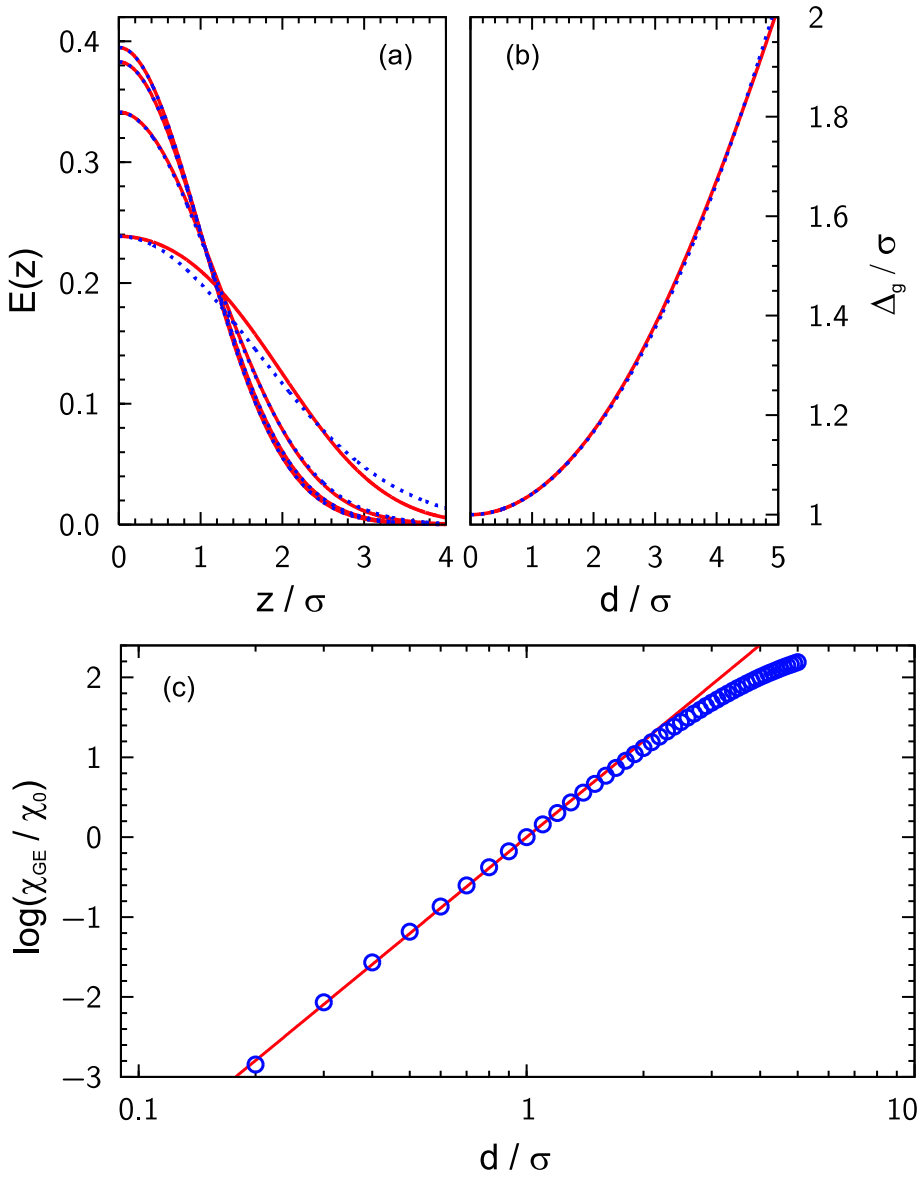

Figure 4.9: (a) Model profiles calculated from Eq. (4.25) (solid red lines) and the associated Gaussians with a width $\Delta_{\mathrm{g}}\,(d,\sigma)$ determined by Eq.(4.27) (dashed blue lines). The ratio d/σ of the slab thickness over the layer roughness ranges from 0.5 (top curve), 1.0, 2.0, to 4.0 (bottom curve), respectively. (b) Dependence of the width Δ_{g} for the Gaussian profiles on the slab thickness in the error function model. The red solid line gives the exact value according to Eq. (4.27a), the dashed blue line is an approximation in third order Taylor expansion from Eq. (4.27b). (c) Integrated squared deviation $\chi_{\mathrm{GE}}\,(d,\sigma)^2$ according to Eq. (4.28a). The straight line denotes the asymptotic limit given in Eq. (4.28b).

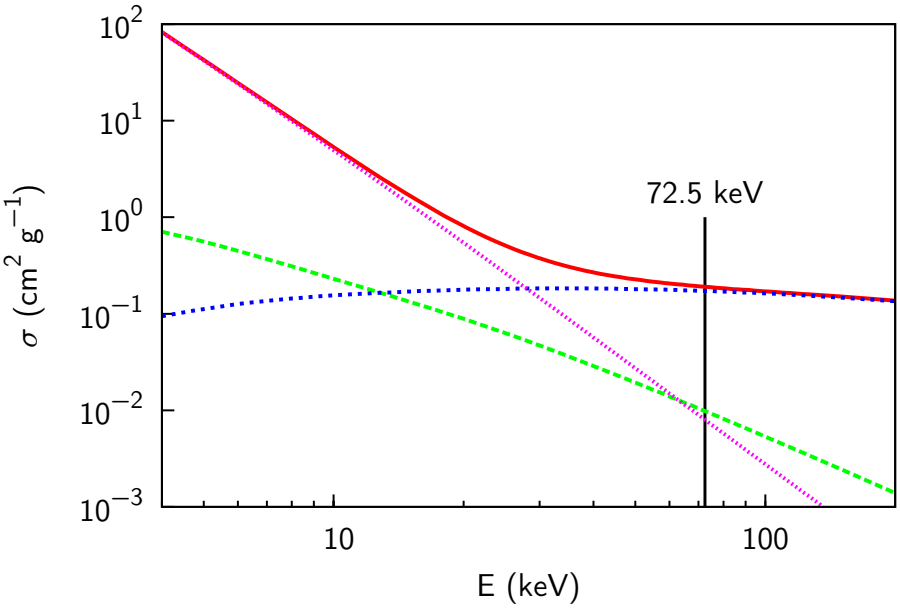

Figure 4.10: Energy dependence of the different contributions to the total x-ray scattering cross section of water. Total attenuation σ_{tot} (solid red line), coherent scattering σ_{coh} (dashed green line), incoherent (Compton) scattering σ_{inc} (short dashed blue line), photoelectric absorption σ_{PE} (dotted purple line). The data were taken from the XCOM photon cross section database from NIST [121]. The vertical line indicates the energy where the experiments were performed.

4.4 The x-ray scattering cross section

Figure 4.10 shows the contributions of the coherent (σ_{coh}, Rayleigh scattering) and incoherent (σ_{inc}, Compton scattering) scattering processes as well as the photoelectric absorption (σ_{PE}) to the total scattering cross section σ_{tot} of x-rays in water. From this data, it is possible to estimate feasibility and suggest further improvements for a given scattering experiment. In the following section, the energy dependence of the signal and the background to the total scattered intensity, which is measured in a reflectivity experiment, is discussed [122, 123].

Apart from the arguments focusing on the scattering from the sample, there are other experimental constraints which are covered in more details in separate sections: The spectral intensity distribution of the synchrotron beamline ID15A is discussed in Sec. 5.1.1, and the x-ray focusing elements in Sec. 5.1.2. Section 5.2.3 addresses the x-ray absorption in the sample cell for the specific experimental setup used in this work as well as other technical aspects concerning the sample environment.

The reflectivity signal

Within the framework of the master formalism Eq. (4.16) one can see directly that the specular reflected intensity $R^2(q_z)$ at a given momentum transfer q_z does not depend on the x-ray energy[17]. Therefore, the optimum energy for a x-ray reflectivity experiment at a deeply buried interface is determined by the absorption of the incident beam and the reflected signal $R^2(q_z)$, the background level, and various other experimental constraints. In the following part of this chapter, the absorption of the signal as well as different scattering contributions to the background originating from the sample are discussed.

Photoelectric absorption and fluorescence

In the transmission-reflection scheme, the x-rays have to penetrate through centimeters of bulk material (e.g. water) before reaching the interface under examination. Figure 4.10 shows that in water at low energies photoelectric absorption is the dominant contribution to the total scattering cross section. In contrast, above $40\,\mathrm{keV}$ which is far above the K edge of oxygen at $0.532\,\mathrm{keV}$ the photoelectric absorption μ_{PE} decreases rapidly and can be neglected.

Photons which are transmitted through the interface can be absorbed in the substrate (silicon) and, after that, excite x-ray fluorescence. These photons have energies below the K edge of the material and are homogeneously distributed over $4\,\pi$. Silicon fluorescence with energy below $1.84\,\mathrm{keV}$ is almost completely absorbed in the silicon sample itself and in the windows of the sample cell. In addition, the single channel analyzer of the detector electronics counts photons between approximately $16\,\mathrm{keV}$ and $100\,\mathrm{keV}$ only.

The incoherent cross section, Compton scattering

Apart from fluorescence, the background signal contains a coherent and an incoherent contribution. In contrast to the photoelectric absorption, the total incoherent Compton scattering cross section of water is almost constant between $20\,\mathrm{keV}$ and $200\,\mathrm{keV}$. In the inelastic scattering process the wavelength λ of the Compton scattered photon is shifted to lower energies.

$$\Delta\lambda = \lambda_{\mathrm{C}}\left(1-\cos 2\vartheta\right) \tag{4.29a}$$

$$\Delta E \approx \frac{\mathrm{d}E}{\mathrm{d}\lambda}\Delta\lambda \tag{4.29b}$$

$$\approx -\frac{E^2}{m_{\mathrm{e}}c^2}\vartheta^2 \approx -\frac{\hbar^2}{4m_{\mathrm{e}}}q^2 \tag{4.29c}$$

For small scattering angles 2ϑ the energy loss ΔE can be approximated by Eq. (4.29c). In the case of the reflectivity experiments shown in this work, the energy shift is always

[17] This statement holds true as long as resonant effects are neglected. In this regime, the relation $f^{(1)} \approx Z$ is valid, and Eq. (4.7a) reduces to its simplified form. For silicon, which is the element with the largest Z used in this work, the K edge is at $1.84\,\mathrm{keV}$, i.e. more than one order of magnitude below the x-ray energy of around $70\,\mathrm{keV}$ used here.

Element	H	C	N	O	F	Al	Si	Cl
Z	1	6	7	8	9	13	14	17
C_Z	0.743	0.823	0.582	0.467	0.376	0.829	0.861	0.540

Table 4.1: Compton factor C_Z.

less than $1\,\mathrm{keV}$. Therefore, Compton scattered photons from both, the water and the silicon substrate, cannot be separated from specular reflected photons and contribute to the background.

For free electrons the differential cross section for Compton scattering $\frac{\mathrm{d}\sigma}{\mathrm{d}\Omega}$ is calculated from the Klein-Nichina formula [124,125]. It exhibits a maximum for scattering with zero momentum transfer ($\vartheta = 0$). For bound electrons in atoms, the scattering in forward direction is mainly coherent and $\frac{\mathrm{d}\sigma_{\mathrm{inc}}}{\mathrm{d}\Omega}$ vanishes. At higher scattering angles 2ϑ, the differential cross section for the incoherently scattered Compton photons increases at the cost of the coherent scattering process. A detailed discussion of incoherent scattering functions can be found in the work of Hubbell et al. [126]. The differential Compton scattering cross section can be estimated[18] from the x-ray atomic scattering form factor $f_0\,(q)$[19] by

$$\frac{\mathrm{d}\sigma_{\mathrm{inc}}}{\mathrm{d}\Omega} = \frac{r_{\mathrm{e}}^2}{4\pi}\left[Z - \frac{f_0\,(q)^2}{Z}\right] . \tag{4.30}$$

For small scattering angles, Eq. (4.30) can be approximated in second order by

$$\frac{\mathrm{d}\sigma_{\mathrm{inc}}}{\mathrm{d}\Omega} = \frac{r_{\mathrm{e}}^2}{4\pi} Z C_Z a_0^2 q^2 \tag{4.31}$$

with the Bohr radius a_0, the Compton factor $C_Z = \frac{\sum_{i=1}^{4} a_i b_i}{8\pi^2 a_0^2 Z}$ and the interpolation coefficients a_i and b_i taken from [127]. The Compton factor depicts how tightly the electrons are bound to the core and therefore determines the probability for an inelastic scattering process. Table 4.1 summarizes the C_Z-values for a selection of elements. Within this approximation, the Compton background increases quadratic with q for small momentum transfer.

The coherent cross section

While the incoherent part of the background depends on the atomic composition of the sample only, the $\boldsymbol{q}$-dependence of the coherent part is governed by the structure of the penetrated material. For crystalline solids, such as the silicon substrate, most of the coherently scattered intensity is highly concentrated in the Bragg reflections[20]. It is therefore

[18] Amongst others, this semi-classical approach neglects the electronic exchange interaction. For details see the work of Henke [109], page 208 and references therein.

[19] In a compound, the electron momentum distribution is affected by the chemical bonds. This leads to slight modifications in the differential Compton scattering cross section.

[20] An example of quasi-coherently scattered intensity from a crystalline solid at finite temperature, which is centered on the Bragg reflections is thermal diffuse scattering (TDS).

easy to identify and does not contribute to the background. In liquids, the coherent differential scattering cross section is proportional to the liquid structure factor $S(q)$, which is the Fourier transform of the radial distribution function (RDF) $G(r)$. Correlations in this distribution depend both, on the intramolecular structure and the intermolecular arrangements within the liquid. For small molecules, such as water with an average distance of $d_{\mathrm{OO}} = 2.8\,\text{Å}$ between two neighboring oxygen atoms [23, 24], the first maximum in $S(q)$ occurs at approximately $q = 2\pi/d \approx 2\,\text{Å}^{-1}$. This is far above the q-range where the measurements shown in this work where performed (for comparison see Sec. 3.1 and Sec. 5.4). On the other hand, the tails from the broad liquid structure factor peaks extend far down to small q-values. Thus, they are the main background source for $q_z \gtrsim 0.5\,\text{Å}^{-1}$[21] (see Fig. 3.4).

[21] For more complex and bulky liquids such as large organic molecules, the nearest neighbor can be in the order of $10\,\text{Å}$ with the first maximum of $S(q)$ at $q \approx 0.6\,\text{Å}^{-1}$ accordingly. As typical structural arrangements at the interface like layering or adsorption have the same vertical length scale, it can be challenging to separate this contributions [128].

Chapter 5

Experimental Details

5.1 X-ray setup

5.1.1 The high energy scattering beamline ID15A at the ESRF

The high energy scattering beamline ID15A [129, 130] is located at the European Synchrotron Radiation Facility (ESRF) in Grenoble, France. It is one of the few beamlines worldwide at a third generation synchrotron source which is optimized for high energy x-rays in the range between $40\,\mathrm{keV}$ and $300\,\mathrm{keV}$ and allows the installation of extensive and bulky user specific setups[1].

The x-ray source

The x-rays are generated in a 7 pole asymmetric multipole wiggler (AMPW, critical energy $44.1\,\mathrm{keV}$, K-parameter 40, magnetic field $B_{\max} = 1.84\,\mathrm{T}$, minimal gap size $20.3\,\mathrm{mm}$). The resulting rms (root mean square) source size is $57 \times 10\,\mu\mathrm{m}^2$ with an rms source divergence of $98 \times 4\,\mu\mathrm{rad}^2$ horizontally and vertically, respectively. In order to reduce the heat load on the optical components (monochromator crystals), the low energy part of the spectrum is removed by a set of permanent filters ($0.7\,\mathrm{mm}$ C, $4.0\,\mathrm{mm}$ Be, $4.1\,\mathrm{mm}$ Al) placed in the white beam. The aluminum absorber cuts almost all intensity below $40\,\mathrm{keV}$. After the filters, a maximum brightness of $3.3 \cdot 10^{14}$ $\left[\mathrm{photons\,mrad^{-2}\,0.1\%\,bw^{-1}}\right]$ per $100\,\mathrm{mA}$ ring current[2] at an energy of around $50\,\mathrm{keV}$ is reached. For $70\,\mathrm{keV}$ ($\lambda = 0.18\,\text{Å}$) photons, used the experiments presented in this work, the brightness drops slightly to approximately $2.8 \cdot 10^{14}$.

[1] Other beamlines where high energy x-rays are available are for example: The beamline ID15B ($60\,\mathrm{keV}$ or $90\,\mathrm{keV}$, fixed), sharing the same x-ray source (AMPW) with ID15A; X17 ($55 - 80\,\mathrm{keV}$), NSLS at BNL, Brookhaven, USA (a second generation synchrotron); GSECARS-13I-C,D ($4 - 45\,\mathrm{keV}$) and XOR/UNI-33-ID-D at the APS, Argonne, USA; I15 ($\approx 100\,\mathrm{keV}$, under construction), Diamond at Rutherford Appleton Laboratory, Chilton, United Kingdom; HEMS ($\approx 40 - 200\,\mathrm{keV}$, in design), Petra at DESY, Hamburg.

[2] Typical ring currents I_{ring} at the ESRF for uniform filling, $2 \cdot 1/3$ filling mode, and hybrid mode are $I_{\mathrm{ring}} = 200\,\mathrm{mA}$ with a lifetime between $60\,\mathrm{h}$ (refill twice a day) for uniform and $35\,\mathrm{h}$ for hybrid mode (refill every $6\,\mathrm{h}$).

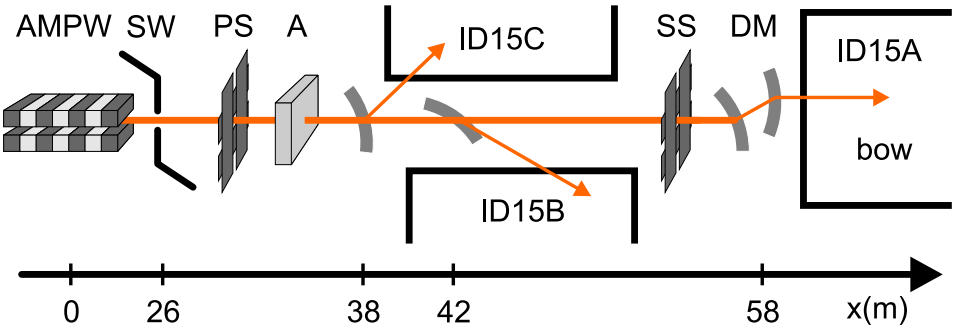

Figure 5.1: Schematic layout of the high-energy beamlines ID15A, ID15C, and ID15B [130]. (AMPW) Asymmetric multipole wiggler; (SW) shield wall; (A) attenuator; (PS) primary slits; (SS) secondary slits; monochromator for ID15C (Laue) and ID15B (Bragg/Laue); (DM) monochromator for ID15A (for this experiment: double Laue).

Beamline optics

The white beam is monochromatized using a double crystal Laue monochromator with two asymmetrically cut and bent Si (111) crystals in fixed exit geometry, located $58\,\mathrm{m}$ after the source. The first monochromator, which is exposed to the white beam, is indirectly cooled with water to remove the heat load. The asymmetric cut of $37.76°$ determines the energy resolution of $\Delta E/E = 2.3 \cdot 10^{-3}$. By bending the monochromator crystals, the beam is made almost parallel in the horizontal direction (see Sec. 5.1.2).

The HEMD setup

The High Energy Micro Diffraction (HEMD) setup [131] is a permanent setup, installed at the backend of the ID15A experimental hutch (bow). It is a highly optimized version of the mobile prototype instrument [9] successfully used in previous experiments [132], [104], [133, 134]. The instrument was constructed, installed, and commissioned recently (August 2004 - February 2005) by the Department Dosch at the MPI for Metals Research as a joint project in cooperation with the ESRF. As the first permanent beamline dedicated to surface sensitive high energy x-ray scattering methods it is also available for external users via the ESRF proposal system. This work represents the first completed project which was entirely performed at the new setup [39, 40].

5.1.2 Beam focusing devices

The beam divergence at a synchrotron source (AMPW at ID15) in the plane of the storage ring (horizontal plane, $98\,\mu\mathrm{rad}$) is much larger than vertically ($4\,\mu\mathrm{rad}$).

In order to reduce the footprint at small incident angles α_i, the beam has to be focused

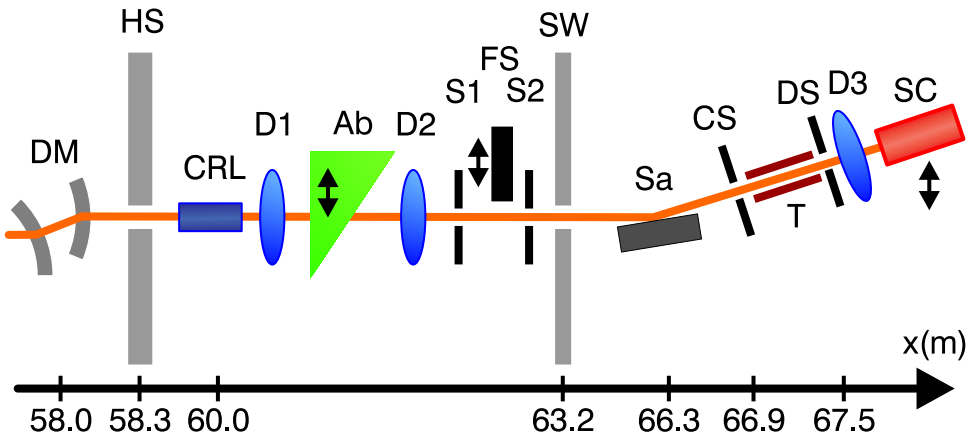

Figure 5.2: X-ray optical elements and beamline setup for high energy reflectivity experiments at ID15A, ESRF (The sketch shows the optimized setup used for recent experiments [40,128].). (DM) double crystal monochromator in Laue geometry; (HS) wall of the experimental hutch ID15A; (CRL) compound refractive lens; (D1) primary beam monitor diode ($t = 0.5\,\mathrm{mm}$); (Ab) absorber wedge of adjustable thickness d (lead glass: thickness $0 \ldots 15\,\mathrm{mm}$, PMMA: $0 \ldots 60\,\mathrm{cm}$); (D2) second monitor diode ($t = 0.3\,\mathrm{mm}$); (S1) first slit set; (FS) fast shutter; (S2) second slit set; (SW) shielding wall reduces, together with the first and second slit set, the background originating from scattering in the CRL and the absorber; (Sa) sample position; (CS) collimator slits; (T) flight tube; (DS) detector slits; (D3) detector diode ($t = 0.5\,\mathrm{mm}$); (SC) scintillation counter (CyberStar, Oxford-Danfysik).

on the sample in the vertical direction. In addition, a smaller beam size at the position of the detector slits allows narrow slit openings, leading to a better signal to background ratio. A standard way of vertical focusing, which is generally employed on surface diffraction beamlines, is the insertion of a bent mirror. At the ESRF, this concept is implemented for example at the beamlines ID1, ID3, or ID23. For high energies such a mirror has to be very long in order to collect the total beam. On the other hand, the bending radius has to be homogeneous over this large area to ensure proper focusing[3]. An alternative way of focusing, which is more suitable for a high energy x-ray beam around $100\,\mathrm{keV}$, is the use of refractive optics. In the experiments shown in this work, focusing was obtained in two dimensions by a compound refractive lens (CRL, approx. $150 - 200$ single lenses[4]) [135]. The coherent interaction of x-rays with matter decreases rapidly for energies $E > E_{1s} \approx R_\infty (Z-1)$. Therefore aluminum lenses are favorable over lighter elements for high energy x-rays[5].

The beam size at the sample position, measured by knife edge scans, was determined

[3] A mirror is currently being tested at ID15A.

[4] For the setup including the lead glass absorber 194 lenses have been used. In recent experiments with the PMMA absorber, a larger focal length was achieved with 174 lenses.

[5] For lower energies lenses are commonly manufactured from beryllium. In the near future a CRL with polymer (PMMA) lenses will be available at ID15A allowing 1D (vertical) focusing.

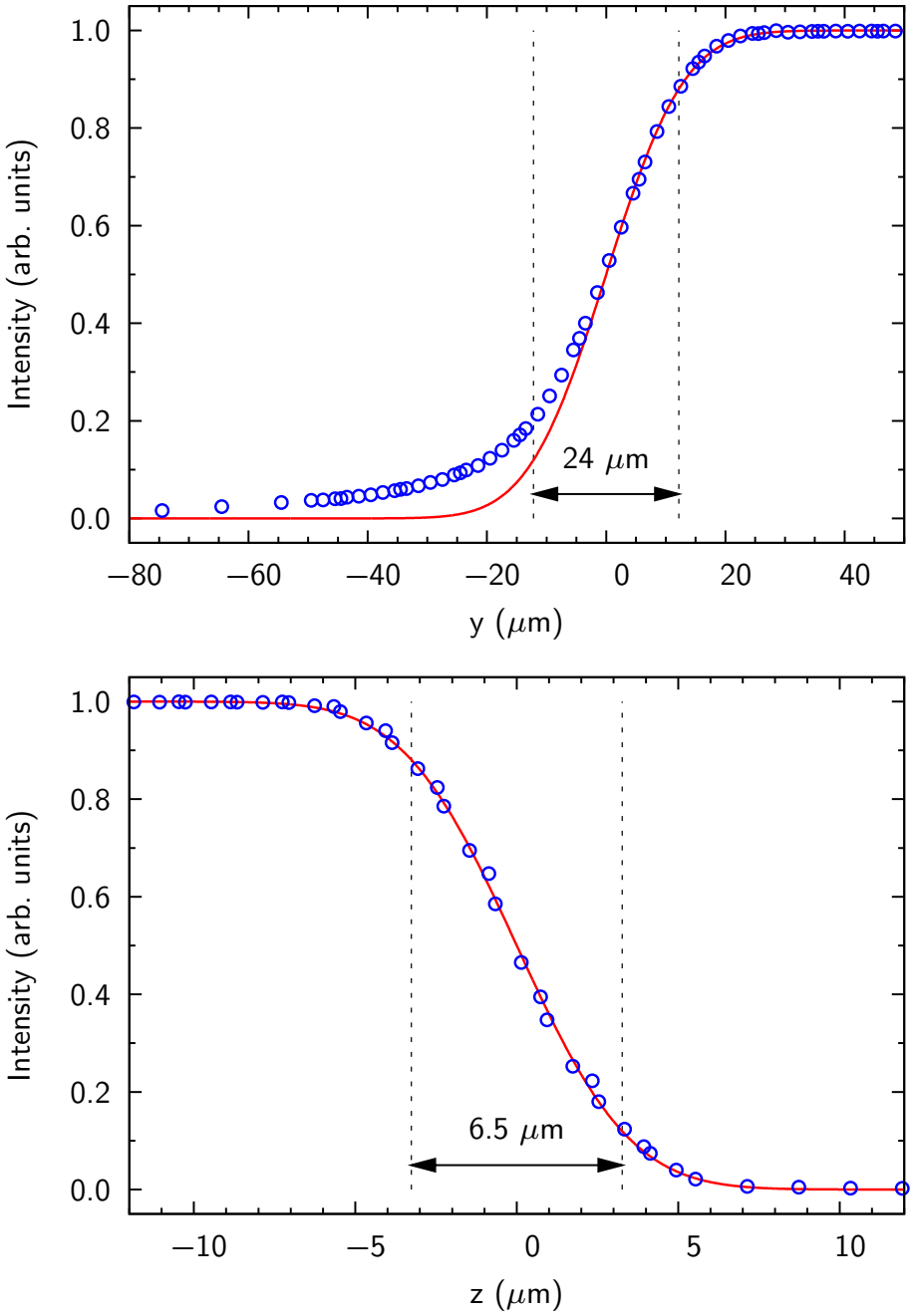

Figure 5.3: Vertical (top) and horizontal (bottom) profile of the x-ray beam measured by a knife edge scan. Fits assuming a Gaussian intensity distribution (solid lines) to the experimental data (circles) give $b_{\mathrm{v}} = 6.5\,\mu\mathrm{m}$ and $b_{\mathrm{h}} = 24\,\mu\mathrm{m}$ for the FWHM (vertical dashed lines) of the vertical and horizontal beam profile, respectively.

to $b_{\mathrm{v}} = 6.5\,\mu\mathrm{m}$ normal (vertical) and $b_{\mathrm{h}} = 25\,\mu\mathrm{m}$ parallel (horizontal) to the sample surface (see Fig. 5.3). The vertical beam width depends strongly on the source size and the stability of the electron beam in the storage ring. Depending on the operation mode of the synchrotron a vertical width between $4\,\mu\mathrm{m}$ and $10\,\mu\mathrm{m}$ can be achieved with the setup described above.

The divergence of the focused beam can directly be measured by a detector scan, using detector slit settings $d \ll \beta l$ to avoid convolution with the slit function (see Fig. 5.4). After focusing, the beam divergence was determined to $\beta_{\mathrm{v}} = 25\,\mu\mathrm{rad}$ and $\beta_{\mathrm{h}} = 43\,\mu\mathrm{rad}$ vertically and horizontally respectively.

5.1.3 The HEMD diffractometer

The main parts of the HEMD diffractometer were custom made by HUBER Diffraktionstechnik GmbH & Co. KG, Rimsting, Germany [136]. It is designed as a six circle diffractometer. In contrast to conventional x-ray diffractometers, the relevant fundamental movements are entirely realized by a combination of linear motions instead of rotations. This allows to achieve the high angular accuracy for the incident ($< 20\,\mu\mathrm{rad}$) and exit diffractometer angle ($< 10\,\mu\mathrm{rad}$), respectively. This precision is essential for reflectivity experiments with high energy x-rays, resulting in very small scattering angles. In addition, the sample position, has to be controlled very precisely in the vertical ($< 1\,\mu\mathrm{m}$) and horizontal ($1\,\mu\mathrm{m}$) direction for micro-beam experiments.

5.1.4 Detector systems

PIN diode

Three Eurisys p/n diodes (Si), connected to a Keithley current amplifier, serve as monitor counters and high intensity signal detector. From the measured diode current I_{PIN} the absolute flux N_{ph}, i.e. the number of photons per second, can be calculated directly by

$$N_{\mathrm{ph}} = \frac{I_{\mathrm{PIN}} E_{\mathrm{g}}}{eE} \left(1 - e^{-\mu_{\mathrm{en}} t}\right)^{-1} \quad . \tag{5.1}$$

$E_{\mathrm{g}} = 3.6\,\mathrm{eV}$ denotes the average energy for the excitation of an electron hole pair by photoabsorption, t the diode thickness, and μ_{en} the energy absorption coefficient[6]. Figure 5.7 shows the photon flux of a PIN diode versus the x-ray energy E. For the detector diode with a thickness of $0.5\,\mathrm{mm}$[7] a current of $1\,\mathrm{nA}$ corresponds to a total flux of $3.2 \cdot 10^7\,\mathrm{photons\,s^{-1}}$. Considering a dark current of $10\,\mathrm{pA}$ and a primary flux of $1 \cdot 10^{11}\,\mathrm{photons\,s^{-1}}$ the effective dynamic range of the detector diode is approximately five orders of magnitude.

[6] Values for the mass energy absorption coefficient $\frac{\mu_{\mathrm{en}}}{\rho}$ can be found in the NIST database [137].

[7] As it is exposed to the un-attenuated beam only, the thickness for the monitor diode can be either $0.3\,\mathrm{mm}$ or $0.5\,\mathrm{mm}$. A thinner diode leads to slightly smaller detection sensitivity but less absorption of the primary beam.

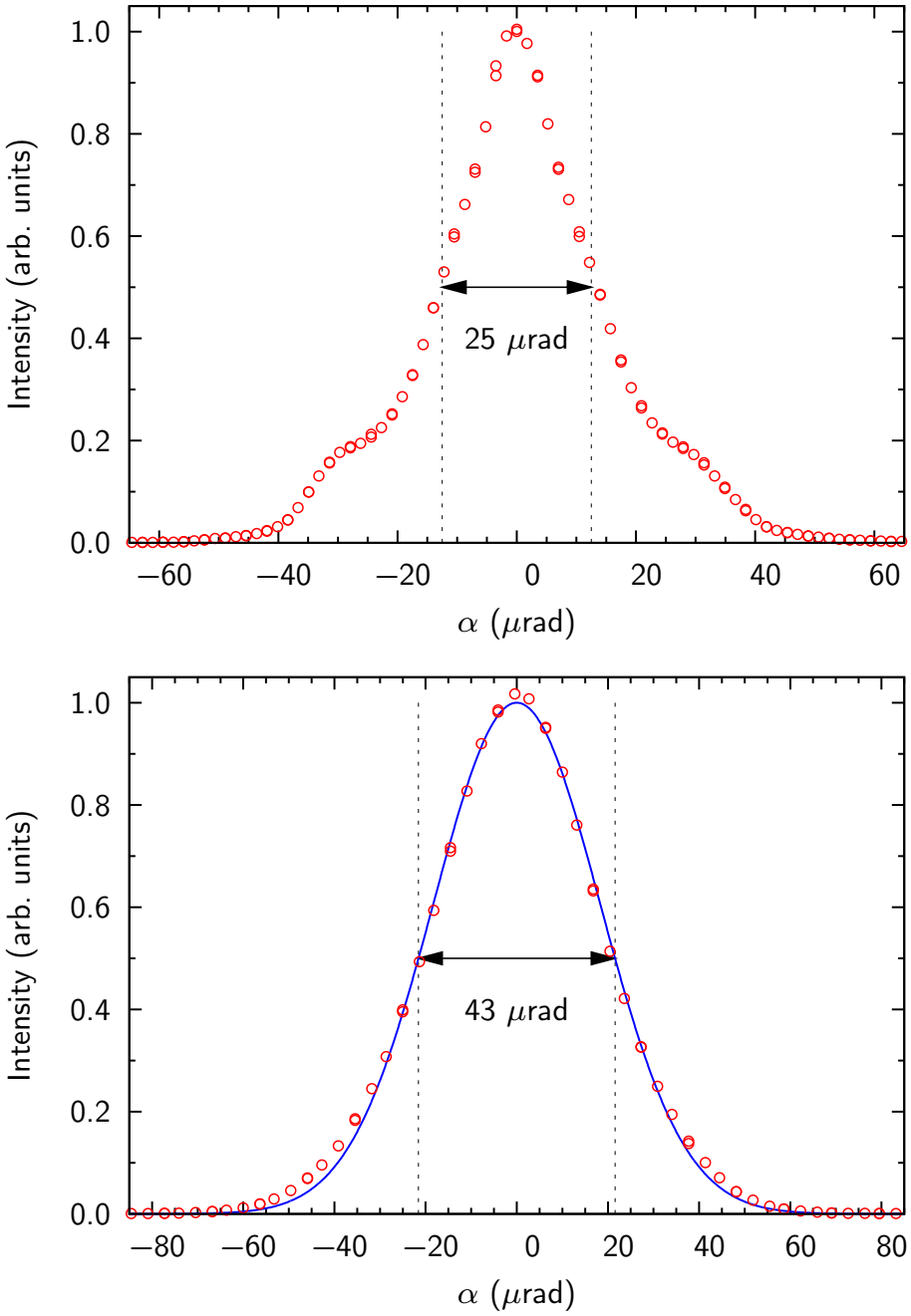

Figure 5.4: Vertical (top) and horizontal (bottom) divergence β of the x-ray beam measured by detector scans. Fits (solid lines) to the experimental data (circles) give $\beta_\mathrm{v} = 25\,\mu\mathrm{rad}$ and $\beta_\mathrm{h} = 43\,\mu\mathrm{rad}$ for the FWHM (vertical dashed lines) of the vertical and horizontal beam divergence, respectively.

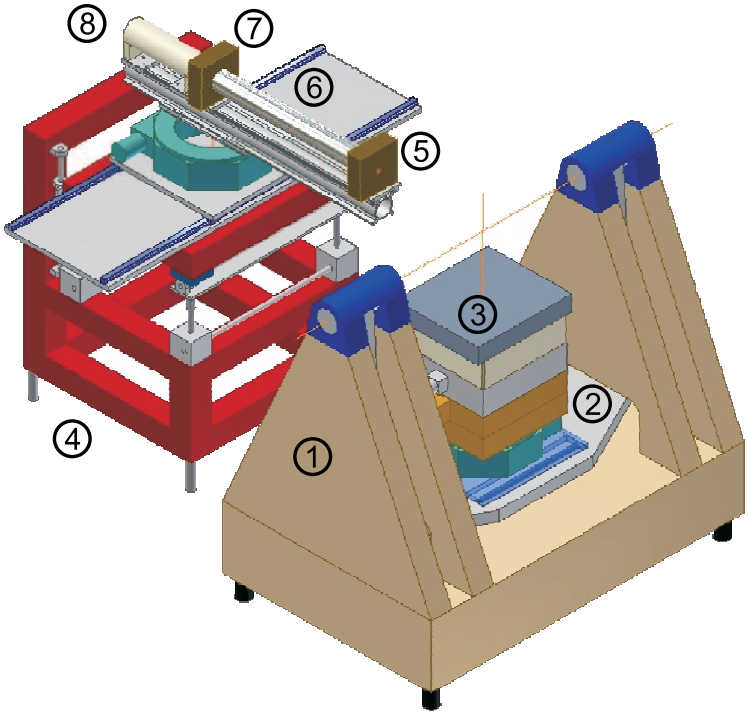

Figure 5.5: Design drawing of the HEMD instrument: (1) Granite base; (2) Swing; (3) Sample tower; (4) Detector stage; (5) Collimator slits; (6) Flight tube; (7) Detector slits; (8) Scintillation counter. (courtesy of F. Adams)

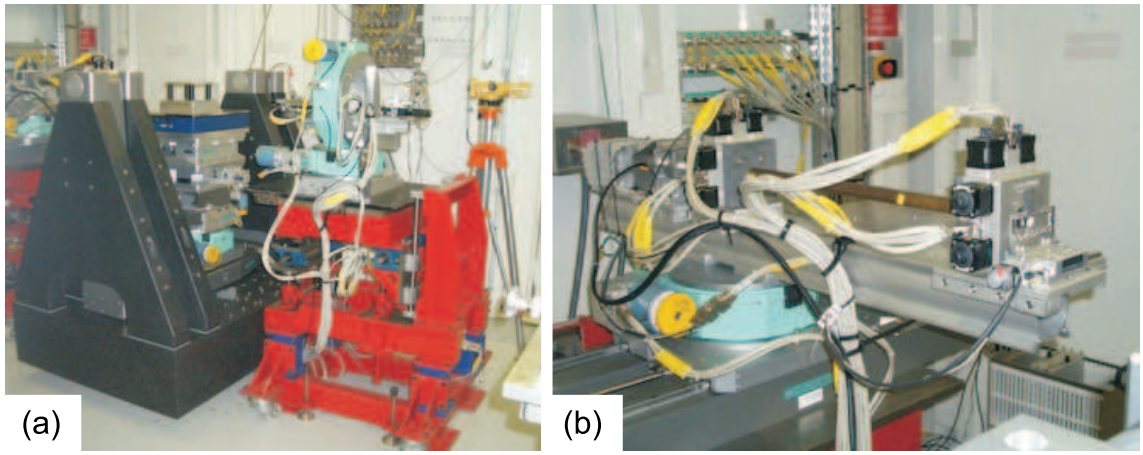

Figure 5.6: Photography of the HEMD instrument. (a) The heavy-duty sample tower for high accuracy positioning is mounted on a granite base for high stability. The additional pair of monochromators (green circle on top of the red table) which allow tilting the incident x-ray beam was not used in this work (for details see [60]). (b) The detector stage is designed as a completely independent assembly.

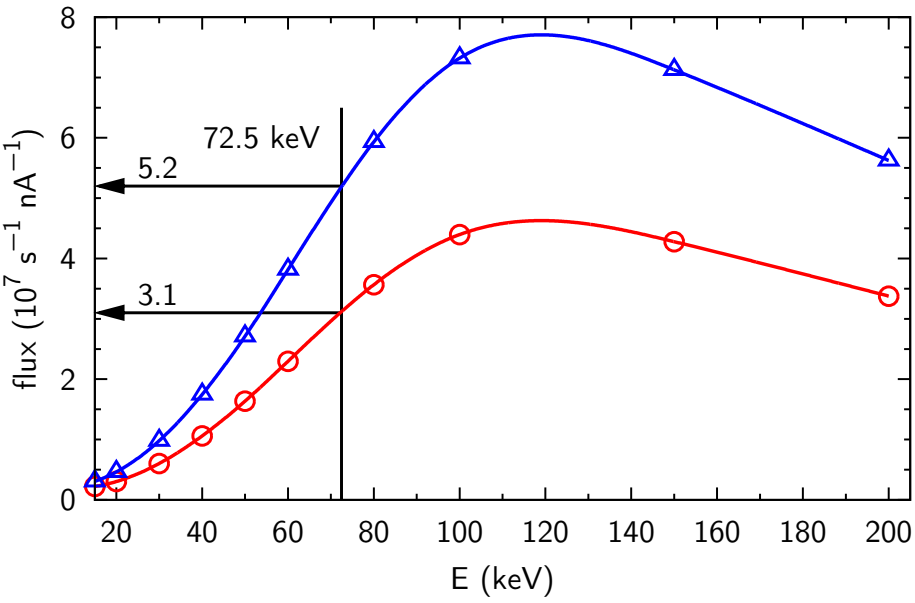

Figure 5.7: Photon flux in $10^7\,\mathrm{photons\,s^{-1}}$ per $1\,\mathrm{nA}$ diode current for a Si diode with a thickness of $t = 0.5\,\mathrm{mm}$ (red circles, D1 and detector diode D3) and $t = 0.3\,\mathrm{mm}$ (blue triangles, monitor diode D2). The detection efficiency for $72.5\,\mathrm{keV}$ photons is similar to the third harmonics at $217.5\,\mathrm{keV}$.

Scintillation counter

For single photon counting a $5\,\mathrm{mm}$ thick, thallium activated, NaI scintillation counter with a $0.2\,\mathrm{mm}$ thick Beryllium window[8] is available. It can be moved sideways for measurements of high intensities with the PIN diode. Due to the thick scintillation crystal, the conversion efficiency for photons around $70\,\mathrm{keV}$ is still more than 99%. The measured count rates N have to be corrected for dead-time. A good approximation for the correction factor is

$$N_{\mathrm{corr}} = \frac{N}{(1 - N\tau)}\,, \tag{5.2}$$

which is applicable for intensities well below the detector saturation. The dead-time constant τ can be determined by fitting the detected count rate to the incident flux. Figure (5.8) was recorded by moving the PMMA wedge absorber (see Sec. 5.1.5) gradually out of the primary beam. By converting the absorber position into the incident flux, one obtains a dead-time constant of $\tau = 0.68\,\mu\mathrm{s}$. Indicated by the significant deviation from the calculated curve for count rates larger than approximately $300000\,\mathrm{cps}$, the detector signal does not follow this simple relation anymore. In this work, count rates were limited to values less than $150000\,\mathrm{cps}$, where the correction factor is in the order of 10 %.

[8] CyberStar CBY48NA05B scintillation counter; Oxford Danfysik.

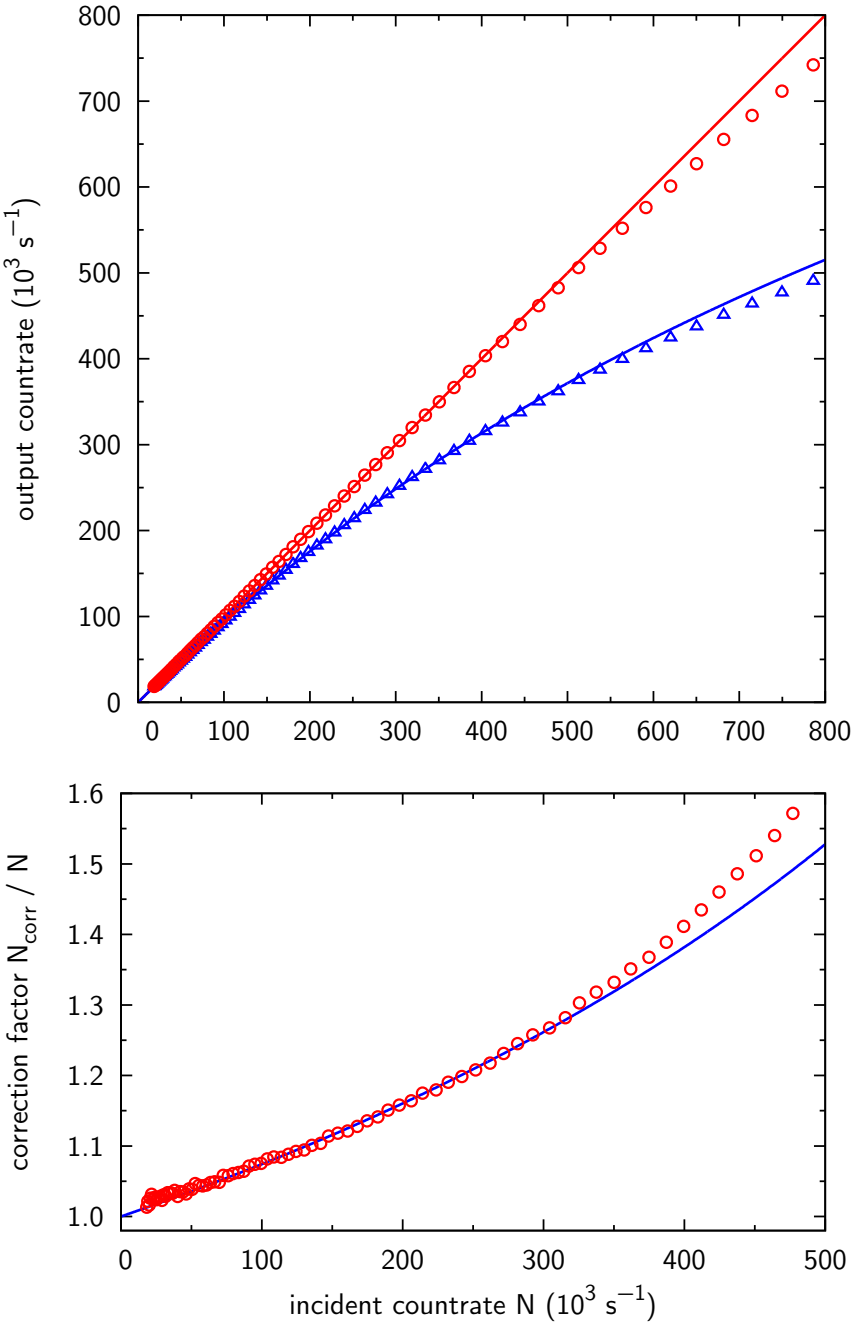

Figure 5.8: Dead-time correction for the Cyberstar scintillation counter. The incident flux was adjusted by the PMMA wedge absorber. (top) Measured count rate N (blue triangles) and corrected data points N_{corr} (red circles) using Eq. (5.2) with a dead-time constant $\tau = 0.68\,\mu\mathrm{s}$ obtained from fitting (solid blue line). The corrected count rate follows a straight line with slope unity up to approximately $300000\,\mathrm{cps}$. (bottom) Correction factor N_{corr}/N versus detected count rate.

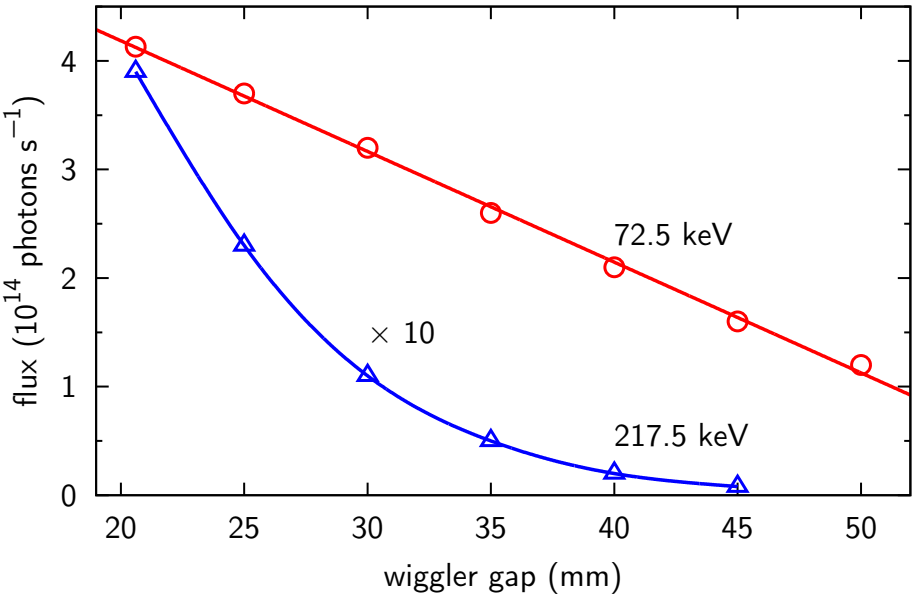

Figure 5.9: Photon flux versus the gap size of the wiggler for $E_0 = 72.5\,\mathrm{keV}$ (red circles) and the third harmonic at $3E_0 = 217.5\,\mathrm{keV}$ (blue triangles, magnified by a factor of 10) from the AMPW at ID15, ESRF [138].

5.1.5 Absorber

As discussed above, the maximum count rate of the scintillation counter is limited to approx. $300000\,\mathrm{cps}$. In contrast, the dynamic range of the reflectivity measurements performed in this work, spans about 9 orders of magnitude. Therefore, the x-ray beam has to be attenuated at high intensities, i.e. in the primary beam and for small scattering angles 2ϑ[9].

Absorber material and beam hardening

At small wiggler gap openings (maximized photon flux), the AMPW of ID15 delivers a beam with contaminations of about 10 % from higher harmonics. For the setup at ID15A used in this work, the contaminations of the primary beam are in the order of 10^{-3}. The intensity ratio between the x-rays with wavelength λ and $\lambda/3$ is affected by the oscillation amplitude of the electrons in the insertion device i.e. the opening of the wiggler gap, and the beamline optics. As shown in Fig. 5.9, increasing the nominal value of $20.3\,\mathrm{mm}$ can suppress the higher harmonic contaminations at the cost of a significantly reduced flux. As the K-parameter of the AMPW is comparatively high (see Sec. 5.1), the ratio $I_\lambda / I_{\lambda/3}$ decreases much slower with an increased wiggler gap compared to undulator beamlines,

[9] For reflectivity measurements absorbers have to be used in the range $q_z \lesssim 0.2\,\mathrm{Å}^{-1}$ (see Sec. 5.4.1).

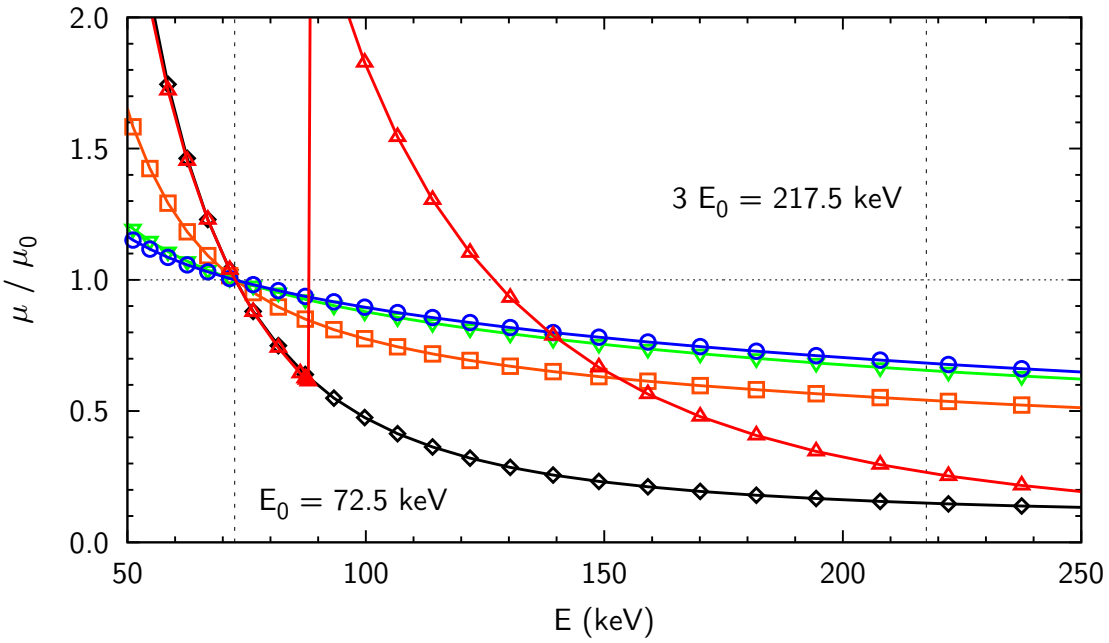

Figure 5.10: Comparison between the energy dependence of the relative linear absorption coefficient $\frac{\mu(E)}{\mu(E_0=72.5\,\mathrm{keV})}$ for different absorber materials. Pb ($\mu_\lambda = 34\,\mathrm{cm}^{-1}$, red triangles up), Cu ($\mu_\lambda = 8.6\,\mathrm{cm}^{-1}$, black diamonds), Al ($\mu_\lambda = 0.60\,\mathrm{cm}^{-1}$, orange squares), H_2O ($\mu_\lambda = 0.19\,\mathrm{cm}^{-1}$, green triangles down), PMMA ($\mu_\lambda = 0.22\,\mathrm{cm}^{-1}$, blue circles). The dashed line at $3E_0 = 217.5\,\mathrm{keV}$ corresponds to the third harmonic. Minimum beam hardening is achieved by low Z materials like H_2O or PMMA where Compton scattering is the dominant absorption mechanism (The Compton cross section is almost constant at high energies.).

operating at energies around $10\,\mathrm{keV}$. As the Darwin width of a perfect single crystal (silicon monochromator) decreases with energy, higher harmonics are reduced by detuning the two monochromator crystals, which also leads to a significantly reduced flux. In contrast, the aluminum CRL lead to a relative increase of $I_{\lambda/3}$.

The transmission $T = \exp\left[\mu\left(E\right)d\right]$ through an absorber depends strongly on the photon energy E. Figure 5.10 shows the linear absorption coefficient μ for a selection of materials. When the primary beam has negligible contaminations with higher harmonic x-rays, the absorber material can be chosen for optimal machining properties, as well as convenient dimensions and weight[10]. Due to the significant amount of higher harmonics in the x-ray beam at ID15A, the absorption at the third harmonic $\mu_{\lambda/3}$ compared to μ_λ has

[10] At conventional surface diffraction beamlines higher harmonics are removed by a mirror as discussed above. Typical absorbers comprise a set of thin metal foils with different thicknesses, which can be inserted in the primary beam. Pneumatic systems allow a quick exchange of the absorber foils, consecutively arranged within an absorber box.

to be as high as possible to avoid a relative increase of $I_{\lambda/3}$ (*beam hardening*).

Lead glass absorber

In this work, a lead glass[11] absorber was used. It has a wedge like shape with an angle of $15.26°$ and a maximum thickness of $15\,\mathrm{mm}$. The K edge of lead at $E_K^{\mathrm{Pb}} = 88.0\,\mathrm{keV}$ gives rise to strong increase in the photoelectric absorption between E_0 and the third harmonic $3E_0$. This significantly reduces the beam hardening compared to a cooper absorber (K edge at $E_K^{\mathrm{Cu}} = 8.99\,\mathrm{keV}$), of approximately the same size. Polished side surfaces guarantee a continuous adjustable absorption upon moving the wedge horizontally in the x-ray beam. Figure 5.11a shows the transmitted intensity versus the thickness. The transmitted intensity (red circles) was measured with the detector PIN diode D3, while moving the absorber wedge. X-rays with $E_0 = 72.5\,\mathrm{keV}$ are absorbed strongly with a half value thickness of $d_\lambda = 630\,\mu\mathrm{m}$ (steep straight blue line), whereas the transmission of the third harmonic contaminant is much higher ($d_{\lambda/3} = 3400\,\mu\mathrm{m}$, shallow straight blue line). For the lead glass absorber already at an absorption factor of only 10^{-3} the detected intensity at the energy $3E_0$ is in the same order of magnitude as the fundamental.

PMMA absorber

In recent experiments [128], a Plexiglas (PMMA[12]) absorber was used (see Fig. 5.11b). Compton scattering, which varies only slightly in this energy range, is the most dominant loss mechanism for light elements like hydrogen, carbon, and oxygen at energies above E_0 (see Sec. 4.4 and Fig. 5.10). Therefore, there is no beam hardening problem for absorption factors down to 10^{-5} as shown in Fig. 5.11b. A drawback is the large half value thickness of $29\,\mathrm{mm}$ leading to a total absorber length of $600\,\mathrm{mm} \approx 20\,d_\lambda$ in order to reduce the transmission to 10^{-6}. While the lead glass absorber can be mounted conveniently at almost every position in the beam path, the PMMA absorber (total weight approx. $10\,\mathrm{kg}$) has to be placed on a much larger translation stage.

Fast shutter

In order to minimize the radiation damage on organic molecules, a fast shutter was mounted in the beam path. Implemented in the beamline control system, the shutter opens automatically $0.2\,\mathrm{s}$ before a counting command is sent to the detector electronics.

[11] Lead glass RD50, lead oxide content (PbO) $\geq 65\%$; Schott AG, Grünenplan.
[12] Polymethyl methacrylate, $(\mathrm{C_5O_2H_8})_n$, density $\rho = 1.19\,\mathrm{g\,cm^{-3}}$

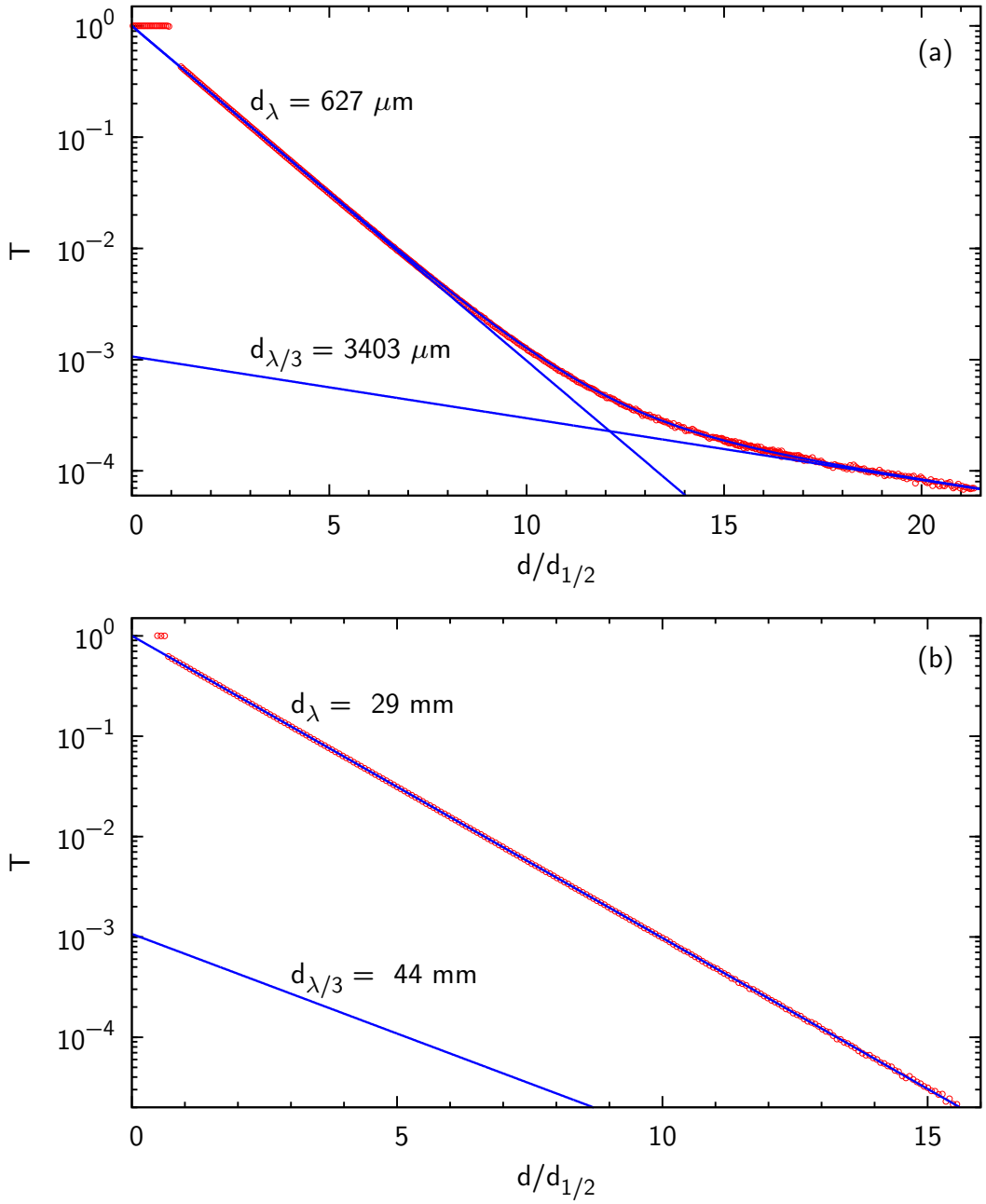

Figure 5.11: Comparison of the transmission T (red circles) versus the normalized thickness d/d_λ between the two absorbers employed in the reflectivity experiments at ID15A. (a) Lead glass absorber with a half value thickness of $d_\lambda = 630\,\mu\mathrm{m}$. The half value thickness $d_{\lambda/3}$ of the third harmonic is much larger than d_λ leading to a significant beam hardening for $T < 10^{-3}$ i.e. $d > 10\,d_\lambda$. (b) PMMA, $(\mathrm{C_5O_2H_8})_n$ absorber ($d_\lambda = 29\,\mathrm{mm}$). Due to the low Z elements, the beam hardening is negligible for $T > 10^{-5}$.

5.2 Sample environment

5.2.1 Materials and cleaning procedures

Impurities are a major issue in experiments dealing with surfaces and interfaces. Even minute quantities of impurities in a bulk system are sufficient to segregate at least one monolayer at an interface. When they are preferentially adsorbed at the surface or interface under observation, these experiments are very likely extremely sensitive to contaminations. Contaminants are introduced by mainly two sources. There are impurities which are already present in the basic materials (here mainly the water), and additional contaminants, originating from the sample preparation and handling. Therefore it is essential to use inert materials for all parts of the inner sample cell in direct contact with the water and the hydrophobic substrate. Suitable materials for the sample cell are glasses with high water stability like Schott Duran glass which can be cleaned thoroughly and do not emit compounds such as plasticizers. Quartz glass would be a preferable material as it is made of SiO_2 only, and therefore no metal ions can be dissolved in the water. On the other hand, amorphous SiO_2 is difficult to machine and has a high transformation temperature.

All glass and quartz parts can be cleaned routinely in an ultrasonic bath, filled with an alkaline detergent. Thorough rinsing, and immersing the parts in ultra pure water over night ensures that most of the ionic contaminants are removed from the glass surface.

Fluorinated polymers like PTFE (Teflon) or PFA can be cleaned in strongly oxidizing solutions like freshly prepared Piranha (1 part H_2O_2 35%, 3 parts H_2SO_4 98%) or chrome-sulfuric acid for $30\,\mathrm{min}$ (for details see Sec. 5.3). The drawback is that the highly hydrophobic PTFE surface has a micro porous structure, in which impurities can withstand cleaning procedures much more easily compared to a smooth glass surface. Furthermore, electro-statically charged materials like PTFE tend to attract dust from the air. As the setup was partially assembled directly at the synchrotron in the experimental hutch, i.e. in a relatively dirty environment, contaminants may enter the setup when it is not tightly sealed for a longer period. Polymers containing only carbon and hydrogen (e.g. polyethylene (PE) or polypropylene (PP)) can be machined much more preciously than the supple PTFE. This is important for fittings in glass grindings, or for the screws fixing the hydrophobic substrate. PE and PP components can be cleaned in analogy to glass parts[13].

5.2.2 Choosing optimum sample dimensions

The angles in high energy x-ray scattering experiments are much smaller than the corresponding ones in experiments at conventional energies. The increased beam footprint on the sample can be partially compensated by focusing the beam (see Sec. 5.1.1). Footprint correction factors can, in principle, accommodate for the part of the beam which does not hit the sample (see Sec. 5.4.2). However, if the sample is even slightly misaligned, with the sample height as the most critical parameter, the sample can move out of the center of

[13] PE or PP can not be cleaned in Piranha. These polymers get oxidized completely in an explosive reaction.

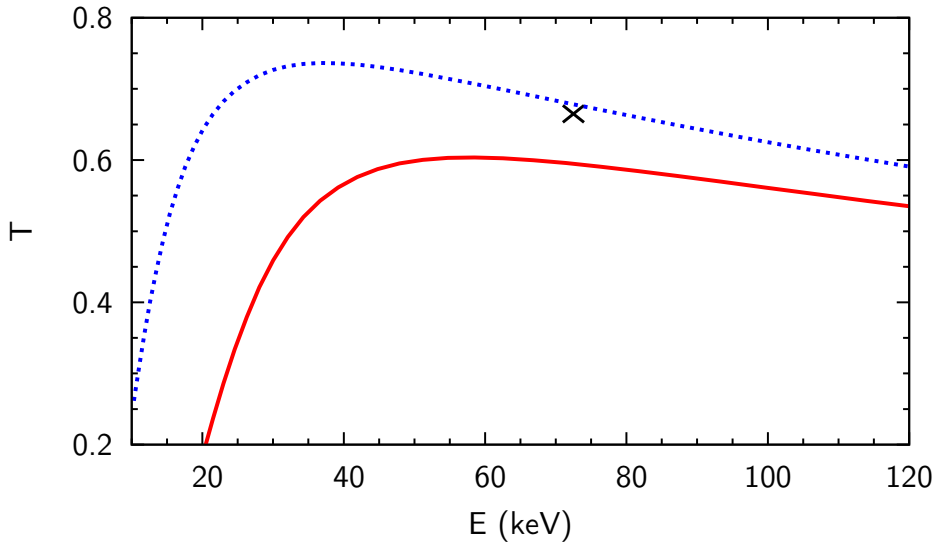

Figure 5.12: X-ray transmission through the sample (dashed blue line) and the total setup (solid red line) as a function of the x-ray energy E. The sample is considered as a water slab of thickness $d = b_\mathrm{v}/\alpha_\mathrm{c}$, assuming a vertical beam size of $b_\mathrm{v} = 10\,\mu\mathrm{m}$. The total setup consists of the sample, a glass (SiO_2) entrance and exit window with a thickness of $0.5\,\mathrm{mm}$ each, and an additional space of $1\,\mathrm{mm}$ between the two windows and the sample, respectively. Absorption coefficients μ where taken from the NIST database [110]. The cross ($\times$) denotes the measured transmission through the sample chamber filled with water.

the incident beam, leading to significant errors in the recorded reflection pattern. Also, a non-Gaussian intensity distribution of the x-ray beam can hinder a fully quantitative footprint correction. Therefore, as a rule of thumb, the sample size should be approximately the FWHM of the footprint at α_c, the critical angle of total reflection. An increase in x-ray energy leads to a linear increase in the sample size, as the critical angle of refraction $\alpha_\mathrm{c} \approx \lambda\sqrt{r_\mathrm{e}/\pi\rho_\mathrm{e}}$ is roughly proportional to the wavelength. For a vertical beam size of $b_\mathrm{v} = 6.5\,\mu\mathrm{m}$, an energy of $70\,\mathrm{keV}$ and an electron density of $\rho_\mathrm{e} = 2.0 \cdot 10^{11}\,\mathrm{cm}^{-3}$ for the silicon substrate, one gets a sample length of $15\,\mathrm{mm}$ for reflectivity experiments in air and $21\,\mathrm{mm}$ for measurements in water.

Taking into account, that the sample length increases with the x-ray energy, the transmission through the sample with thickness $d\,(E) = b_\mathrm{v}/\alpha_\mathrm{c}\,(E)$ is given by

$$T = e^{-\mu(E)d(E)}\,. \tag{5.3}$$

The dashed blue curve in Fig. 5.12 shows the transmission through a water slab according to Eq. (5.3). In the energy region where the Compton scattering cross section of water is the dominant contribution to the total absorption ($E > 30\,\mathrm{keV}$), the decrease in the absorption coefficient can not compensate for the larger sample size. Note here, that the absorption is not only caused by the sample. Entrance and exit windows, as well as the

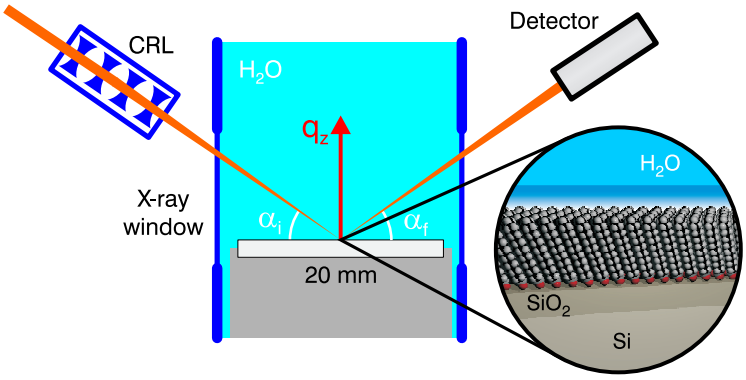

Figure 5.13: Sketch of the experimental setup. The microfocused high energy x-ray beam penetrates the sample cell from the side illuminating only the interface to be studied. The x-ray beam is reflected from the interface and detected by a scintillation counter. Zooming in at the interface, a sketch of the structure of the OTS-SAM in contact with water is shown.

space between the windows and the sample edge, which in this setup is also filled with water, contribute significantly to the total absorption (red solid line in Fig. 5.12).

Furthermore, an increased path length of the x-ray beam penetrating the sample leads to an increase in the background level due to bulk water scattering (see Sec. 4.4). Considering all those constraints, a sample size of $20\,\mathrm{mm}$ is a good compromise between the conflicting requirements. The measured transmission though the cell filled with water at $72.5\,\mathrm{keV}$ is 67 %, which is slightly higher than the calculated value.

5.2.3 Cell design

Glass chamber

The main part of the sample cell is a cylindrical glass tube[14] (see Fig. 5.13 and 5.14). In order to connect the cell to different types of adaptors or caps for sealing, the top part is equipped with a GL45 glass thread. At the bottom, the tube ends with a NS45/40 norm grinding, which fits on top of the sample holder. Two planar glass slides, molded parallel into the cell and spaced by $22\,\mathrm{mm}$ from each other, serve as windows for the high energy x-ray beam. In the region where the x-ray beam penetrates the windows, the glass slides are polished to a thickness of $0.5\,\mathrm{mm}$ over a height of $10\,\mathrm{mm}$. The advantage of a rectangular cross section of the cell at the position of the windows is the constant length of the beam path through water and therefore a constant signal absorption and background level when moving the sample sideways.

Sample mount

The sample has to be mounted on a holder to ensure its stability on a $\mu\mathrm{m}$ scale over the whole duration of the experiment (up to $2\,\mathrm{h}$). On the other hand, the thin Si substrate

[14] Laboratory glass, Schott Duran, No. 8330

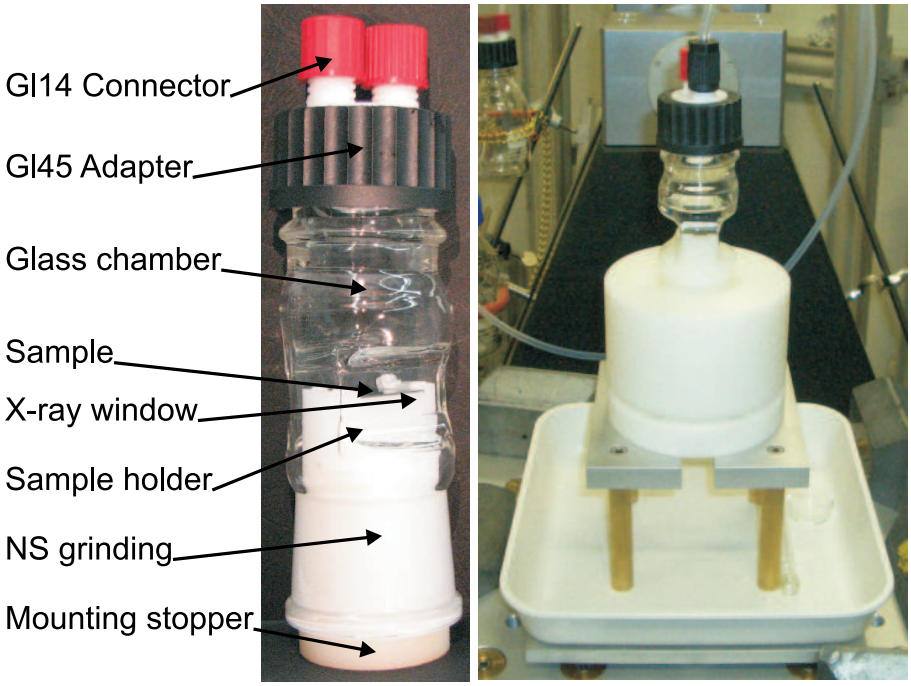

Figure 5.14: (left) Completely mounted sample cell. (right) Sample is mount on top of the HEMD diffractometer.

(thickness $625\,\mu\mathrm{m}$) bends when tightened too strongly, leading to undefined incident (α_i) and exit (α_f) angles, respectively. Figure 5.15 shows the two parts of the sample mount. The Si substrate ($20\,\mathrm{mm} \times 25\,\mathrm{mm}$) is clamped on the rectangular notch of the sample holder (see Fig. 5.15a) by four M3 PTFE screws. By the stud on the bottom of the holder, it can be nested on the mounting stopper (see Fig. 5.15b). Two holes (diameter $1.5\,\mathrm{mm}$ each) are used for filling and emptying the cell with water. Each hole ends in a $\mathrm{G}1/8''$ pipe thread to connect the fittings of the PFA tubes. The middle part of the mounting stopper (indicated by the light grey part in Fig. 5.15b) follows the conical shape of a NS45/40 norm grinding[15]. Both, the sample holder and the mounting stopper are made of PE. For sealing the connection between the grinding of the glass cell and the PE a conical Teflon sleeve[16] is imposed on the mounting stopper.

5.2.4 Vacuum and water handling

The experimental setup including the sample cell and the equipment for vacuum and water handling is shown in Fig. 5.16. Vacuum was applied, both for the preparation of degassed water and to fill and empty the experimental chamber. It was generated by a three-stage

[15] Base diameter $45\,\mathrm{mm}$, height $40\,\mathrm{mm}$, gradient 1:10 corresponding to an angle of $2.86°$ and a top diameter of $41\,\mathrm{mm}$.

[16] Teflon sleeve, thickness $0.1\,\mathrm{mm}$

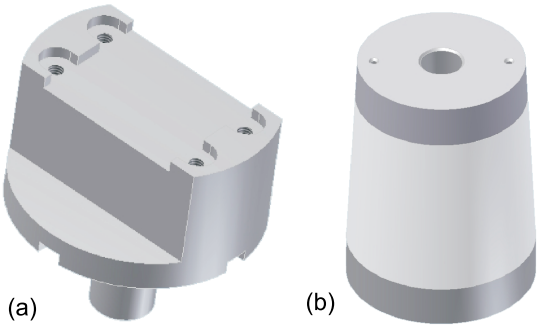

Figure 5.15: Design drawings of the sample holder (a) and mounting stopper (b). The light grey area indicates the region where the mounting stopper has a conical shape in accordance to an NS45/40 norm grinding.

diaphragm pump[17]. To avoid condensation of water vapor inside the pump, a drying cylinder filled with approximately $500\,\mathrm{g}$ blue or orange gel[18] was added. A gas washing bottle[19] ensures that no contaminations from the drying gel and the pump can enter the vacuum system and thus the sample cell. All tubing with direct contact to the chamber was made of PFA. For connections between the pump, the drying cylinder, and the gas washing bottle PE tubes were used. For details on the preparation of degassed and gas enriched water see Sec. 5.3.3.

The top of the sample cell can be tightly sealed by any GL45 screw cap or adaptor. In this work, a PTFE multiple distributor, equipped with GL14 connectors[20] (see Fig. 5.14), was used. The water was sucked from the reservoir by low-pressure directly into the sealed sample cell by carefully opening valves 2 and 4. By this method, any contact of the degassed water with air was avoided while filling the chamber is avoided. For filling the cell with gas enriched water, the vacuum bottle with the stirring rod was replaced by a container filled with the corresponding liquid.

5.3 Sample preparation

5.3.1 Substrate preparation

Silicon substrates

Self-assembled monolayers (SAMs) of octadecyl-trichlorosilane (OTS) were grafted on silicon substrates covered with a native oxide layer. Pieces with a size of $20\,\mathrm{mm} \times 25\,\mathrm{mm}$ were cut from (100) oriented Si-wafers[21]. The sample edges were polished with abrasive

[17] Volume flow rate $3.3\,\mathrm{m^3h^{-1}}$, ultimate vacuum $2\,\mathrm{mbar}$; Vacuubrand GMBH, Wertheim

[18] Silica gel with moisture indicator; Merck, Darmstadt

[19] Gas washing bottle (Schott Duran) with size 1 porosity for gas distribution in liquids. The bottle was filled with a mixture of water and particles of fumed silica (particle size $0.012\,\mu\mathrm{m}$, surface area $200\,\mathrm{m^2g^{-1}}$, CAS: 112945-52-5, Aldrich)

[20] PTFE BOLA-Multiple Distributors for Bottles; Bohlender GmbH, Grünsfeld

[21] Thickness $625\,\mu\mathrm{m}$, p-type boron, $10 - 20\,\Omega\mathrm{cm}$. The $5''$ ($\varnothing\,125\,\mathrm{mm}$) silicon wafers, used in this work, were kindly supplied by P. Dreier, Siltronic AG, Burghausen/Munich

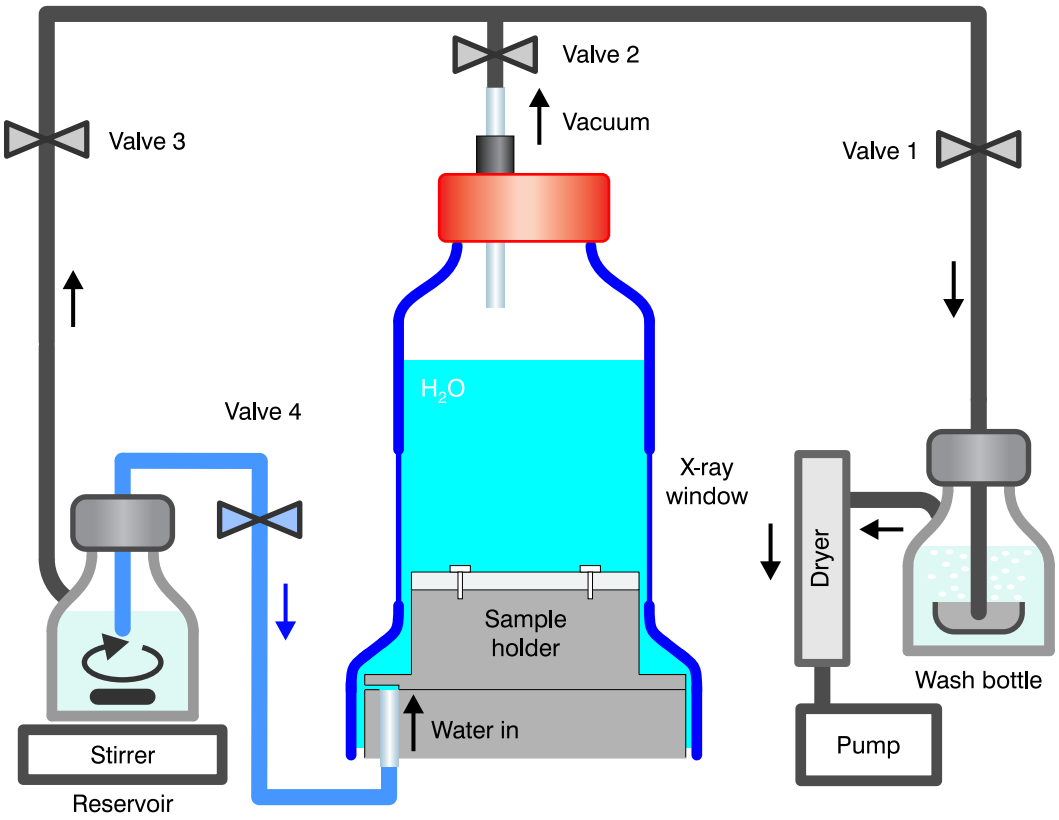

Figure 5.16: Experimental setup with equipment to fill and empty the cell. Degassed water was prepared in-situ in the reservoir by heavy stirring under vacuum.

paper[22] to avoid parasitic scattering at small incident angles α_i.

Substrate cleaning

Prior to functionalization with SAMs, the surface has to be cleaned from residues and prepared with an OH surface termination. Most of the contamination, mainly introduced by wafer cutting and edge polishing, can be removed by cleaning the substrate in a series of solvents. There are various ways of preparing a hydrophilic OH surface termination [139] for the subsequent anchoring of the organo-silanes. Abrasive processes like etching in an alkaline aqueous solution (KOH), the RCA1+RCA2 cleaning procedure[23], or plasma

[22] SiC abrasive paper, grit 2400, grain size 8 μm; Struers, Willich

[23] In the RCA cleaning procedure the oxide is striped by a HF dip and subsequently grown fresh using a wet chemistry process. The oxide grown under wet conditions is much more inhomogeneous, less dense, and with a higher surface roughness than the one grown in dry environment by the wafer manufacturer.

cleaning in an Ar/O_2 atmosphere produce strongly hydrophilic surfaces. These preparation methods lead to a significant increase in the surface roughness of the native oxide layer on top of the silicon substrate. As an alternative, the sample can be etched in Piranha. Piranha is a mixture of hydrogen peroxide with concentrated sulfuric acid (1 part H_2O_2 35%, 3 parts H_2SO_4 98%) which heats up immediately after preparation. Serving as an extremely strong oxidizing agent it removes traces of organic contaminants leaving a high degree of OH surface termination. As SiO_2 is much more stable under acidic than under alkaline conditions no significant roughening of the samples after a single Piranha treatment was detected. Nevertheless, after consecutive removal of SAMs by etching, roughening of the native oxide layer on silicon was found by McIntire et al. [140]. The best results were obtained by irradiating the pre-cleaned silicon wafer substrates with UV light under an atmosphere of pure O_2[24]. The UV light ($\lambda = 172\,\mathrm{nm}$)[25] breaks the covalent bonds of the molecules adsorbed on top of the substrate. Subsequently, the fragments, produced by the UV light, are oxidized by Ozone to CO_2 and H_2O. In the following, the detailed cleaning procedure for the substrates is summarized:

1. Starting from an aqueous soap solution (3 parts water, 3 parts ethanol, 1 part liquid detergent) the cleaning bath was gradually changed (isopropanol, acetone) to more oil like solvents (chloroform). In each solvent the sample was immersed for $15\,\mathrm{min}$ in an ultrasonic bath.

2. Subsequently, the substrates where etched in frechly prepared Piranha for $10\,\mathrm{min}$.

3. After thorough rinsing with pure water, the substrates were completely wetted by water, indicating a high degree of OH surface termination.

4. Prior to further treatment the samples were blown dry in a jet of pure Ar gas.

5.3.2 Preparation of self assembled monolayers (SAM)

The SAMs were prepared from a solution of $1\,\mathrm{mM}$ octadecyl-trichlorosilane (molecular formula $CH_3(CH_2)_{17}SiCl_3$, CAS number 112-04-9)[26]. Even when strictly following the detailed preparation recipe as described below, only about 10% of the samples showed homogeneous, densely packed, and well ordered monolayers. Inhomogeneous samples with strongly tilted SAMs can be clearly identified by a coarse reflectivity measurement (see Sec. 6). As chloroform is harmful, the first part of the preparation was performed under a fume hood.

1. The deposition solution containing approximately $1\,\mathrm{mMl}^{-1}$ OTS was prepared from

[24] The required equipment for UV treatment was not available at the time when the experiments, shown in this work, were performed.

[25] BlueLight Excimer Compact Source, $20\,\mathrm{W}$ electric, irradiance $50\,\mathrm{mWcm}^{-2}$; Heraeus Noblelight, Hanau

[26] Octadecyl-trichlorosilane $\geq$ 90%, product number 104817, Aldrich

- $9\,\mathrm{ml}$ n-hexane (C_6H_{14}), (Riedel-de Haën; 99%, puriss. p.a.)
- $3\,\mathrm{ml}$ chloroform ($CHCl_3$), (Fluka; 99.8%, puriss. p.a.)
- $20\,\mu\mathrm{l}$ OTS.

2. The clean OH-terminated Si-wafer pieces were immersed in the deposition solution for $3\mathrm{h}$. To prevent evaporation of the solvent, the beaker was covered with a Petri dish. This ensures that the samples are completely covered with liquid during the SAM deposition.

3. After removing the samples from the deposition solution, they had to be rinsed to remove OTS residues. Therefore, the samples had to be transferred into the washing beaker quickly without getting dry. They were rinsed twice in $25\,\mathrm{ml}$ n-hexane (C_6H_{14}) and toluene ($C_6H_5CH_3$), respectively.

4. The samples were removed dry from the toluene rinse. Residual droplets sticking to the sample edges were removed in a jet of argon.

5. In order to promote cross linking between the silane anchor groups, the samples were annealed for $1\,\mathrm{h}$ at $110\,^\circ\mathrm{C}$ in a covered beaker.

6. When cooled down to RT, the samples were rinsed with pure water.

5.3.3 Water preparation

Degassed water

There are different standard recipes for the preparation of degassed water. Heating water leads to a decreased solubility of dissolved gases. Thus, boiling the water is the simplest way of reducing the amount of dissolved gasses. The disadvantage is that the hot water may dissolve parts of the container[27] during degassing. An alternative way of degassing water exploits the lower gas solubility in the solid phase compared to the liquid. By cyclic freezing (multiple zone refinement) the gases are gradually removed while the water melts and the trapped air bubbles can escape. Instead of decreasing the gas solubility, also a reduction of the ambient pressure leads to a removal of dissolved gas.

In this work, degassed water was prepared by heavily stirring with a PTFE coated magnetic stir bar (rotation speed $\sim 1000\,\mathrm{rpm}$) under vacuum for 1 h. Agitating the liquid prevents superheating. In addition, the micro-porous PTFE supplies additional nucleation sites where gas bubbles of water vapor, enriched with the dissolved gasses, can form. This method allows the preparation on demand and was implemented in the experimental setup as described in Sec. 5.2.4. As starting material freshly taped ultra pure water from a purification system[28] was used.

[27] The water resistivity of Schott Duran glass decreases strongly for temperatures above $60^\circ\mathrm{C}$. Therefore quartz is the preferable material for experiments involving ultra pure water at elevated temperatures.

[28] Millipore Gradient; $18.2\,\mathrm{M\Omega cm}$; TOC $\leq 5\,\mathrm{ppb}$

parameter	
x-ray wavelength λ	$0.171\,\text{Å}$
wavelength spread $\Delta\lambda/\lambda$	$2.3 \cdot 10^{-3}$
primary beam intensity	$10^{11}\,\text{phot.}\,\text{s}^{-1}$
vertical detector slit opening	$500\,\mu\text{m}$
horizontal detector slit opening	$500\,\mu\text{m}$
vertical beam size b_v	$6.5\,\mu\text{m}$
horizontal beam size b_h	$24\,\mu\text{m}$
vertical beam divergence β_v	$25\,\mu\text{rad}$
horizontal beam divergence β_h	$43\,\mu\text{rad}$
number of Al lenses in the CRL	194
focal distance of the CRL	$6.3\,\text{m}$
distance sample-detector	$1196\,\text{mm}$
maximum vertical momentum transfer q^max	$0.85\,\text{Å}^{-1}$
sample length d	$20\,\text{mm}$

Table 5.1: Summary of the experimental parameters for the reflectivity experiments.

Gas enriched water

Water, enriched with various gases, was prepared from degassed water by bubbling the respective gas through a glass frit[29] through the water until saturation was achieved. In the case of CO_2, the dissolution progress can be monitored by measuring the pH-value of the water.

5.4 Reflectivity experiments

5.4.1 Experimental parameters

The key parameters of the reflectivity experiments are summarized in Tab. 5.1. Complete experimental reflectivity curves were merged from reflectivity scans covering only parts of the total q-range with appropriate absorber settings, horizontal sample translation, and counting time (see Tab. 5.2). Vertical translation was applied to the samples immersed in water to avoid beam damage (see Sec. 6.7). Overlap between neighboring scans allowed identification of misalignment when moving the sample sideways. Background scans were measured for each reflectivity scan with identical parameters by detuning the incident angle α_i by $+0.05\,°$.

[29] Porosity 1 (pore size for gas distribution in liquids), nominal maximal pore size $100 - 160\,\mu\text{m}$, bowel $\varnothing\,25\,\text{mm}$, area $3.5\,\text{cm}^2$; Schott Duran

$\alpha^{\min}$ [°]	$\alpha^{\max}$ [°]	step size [°]	absorber factor	counting time [s]	translation $[\mu\mathrm{m\,point^{-1}}]$
dry samples					
0.00	0.14	1/600	30000	3	-
0.09	0.24	1/300	400	3	-
0.16	0.60	1/200	30	3	-
0.30	0.80	1/100	1	3	-
0.75	1.00	1/100	1	10	-
0.90	1.40*	1/50	1	30	-
samples immersed under water					
0.00	0.14	1/600	30000	3	-
0.09	0.24	1/300	70	3	-
0.16	0.60	1/200	5	3	2
0.30	0.80	1/100	1	3	17
0.75	1.00	1/100	1	10	24
0.90	1.40*	1/50	1	30	24

Table 5.2: Summary of the reflectivity scans for the dry sample and the sample immersed in water. In the high-angle regime of the marked (*) scans, data were dismissed from analysis when the signal to background ratio was too low.

5.4.2 Data preprocessing

Footprint correction

At shallow angles, the height of the incoming x-ray beam is larger than the vertical projection of the tilted substrate. Thus, the incident beam hits the sample only partially. This has to be corrected by applying an appropriate foot print correction to the raw data. Measurements show that the vertical beam profile can be approximated fairly well by a Gaussian intensity distribution (see Fig. 5.3b). For a Gaussian beam profile the foot print corrections are given by

$$f_{\mathrm{fp}} = \mathrm{erf}\left(\frac{d\sin\vartheta}{8\sqrt{\ln 2}b_{\mathrm{v}}}\right) . \tag{5.4}$$

For more details see references [12] and [104].

Data normalization

Prior to further data analysis, the count rates measured with the scintillation counter were corrected for the detector dead time as described in Sec. 5.1.4. Between refills of the storage ring, the loss of electrons leads to a monotonous decrease in the intensity of the primary beam. By monitoring the primary beam with PIN diode D1 the data can be corrected

not only for the ring current, but also for other effects[30] leading to intensity fluctuations in the incident beam. Finally, the measured data was multiplied with the foot print and absorber corrections (see section 5.1.5) and merged together to one single data set.

[30] Temperature changes in the beamline optics can detune the alignment.

Chapter 6

Data analysis, results, and discussion

6.1 Overview of the x-ray experiments

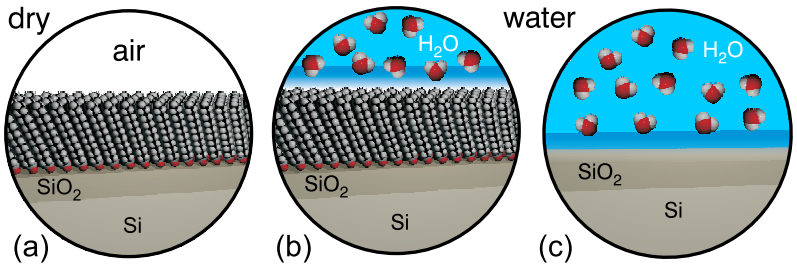

Figure 6.1: Sketch of the interfaces employed in this study. (a) The free OTS-air interface (Si-SiO_2-OTS-air); (b) The deeply buried hydrophobic OTS-water interface (Si-SiO_2-OTS-water); (c) The deeply buried hydrophilic silicon dioxide-water interface (Si-SiO_2-water).

Figure 6.1 summarizes the schematic molecular architecture of the different samples used in this study[1]. The x-ray reflectivity curves corresponding to the systems studied, are displayed in Fig. 6.2. Since a detailed knowledge of the structural arrangement of the self-assembled OTS-layer on the substrate is crucial for the following high precision analysis, the x-ray reflectivity from the Si-SiO_2-OTS interface (see Fig. 6.2a) will be discussed separately in Sec. 6.2. The main result of this study, the x-ray reflectivity from the Si-SiO_2-OTS-H_2O interface, is shown in Fig. 6.2c. In Sec. 6.3 the analysis of the water-OTS interface is discussed by using both, a semi-quantitative analysis employing the analytical gap-step model introduced in Sec. 4.3.2, as well as the refinement of a slab model.

[1] The Si-SiO_2-air system can not be measured with the setup employed in this work. A thin water layer, adsorbed on top of the strongly hydrophilic OH-terminated native SiO_2, leads to strong oscillations in the reflection pattern [141]. This prevents a precise determination of the oxide thickness and density impossible. For those experiments the sample had to be heated and kept under UHV conditions in order to remove any adsorbed water.

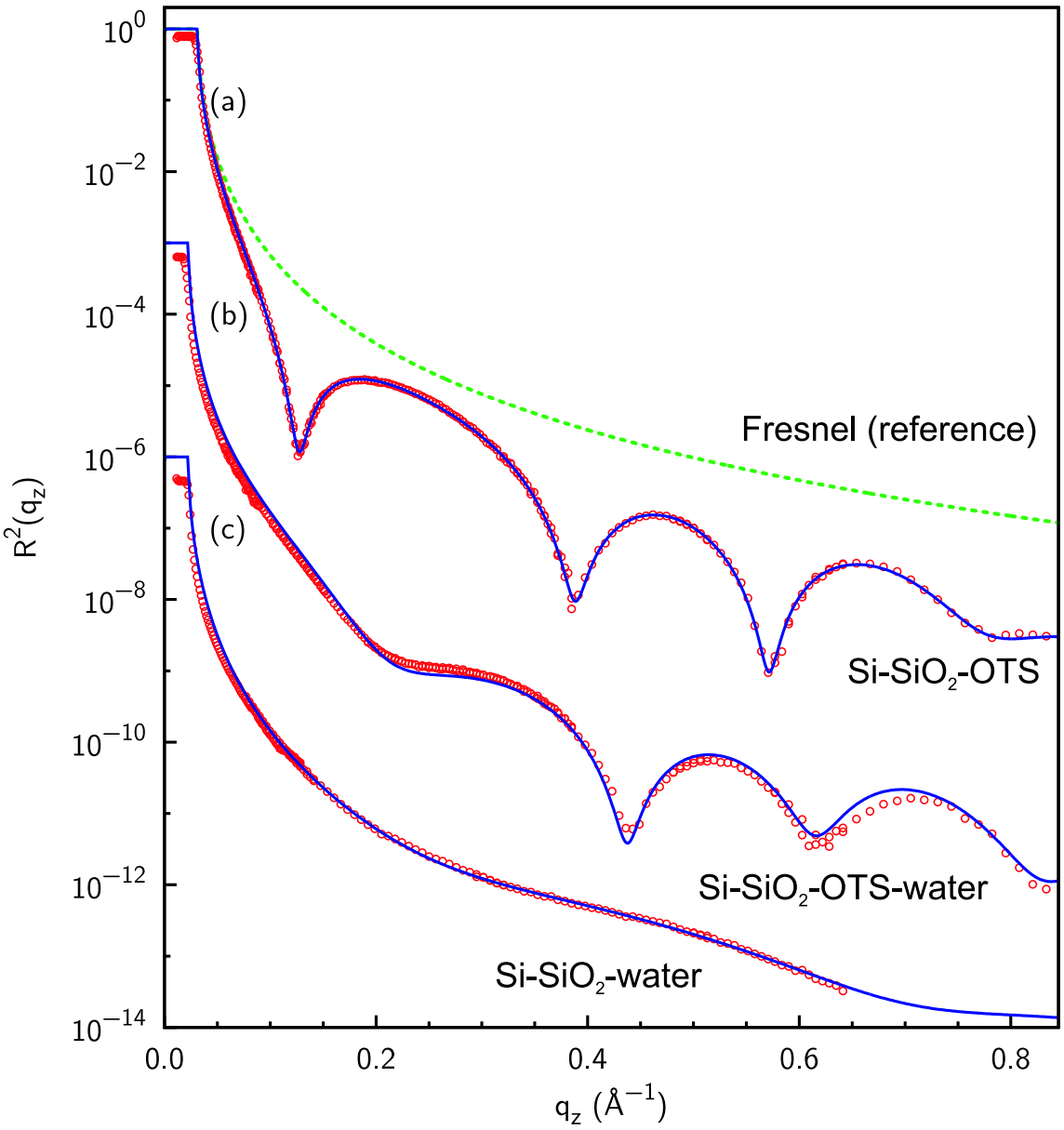

Figure 6.2: Comparison of the experimentally recorded x-ray reflectivity patterns (circles) from the different samples introduced in Fig. 6.1. The measurements are shifted by three orders of magnitude for clarity. For comparison, the Fresnel reflectivity from an ideal silicon substrate is shown for the dry OTS-covered substrate (dashed green line). The x-ray reflectivities from all interfaces are perfectly reproduced by refinement of a slab model (blue lines, for details see Sec. 4.2.5). (a) Dry silicon wafer covered with a self-assembled OTS-layer. (b) Silicon wafer covered with a native SiO_2-layer and immersed in degassed water. (c) Native silicon wafer covered with a self assembled OTS-layer immersed in degassed water.

Subsequently, the effect of dissolved gas on the interfacial water structure is discussed in Sec. 6.5. Additional measurements of the x-ray reflectivity from the Si-SiO_2-H_2O interface, which are shown in Fig. 6.2b, are discussed in Sec. 6.4. Summarizing this results, in Sec. 6.6 the extracted interfacial profiles from the experiments with the samples immersed in water are discussed from a more general point of view by comparison with a simple DFT model, introduced in Sec. 3.3.2. Finally, Sec. 6.7 deals with the radiation damage and the associated chemical processes caused by the x-ray beam during the reflectivity measurements.

6.2 The dry OTS-layer

6.2.1 Qualitative analysis

Figure 6.2c shows the x-ray reflectivity $R^2(q_z)$ from the dry OTS-layer grown on SiO_2. At small vertical momentum transfer, total reflection occurs up to $q_\mathrm{c} = 0.03\,\text{Å}^{-1}$ which is determined by the electron density difference between air and silicon. This plateau is followed by a rapid decay of the reflected intensity for $q_\mathrm{z} > q_\mathrm{c}$ commonly known as the Fresnel reflectivity curve (green line). Finally, at large momentum transfer values the oscillations (Kissig fringes) in the reflectivity curve originate from the finite thickness of the OTS-layer.

Figure 6.3 shows the x-ray reflectivity $R^2(q_\mathrm{z})$ normalized by the rapidly decaying Fresnel reflectivity $R_\mathrm{F}^2 \propto q^{-4}$. The normalized reflectivity exhibits minima at $q_\mathrm{z} = 0.127\,\text{Å}^{-1}, 0.387\,\text{Å}^{-1}, 0.572\,\text{Å}^{-1}, 0.780\,\text{Å}^{-1}$ indicated by vertical solid lines. Since a single homogeneous layer on top of a substrate produces a series of equally spaced interference fringes in x-ray reflectivity [10], it is immediately apparent that the OTS-layer which is anchored on top of the native SiO_2-layer exhibits a more complex substructure. The OTS-SAM can be divided into an anchor (head) group, supplying a covalent bond of the organic molecule to the SiO_2, and an 18 C long linear hydrocarbon chain (tail), which is responsible for the hydrophobic properties of the OTS-SAM. Therefore, a realistic model of the electron density across the interface requires at least three layers. Nevertheless, the OTS-layer thickness can be estimated (neglecting the SiO_2 layer due to $\rho_{\mathrm{SiO_2}} \approx \rho_{\mathrm{Si}}$) from the position $q_\mathrm{z}^{(1)}$ of the first minimum to $d_\mathrm{OTS} \approx \pi \left({q_z^{(1)}}^2 - q_\mathrm{c}^2 \right)^{-1/2} = 27\,\text{Å}$. Features in the x-ray reflectivity curve at small values of q_z correspond to the large scale structure in real space. Thus, the first minimum is almost insensitive to details in the substructure of the OTS molecule and provides a good estimate for the overall thickness of the molecular layer.

The quality of a given OTS-SAM can be determined from the reflection pattern by mainly three relevant features: The roughness σ of the sample is given by the overall decay of the reflected intensity. In the simple case of one interface, this is taken into account by a damping factor $e^{-\sigma^2 q^2}$. For comparison, in Fig. 6.3 we show a calculated reference signal (dashed line) that assumes scattering from two independent rough interfaces (SiO_2-OTS

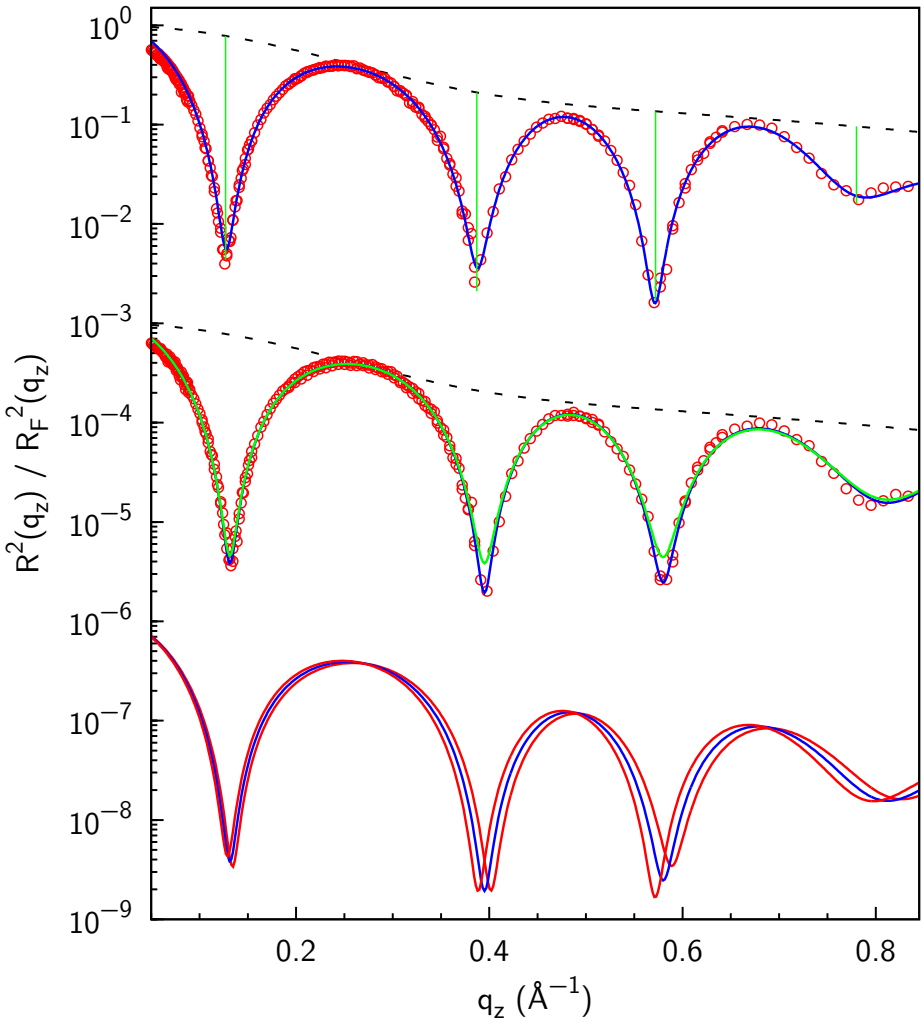

Figure 6.3: Normalized X-ray reflectivity of the homogeneous OTS SAM grown on a native SiO_2 layer on top of a silicon wafer substrate (circles) before measuring the sample immersed in water (top curve) and after removing the the water at the end of the experiment (middle curve). The solid blue line denotes a fit employing a two layer model for the OTS SAM (head and tail group of the OTS molecule). The depth of the minima is measured with respect to a calculated reference signal (dashed line) assuming independent scattering from the rough SiO_2-OTS ($\sigma = 1.1$ Å) and OTS-air ($\sigma = 4.4$ Å) interface. The bottom curves show the calculated patterns using the extracted parameters (blue line) together with a profile where the OTS head group is stretched by $\pm 2.35\%$ (red lines). An incoherent sum of corresponding profiles with a Gaussian FWHM of the stretch parameter of 2% results in a pattern depicted as the green line in the middle panel.

and OTS-air), which supplies an approximate measure for the layer roughness. Since the measured overall damping of the normalized reflectivity curve is only one order of magnitude up to $q_{\max} = 0.8\,\text{Å}^{-1}$, the roughness between the layers with the largest density change can be readily estimated to approximately 2-3Å.

The intensity ratio between a minimum and the neighboring maxima of the homogeneous OTS SAM, shown in Fig. 6.3, is larger than two orders of magnitude (vertical lines). This ratio is very sensitive to inhomogeneities in the organic layer induced by e.g. island formation. Comparison of the experimentally obtained pattern with an incoherent sum of calculated values assuming a Gaussian distribution of the film thickness with a FWHM of 2% constrains the abundance of surface inhomogeneities. This again confirms the presence of a very homogeneous layer.

The spacing between the interference minima is related to the thickness of the layer. While densely packed OTS molecules, which are standing almost upright, result in a thick SAM (first minimum at $q_z^{(1)} = 0.13\,\text{Å}^{-1}$), strongly tilted or even laying-down molecules produce a thin layer and therefore a first minimum shifted to higher values of q_z.

In addition, the surface quality was checked by rocking scans. Scans through the specular rod revealed a resolution limited full-width-half-maximum (FWHM) of $2.5 \cdot 10^{-3}\,^{\circ}$ for all samples (the FWHMs extracted from measurements on the dry sample are shown in Fig. 6.9b as triangles). This again confirmed the high structural quality of the samples used in this study.

6.2.2 Parameter refinement of a slab model

From the reflection pattern of the dry OTS-SAM shown in Fig. 6.3 the laterally averaged electron density profile across the interface can be deduced quantitatively by parameter refinement of a slab model. For the actual fitting, the experimental data in the range of $0.06\,\text{Å}^{-1} < q_z < 0.82\,\text{Å}^{-1}$ was used. By applying one slab for the SiO_2 layer on the Si substrate and two slabs for the head and the tail group of the OTS, respectively, the measured reflectivity curve is reproduced perfectly (solid line in Fig. 6.2 and Fig. 6.3). The final parameters are summarized in Tab. 6.1 and are in very good agreement with the work of Tidswell et al. [65, 142, 143].

The values extracted from the reflectivity data recorded in the beginning and at the end of the experiments on an irradiated spot agree very well with each other. These values were used to estimate a typical error of about 5% for each quantity. Due to a refractive index close to the silicon substrate, only the thickness of the native oxide layer shows larger variations (see also Sec. 6.4).

As expected, the value for the density of the hydrocarbon chain lies in between the one for liquid n-octadecane ($\rho = 0.78\,\text{gcm}^{-3}$) and the one for single crystalline n-octane ($\rho = 0.93\,\text{gcm}^{-3}$ [68]) or high density polyethylene PE-HD ($\rho = 0.94 - 0.97\,\text{gcm}^{-3}$). This is explained by the more densely packed hydrocarbon chains of the anchored silane on the native SiO_2 substrate in comparison to the corresponding disordered liquid phase.

Even small holes inside the SAM would result in a significantly lower (averaged) den-

layer	d [Å]	σ [Å]	ρ [g cm^{-3}]	$\rho_e r_e$ [10^{15} m^{-2}]	δ [10^{-8}]	β [10^{-12}]
air	-	2.6	0.00	0.00	0.00	0.00
	-	2.6	0.00	0.00	0.00	0.00
OTS tail	20.9	2.7	0.86	0.84	3.91	2.88
	21.8	2.9	0.85	0.83	3.86	2.85
OTS head	5.8	0.0	1.68	1.43	6.63	8.33
	5.7	0.0	1.72	1.45	6.76	8.50
SiO_2	11.3	0.0	2.12	1.85	8.62	10.84
	10.4	0.0	2.18	1.85	8.58	10.79
Si (bulk)	-	-	2.32	1.96	9.12	21.46

Table 6.1: Model parameters for the OTS sample in air. The values given in the upper rows correspond to the reflectivity data recorded before the sample was immersed in water. Values in the lower rows were extracted from the dry sample after the measurements at the sample immersed in water. The density for the bulk Si substrates was taken from literature [110].

sity ρ_t for the hydrocarbon chain. The length of a stretched linear alkyl chain C_nH_{2n+1} in all-trans configuration can be estimated from bond angles and interatomic distances taken from literature [144]. The projected C–C bond length of 1.27 Å is deduced from an interatomic distance of $d_{C\text{–}C} = 1.53$ Å and a bond angle of $112.9°$. The terminal methyl group (CH_3) adds 1.5 Å. This results in a maximum length of 23 Å for the OTS alkyl chain ($n = 18$). The comparison to the value of $d_t = 21.8$ Å, extracted from the x-ray reflectivity data suggests a tilt angle of the hydrocarbon chain of about $20°$. This can be readily explained by the larger diameter of the silane anchor group in comparison with the diameter of the hydrocarbon chain. The VdW interaction between the alkyl chains favors therefore a tilt resulting in a closer packing of the OTS tails. With the known molecular mass of $A_r = 253.5\,\mathrm{g\,mol^{-1}}$ for the OTS alkyl chain, the mass density converts into a molecular volume of 490 Å^3 for an alkyl chain or an effective area of 23 Å^2 per OTS molecule. The density profile obtained from the parameter refinement is supported by the qualitative analysis discussed in Sec. 6.2.1, confirming the high quality of the prepared OTS-SAMs.

6.3 The hydrophobic water-OTS interface

6.3.1 Models without an interfacial water gap

The model for the electron density profile used for the slab calculations has been constrained by taking into account mass conservation for the alkyl chain, i.e. the product $d\rho$

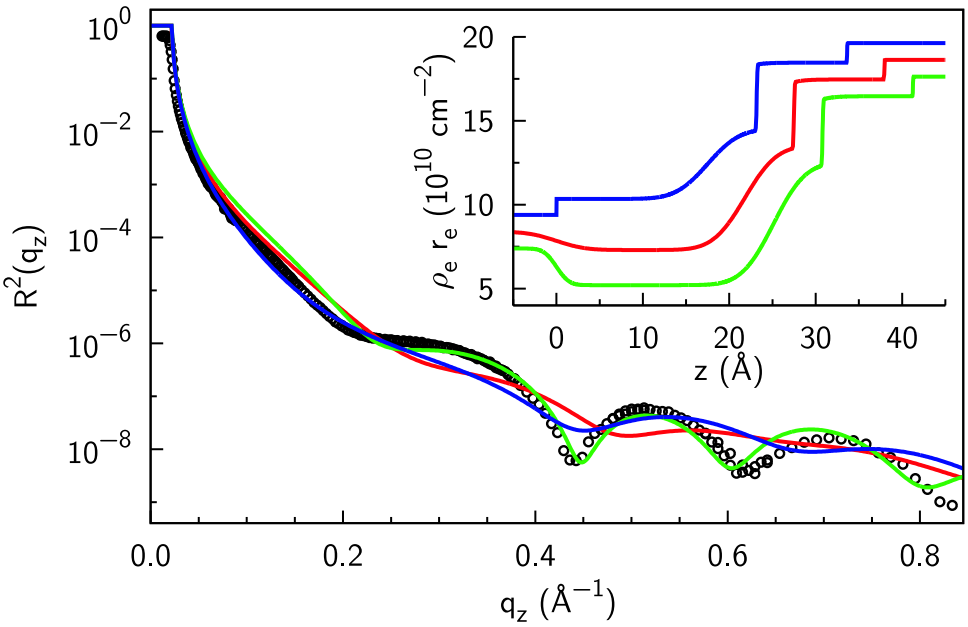

Figure 6.4: X-ray reflection pattern from the OTS-layer immersed in degassed water (circles). Models without an interfacial gap: without modifications to the hydrophobic layer (red line) and by stretching (green line) and compressing (blue line) the alkyl chains while keeping the product $d\rho$ constant (mass conservation). The inset shows the associated electron density profiles. The curves are shifted vertically for clarity.

was kept constant at $6.4\,\mathrm{e\AA}^{-2}$ as determined from the measurement at the dry OTS layer. The interfacial roughness σ between the water and the alkyl chains was kept as a free parameter and refined in the analysis.

In order to rule out that the observed oscillations are originating from a densification or stretching of the OTS hydrocarbon chain only, both cases are discussed separately. As the packing of the hydrocarbon chains leads to a density of about 90 % compared to the crystalline modification (see Tab. 6.1), further densification is rather limited, in order to maintain a physically meaningful model. In order to shift the first minimum from $q_z = 0.27\,\mathrm{\AA}^{-1}$ (see red curve in Fig. 6.4) to $q_z = 0.205\,\mathrm{\AA}^{-1}$ a compression of about 60 % is required (blue curve), which is incompatible with the boundary conditions.

Figure 6.4a shows that the main features of the measurements could also be reproduced with an increased thickness of $25\,\mathrm{\AA}$ for the hydrophobic alkyl chain (green curve). The observed shift in the position of the first minimum to smaller values can, in this case, be achieved by stretching the alkyl chain, since the simple argument $d \approx \pi/q_{\mathrm{min}}$ does not hold anymore. Due to mass conservation in the alkyl chain layer the electron density is then significantly lower than in bulk water and therefore the profile does not decay monotonously from the silicon to the water. Since the maximum length of the hydrocarbon chain of $23\,\mathrm{\AA}$ cannot be exceeded, a simple stretching of the hydrophobic alkyl chain

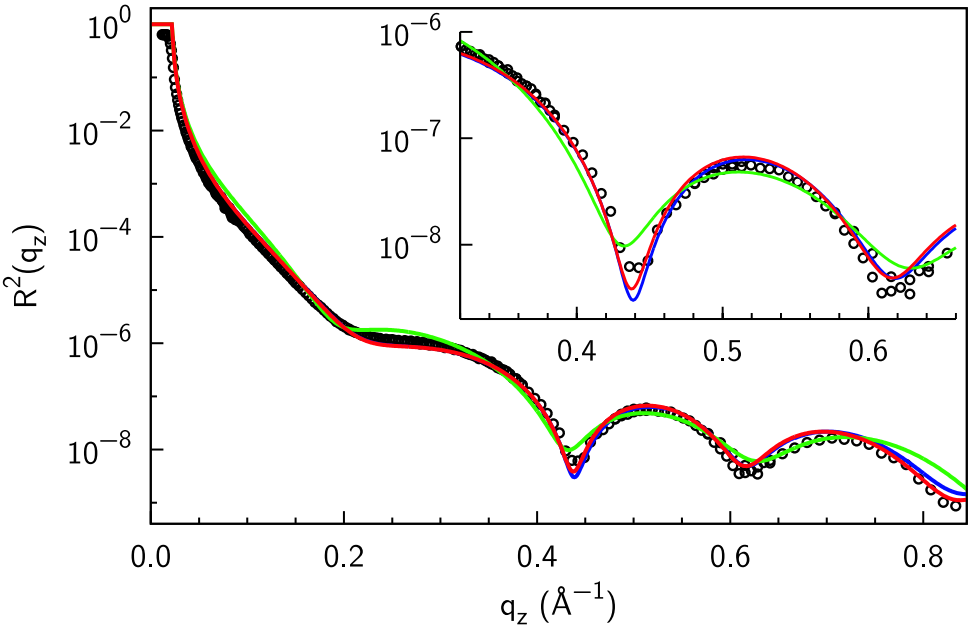

Figure 6.5: The x-ray reflectivity from the hydrophobic OTS-layer immersed in degassed water (circles) is reproduced by a four layer model, including the OTS-layer (head and tail group of the OTS molecule) on SiO_2 and an interfacial depletion layer between the OTS-layer and the bulk water. The solid lines give the best fits for a fixed thickness d_w of the interfacial gap. (blue: 2.0 Å, red: 3.8 Å, green: 8.0 Å).

cannot explain the observed features in the reflectivity curve.

6.3.2 Models with an interfacial water gap

In the following analysis, all parameters that have already been determined at the dry samples were kept fixed. Only a densification of the OTS tail group (hydrocarbon chain), and an additional density depletion layer of thickness d_w in between the hydrophobic alkyl chains and the bulk water phase was allowed. The product of density and thickness $d_t\rho_t$, however, was kept constant. In contrast to the models without an interfacial depletion layer, the obtained densification of 7% is physically feasible.

Figure 6.5b shows a representative selection of calculated reflection patterns with fixed thickness d_w of the interfacial gap ranging from $d_w = 2.0$ Å to $d_w = 8.0$ Å. Both parameter sets, with $d_w = 3.8$ Å, $\rho_w/\rho_{H_2O} = 0.71$ (red line) and $d_w = 2.0$ Å, $\rho_w/\rho_{H_2O} = 0.44$, (blue line) result in a reflection patterns which reproduce the experimental data excellently. Only for larger gap widths ($d_w = 8.0$ Å, green line) significant deviations appear. Apparently, the thickness of the depletion layer itself is not a parameter, which can be extracted from the experimentally obtained reflection pattern directly within the slab model.

For a quantitative determination of the interfacial gap size, and in order to identify

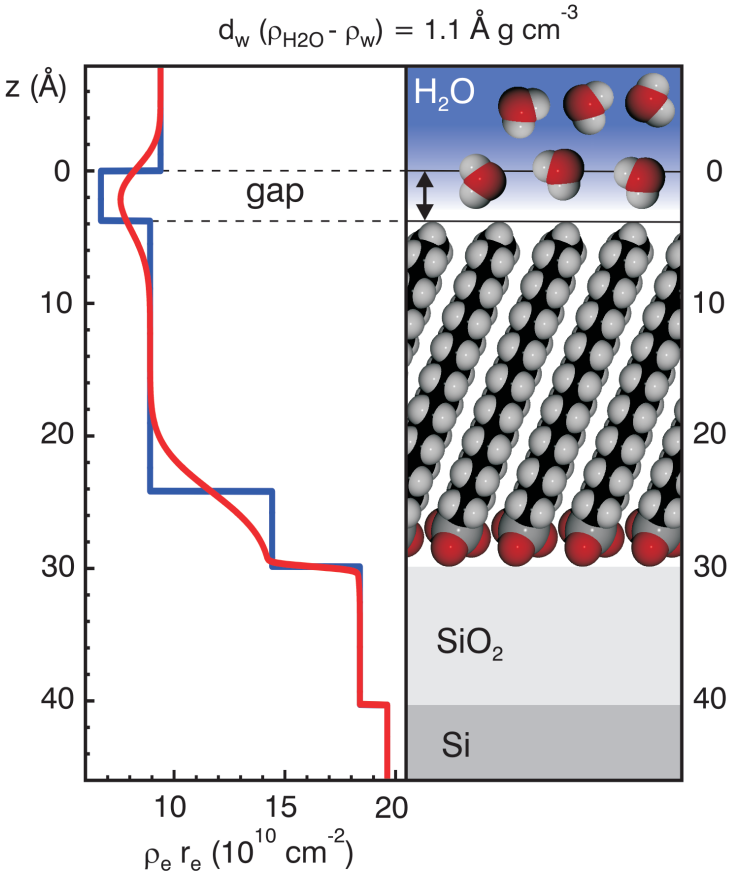

Figure 6.6: Electron density profile (OTS-sample immersed in water) deduced from the parameter refinement of a four-layer model to the measured x-ray reflectivity pattern (blue line: box model for the electron density; red line: density profile including the roughness of the layers). On the right side a sketch of the profile including the native SiO_2 oxide, a layer of self assembled OTS molecules (head and tail group of the OTS molecule), and a depletion layer between the OTS-layer and the bulk water is shown.

coupling between fit parameters, extensive fitting of the data was performed. Figure 6.7 shows that for a gap thickness of $1\,\text{Å} < d_\text{w} < 6\,\text{Å}$ all fits were comparable in quality indicated by the almost constant logarithmic deviation $\chi^2 \propto \min_\alpha \sum_i \left(\ln \alpha I_{i,\text{exp}} - \ln I_{i,\text{cal}}\right)^2$ between the experimentally observed reflectivity pattern (I_exp) and the calculated values (I_cal). For details see Sec. 4.3.1.

While it is not possible to determine the gap width d_w better than $1\,\text{Å}$ - $6\,\text{Å}$, the integrated density deficit $d_\text{w}\left(\rho_{\text{H}_2\text{O}} - \rho_\text{w}\right) = 1.1 \pm 0.1\,\text{Å}\,\text{g}\,\text{cm}^{-3}$ stays constant over this range. This water depletion layer corresponds to an interfacial electron deficit of $\Gamma = 0.3\,e\text{Å}^{-2}$. The strong oscillations observed in the reflection pattern originate from the interference between the wave reflected from the integrated density deficit of the interfacial structure and the wave reflected at the SiO_2 substrate. On the other hand, without an additional structure (depletion gap or compression peak) in between the alkyl chains and the bulk water, no oscillatory pattern would appear in x-ray reflectivity due to close contrast matching. The wide range of d_w-values which is compatible with the experimental data is determined by several factors. The q-range covered by the experiment leads to a real space resolution on the order of $\pi q_\text{max}^{-1} = 4\,\text{Å}$. The given interfacial roughness of the OTS-layer of $\sigma_\text{OTS} = 2.6\,\text{Å}$ smears the profile additionally (for a discussion of the sensitivity of x-ray reflectivity measurements to the shape of the depletion gap, see Sec. 4.3.3).

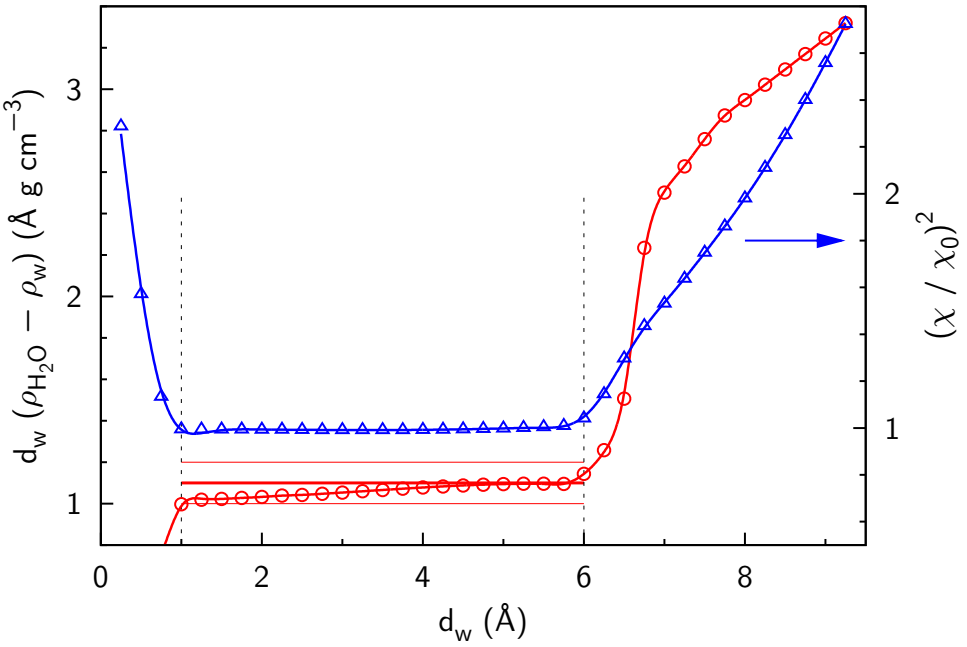

Figure 6.7: Integrated density deficit (circles, left axis) $d_\mathrm{w}\,(\rho_{\mathrm{H_2O}} - \rho_\mathrm{w})$ as a function of the gap width d_w. The blue triangles give the goodness $(\chi/\chi_0)^2$ of each fit (right axis).

Parameter sets with significantly larger values of d_w (i.e. $d_\mathrm{w} > 6\,\text{Å}$) rapidly decrease the goodness of the fit. For a thickness of the interfacial gap d_w smaller than $1.1\,\text{Å}$ an integrated density deficit of $d_\mathrm{w}\,(\rho_{\mathrm{H_2O}} - \rho_\mathrm{w}) = 1.1\,\text{Å g cm}^{-3}$ can only be achieved with a gap layer density $\rho_\mathrm{w} < 0$, which is unphysical.

6.3.3 Models with nanobubble formation

The existence of a hydrophobic gap has sometimes been linked to the formation of gas nanobubbles at the hydrophobic interface. In this scenario, the water density at the interface exhibits a strong lateral variation. Lateral structures with a typical extension L at the solid-liquid interface give rise to an off-specular diffuse intensity distribution on the length scale of $q_x = \frac{2\pi}{L}$ around the specular reflected beam (see Fig. 6.8). The presence of such off-specular scattering has been carefully checked for.

Figure 6.9 shows rocking scans for selected values of the vertical momentum transfer q_z. The data for measurements performed in degassed and gas enriched water coincide perfectly. In Fig. 6.9b, the extracted FWHM at different sample positions is plotted versus the vertical momentum transfer. The q-space resolution is given by the vertical divergence of the x-ray beam $\beta_\mathrm{v} = 25\,\mu\mathrm{rad}$ and the vertical detector slit opening of $10\,\mu\mathrm{m}$ used for the rocking scans. This results in an instrumental resolution of $\delta q_x \approx 6 \cdot 10^{-5} q_z$ in the horizontal direction (see Sec. 4.1.3). A further source of broadening is the curvature of

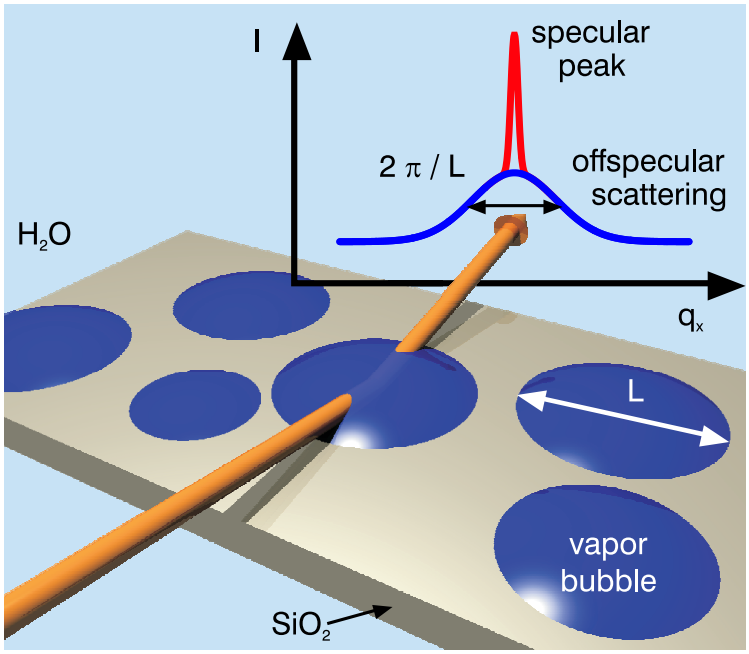

Figure 6.8: Sketch of the scattering in forward direction from an interface covered by randomly spaced bubbles.

the sample surface under the large footprint of the x-ray beam at the small incident angles $\alpha_{\rm i} \approx 1.4 \cdot 10^{-2} q_z$ Å$\cdot$rad resulting in a total experimental resolution of $7.2 \cdot 10^{-5} q_z$ (straight line in Fig. 6.9b).

In all the x-ray reflectivity measurements presented in this work, no off-specular scattering from lateral structures at the solid-liquid interface was detected. Bubbles with a height larger than the upper limit for the interfacial gap ($d_{\rm w} = 6$ Å) would immediately show up as additional roughness, leading to a strong damping in the reflected intensity. On the other hand, bubbles with a height smaller than the upper limit for the interfacial gap require a surface coverage of at least 20% to produce an integrated density deficit of 1.1 Å g cm^{-3}. Such a large coverage would produce strong diffuse scattering. Taking into account the experimental resolution, this implies that there are no lateral inhomogeneities on length scales $L < 60\,\mu$m.

For gas bubbles with a lateral size larger than the coherence length of the x-ray beam, the measured x-ray reflectivity is an incoherent sum of reflected intensities from regions where the water is directly in contact with the OTS and the bubble region [90]. This would imply a smearing of the interference pattern in the x-ray reflectivity, which is not observed experimentally. In addition, the thickness $d_{\rm w}$ of the density depletion layer at the hydrophobic interface is at most a few diameters of a water molecule, leading to completely unphysical contact angles for such large gas bubbles.

The results obtained in this work therefore provide strong evidence that the density depletion at the water-OTS interface is not caused by the formation of gas bubbles at the interface. AFM measurements reported nanobubbles with base areas of approximately $0.1\,\mu$m^2, and a height of several nm [18]. For more details on the formation of nanobubbles

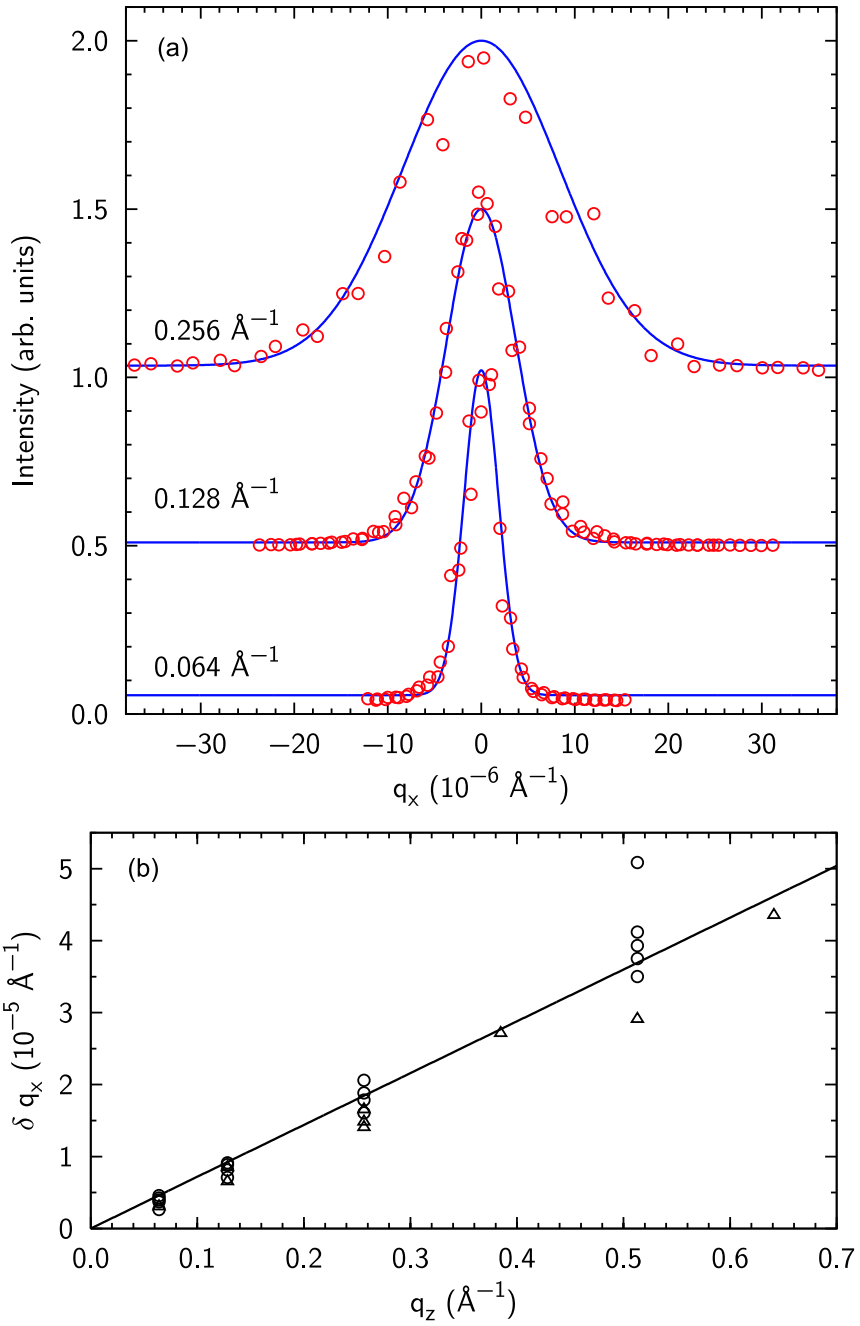

Figure 6.9: (a) Rocking scans (scanning along q_x while keeping q_z constant) of the sample immersed in water for different values of q_z. The experimental data (circles) were compiled from several measurements on different spots, for degassed and gas enriched water. Solid lines denote Gaussian profiles. (b) Extracted FWHM δq_x versus the vertical momentum transfer q_z for the dry OTS-sample (triangles) and the sample immersed in water (circles). The straight line indicates an experimental resolution of $\delta q_x = 7.2 \cdot 10^{-5} q_z$.

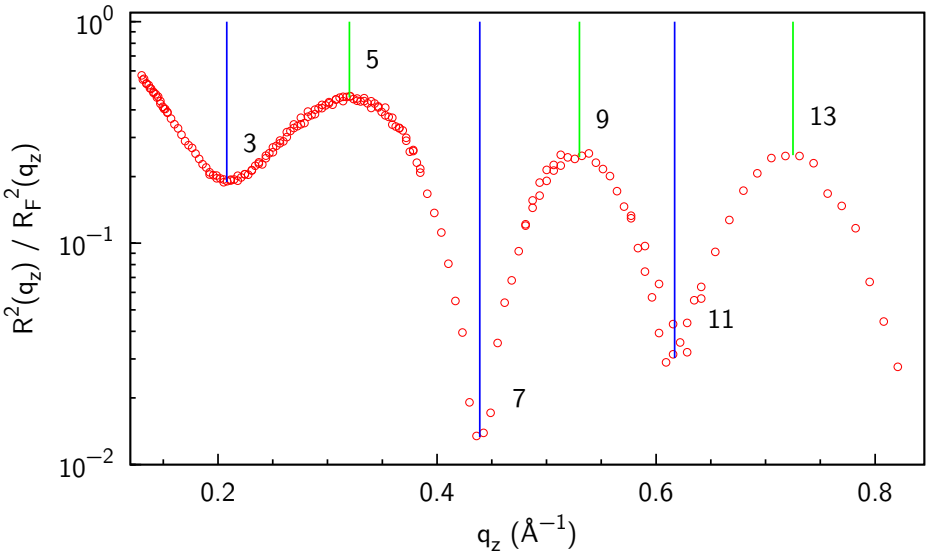

Figure 6.10: Normalized reflectivity of the OTS-layer immersed in degassed water (red circles). Vertical lines indicate the momentum transfer for constructive (green lines) and destructive (blue lines) interference.

in AFM experiments see Sec. 3.4.2. According to a recent quartz crystall microbalance (QCM) study, nanobubbles do not form on ultra smooth homogeneous surfaces [145]. (Note that the microscopic roughness of the hydrophobic samples prepared in this work is below 3 Å; see Table 6.1) Confinement effects were found in infrared spectroscopy studies (ATR-FTIR) on the interaction between small hydrophobic particles [99] as well as in experiments on their colloidal stability in electrolytes [98]. Therefore, it is concluded that the nanobubbles reported in some scanning probe experiments are created by confinement effects, i.e. capillary evaporation between the hydrophobic substrate and the AFM tip.

6.3.4 Analysis via the gap-step model

Figure 6.10 shows the normalized reflectivity curve R^2/R_{F}^2 for the OTS-layer immersed in degassed water. A semi-quantitative analysis of the reflection pattern can be performed using the analytical solution of a gap-step model as described in Sec. 4.3.2. The structure factor follows the generic shape of the gap-step model including a density depletion on top of a thin, almost contrast matched layer (electron density ratio $\rho_{\mathrm{tail}}/\rho_{\mathrm{H_2O}} = 0.92$) as shown in Fig. 4.5. Strong minima at $q_z = 0.208\,\text{Å}, 0.439\,\text{Å}, 0.617\,\text{Å}$, indicated by the vertical blue lines, are assigned to the dimensionless momentum transfer values $q_z' = 3/4,\ 7/4,\ 11/4$ ($\Delta' = 3, 7, 11$) expected from the gap-step model (see Eq. (4.24)). The normalized reflectivity is characterized by an initial increase of the oscillation strength of equally spaced interference fringes, followed by a decrease for higher values of q_z. Deviations from the model reflectivity calculated from Eq. 4.24, such as the not perfectly

equal spaced minima, are, amongst others, explained by the additional silane anchor group, the native SiO_2, the slight contrast mismatch of 8 % between water and the OTS tail, or the substrate roughness. The averaged period of the interference fringes of $\Delta q_z \approx 0.2\,\text{Å}^{-1}$ corresponds to a layer thickness of $d = 2\pi\Delta q_z^{-1} \approx 31\,\text{Å}$. This length can be directly assigned to the overall thickness $d = d_{\text{head}} + d_{\text{tail}} + 1/2\,d_{\text{gap}} = 26\,\text{Å} + 1/2 d_{\text{gap}}$ of the hydrophobic OTS-layer (see Tab. 6.1). The largest oscillation amplitude appears at the third minimum at $q_z^{(3)} = 0.438\,\text{Å}^{-1}$. This corresponds to the dimensionless parameters $q' = 7/4$ and $\Delta' = 7$ (see Eq. (4.24)). Therefore, the width (FWHM) of the gap can be directly estimated to $\Delta_{\text{gap}} = 4\sqrt{2\ln 2}d/(\pi\Delta') = 6.6\,\text{Å}$ within the gap-step model. This value represents approximately the upper limit of the gap width obtained from the parameter refinement shown in Sec. 6.3.2.

6.4 The water-SiO_2 interface.

The details of the structure of water at real interfaces should depend on many parameters, such as the chemical composition of the substrate surface. As shown in Sec. 3.3.2, in a hard sphere model a decrease in the integrated density depletion for substrate-fluid combinations with smaller contact angles is predicted. In order to test the effects of these parameters, additional x-ray reflectivity measurements at the hydrophilic OH-terminated water-SiO_2 interface have been performed. Figure 6.2b shows that the x-ray reflectivity can be modeled perfectly with a single (native) SiO_2 layer (thickness $13.6\,\text{Å}$, $\rho = 2.2\,\text{gcm}^{-3}$, $\sigma = 1.0\,\text{Å}$). These values correspond very well to the parameters extracted from the reflection pattern of the dry OTS-sample summarized in Tab. 6.1 confirming the appropriateness and consistence of the analysis. Adding a layer of increased or decreased density at the interface does not improve the fit significantly. Due to the large step in the electron density at the water-SiO_2 interface and the missing contrast matched reference layer, it is not possible to extract details on the interfacial water density profile.

6.5 Influence of gases dissolved in the water

One could intuitively assume that any dissolved gas within the water phase might segregate to the hydrophobic interface, thereby further increasing the gap size and reducing interface energy costs. Therefore, the influence of dissolved gases on the interfacial density depletion was investigated. For this, the hydrophobic OTS-substrate was immersed in water which was saturated with a variety of gases as described in Sec. 5.3.3 (inert noble (Ar, Xe, Kr), linear non polar (N_2, O_2, CO_2), polar gas (CO)), and a 0.5 M aqueous HCl solution. Selected reflectivity curves for different gases are shown in Fig. 6.12. It is evident that all the curves are virtually identical up to the maximum momentum transfer accessible in the experiment. Therefore, it is concluded that – within the real space resolution of $4\,\text{Å}$ and the convolution due to the intrinsic roughness of the hydrophobic interface – from x-ray reflectivity measurements there is no evidence for an effect of dissolved gases

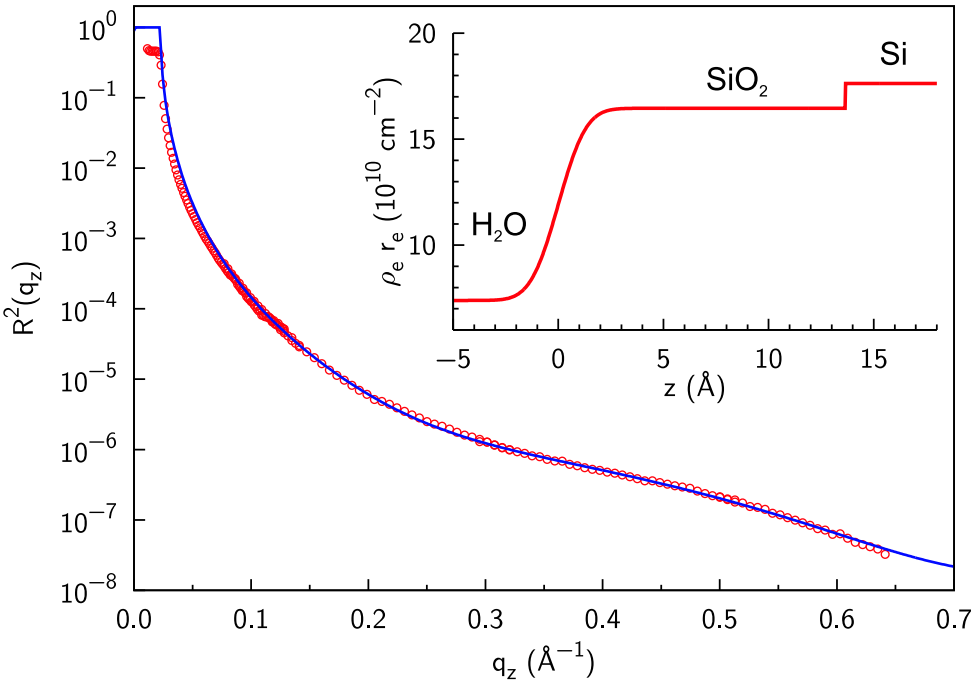

Figure 6.11: Reflection pattern from the Si-SiO_2-water interface. The experimental data (circles) are reproduced perfectly by the calculated reflection pattern (solid line) from a two layer model (inset).

on the size of the interfacial gap. In contrast to these experiments performed at a single flat interface, experiments in confinement geometry are sensitive to gases dissolved in the water (e.g. CO_2). Here capillary evaporation is the dominant effect as the liquid phase is constrained in between two objects spaced by approximately $10\,\mathrm{nm}$ [15, 98]. Also in molecular dynamic simulations [17] no effect of dissolved gas was found at a single flat and hydrophobic wall, whereas in confinement a significantly higher gas concentration close to the hydrophobic interfaces was found.

6.6 Discussion of the interfacial density depletion

In the measurements, a characteric depletion gap was only found at the water-OTS interface, while the result on the water-SiO_2 interface is less conclusive. The analysis limits the size of the gap to $d_\mathrm{w} = 1 - 6\,\text{Å}$, a length scale which is close to the diameter of the water molecule ($2.8\,\text{Å}$). Thus, the perturbation of the water structure by the presence of the hydrophobic interface is confined to a length scale which is comparable to the correlation length $\xi = 4\,\text{Å}$ [59] and the average OO distance $d_\mathrm{OO} = 2.9\,\text{Å}$ [23, 24] of bulk water (see Sec. 3.1).

This rises the question whether this small gap is a special feature associated with hy-

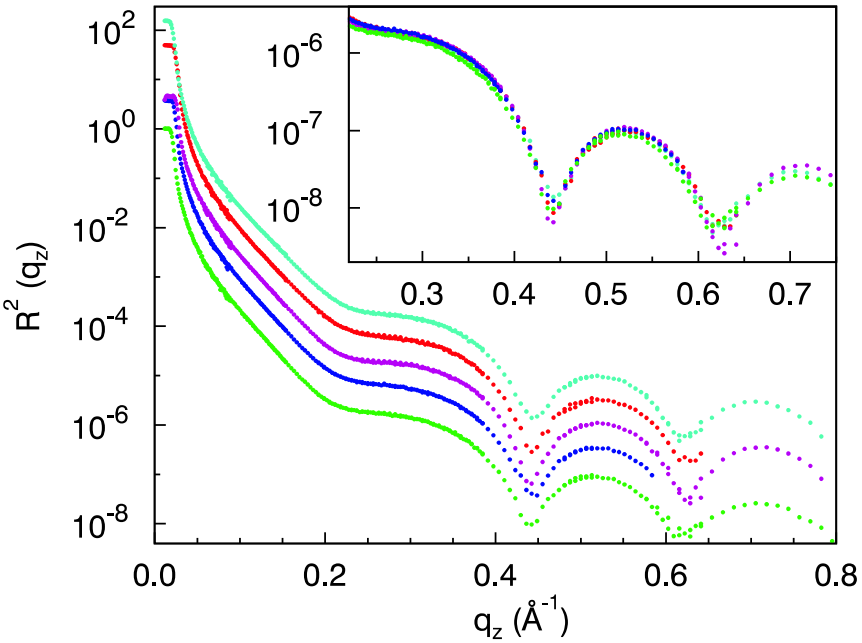

Figure 6.12: X-ray reflectivity of the OTS-layer immersed in water, which was saturated with a variety of gases (light green (bottom): degassed, blue: CO, purple: CO_2, red: Ar, dark green (top): 0.5 M HCl). The curves are shifted vertically for clarity. In the inset a magnification of the high q-range is shown, where the measurement is most sensitive. All measured reflectivity curves are identical up to the maximum momentum transfer achieved in the experiments.

drophobicity or indeed mediated by an electronic (hard core) repulsion. To answer this question, the results obtained from the data analysis in Sec. 6.3 are discussed in a more general framework by comparison with interfacial profiles calculated by R. Roth within a DFT model of classical fluids at a solid wall (see Fig. 6.13 and Sec. 3.3.2).

Due to the non-vanishing roughness imposed by any real substrate, the density profiles are smeared and the oscillatory features are damped out (see inset in Fig. 6.13). The excess adsorption, i.e. the integrated density $\rho(z)$ minus the bulk density, is very close in both cases (hydrophilic and hydrophobic interface), so water density depletion does not seem to be unique to hydrophobic surfaces. The detection of density depletion due to purely hydrophobic effects is therefore a formidable challenge to experiment.

Using the density depicted in Fig. 6.13, it is now possible to visualize the density depletion at a contrast-matched ($\sigma_\mathrm{i} = 2\,\text{Å}$, $d_\mathrm{i} = 25\,\text{Å}$, $\rho_\mathrm{i} = \rho_{\mathrm{H_2O}}$) hydrophobic (see Fig. 6.14a) or hydrophilic (see Fig. 6.14b) layer on top of a denser semi-infinite substrate ($\sigma_\mathrm{s} = 1\,\text{Å}$, $\rho_\mathrm{s} = 2\rho_{\mathrm{H_2O}}$). The integrated density deficit at the hydrophobic interface is $1.1\,\mathrm{g\,cm^{-3}}$ Å, whereas the integrated density deficit at the hydrophilic wall is $0.6\,\mathrm{g\,cm^{-3}}$ Å.

Taking the simplified density profiles from Figs. 6.14a,b, it is straightforward to calculate the normalized reflectivity R^2/R_F^2 in the kinematic approximation for the hydrophobic

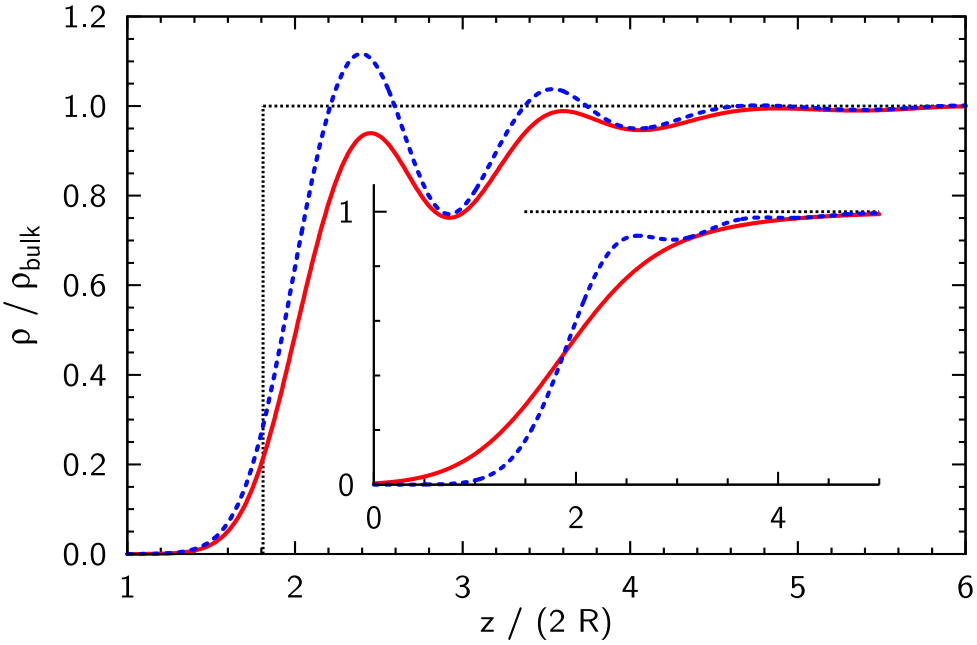

Figure 6.13: Density profiles of a square-well fluid at a repulsive ($\Theta = 120^{\circ}$, dashed line) and at an attractive wall ($\Theta = 80^{\circ}$, solid line). The vertical dashed line at $3.26\,R = 5.07$Å denotes the position of the hydrophobic wall for the experimentally obtained integrated density deficit of $1.1\,\mathrm{g\,cm^{-3}}$ Å. (inset) Convolution of the interfacial profile at the hydrophilic wall with a Gaussian ($\sigma = 1$ Å, dashed line; $\sigma = 2$ Å, solid line) mimicking the roughness of the underlying substrate.

and hydrophilic solid-liquid interface. Figure 6.14c shows that the hydrophobic and the hydrophilic case approximately differ by a factor of two only. For comparison, the difference in the normalized reflectivity signal from the OTS-layer in air (see Fig. 6.3) and the OTS-layer immersed in water (see Fig. 6.10) varies between one and two orders of magnitude as a function of q_z. Apparently, the unambiguous detection of the increase of the depletion layer caused by hydrophobic effects is very challenging.

6.7 Radiation damage in the OTS-layer

X-ray reflectivity measurements on dry OTS-samples could be performed without any noticeable damage induced by the x-ray beam. On the other hand, performing the same measurements on OTS-layers immersed in water causes severe damage of the organic molecules. In the following, the interface degradation with radiation dose is quantified by monitoring the reflected x-ray intensity at fixed momentum transfer q_z as a function of time. Adjusting the momentum transfer to the minimum of the reflectivity curve at $q_z = 0.44\,\mathrm{Å}^{-1}$ (see Fig. 6.10 and inset of Fig. 6.15a), maximum sensitivity to structural

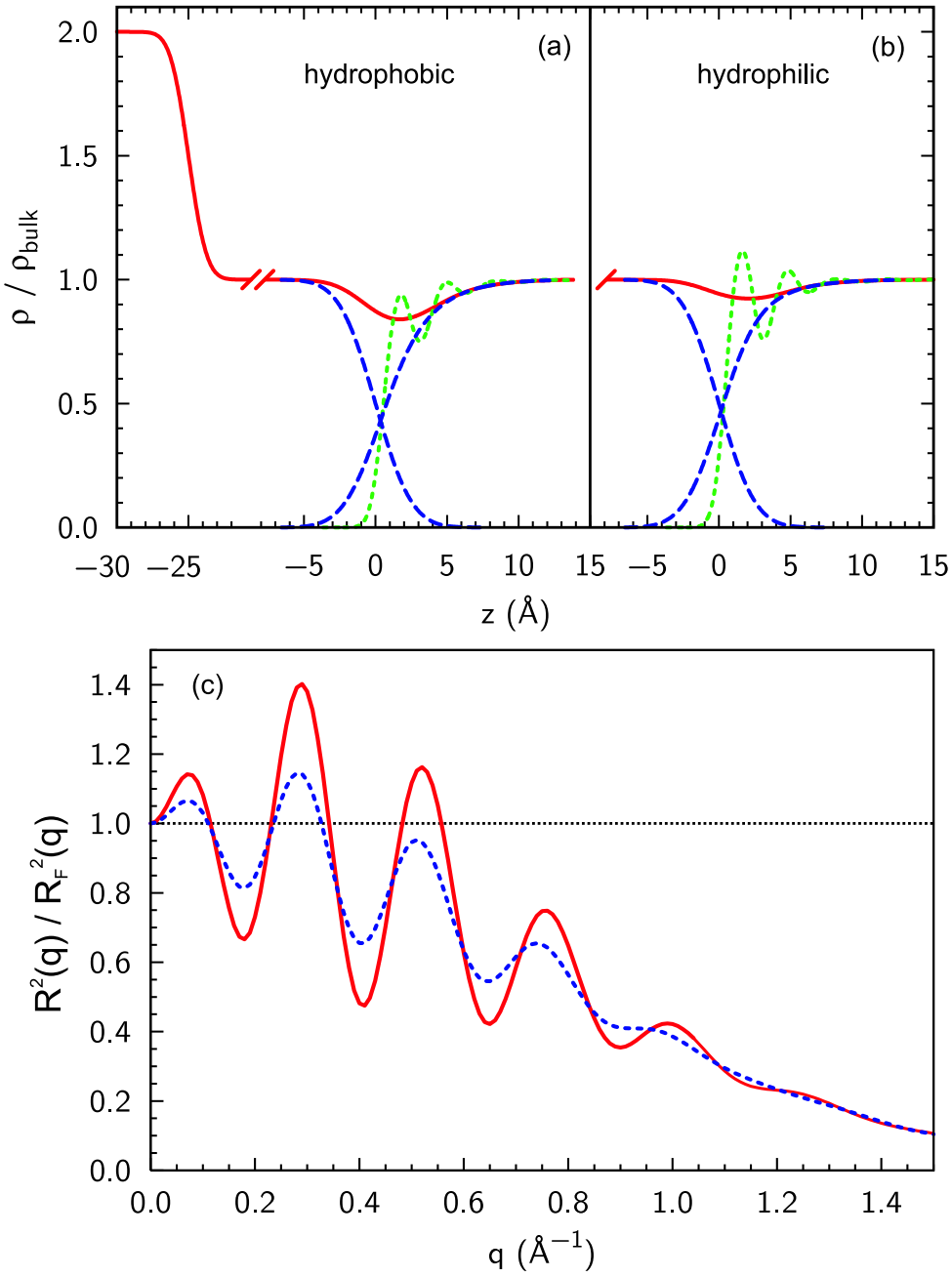

Figure 6.14: Density profiles of the fluid in contact with a contrast-matched hydrophobic (a) or hydrophilic (b) organic layer on top of a denser semi-infinite substrate. The calculated profiles (dotted curves) are convoluted with a Gaussian (dashed curve) in order to account for the surface roughness of the organic layer (dashed curve). (c) Calculated reflection pattern R^2/R_{F}^2 for the hydrophobic (solid line) and the hydrophilic solid-liquid interface (dashed line).

changes in the OTS-film is achieved. At this position, even small structural modifications change the destructive interference in the x-ray reflectivity pattern and lead to a clearly visible intensity increase (known in conventional optics as "Aufhellung").

If the main mechanism of radiation damage leads to a decreased length of the hydrocarbon tail of the OTS molecule, the second minimum in the x-ray reflectivity pattern shifts to larger values of q_z resulting in a strong increase in the measured intensity until a maximum is reached. Indeed, this is experimentally observed for the OTS-layer immersed in water after $200\,\mathrm{s}$ irradiation with the full x-ray beam. After $400\,\mathrm{s}$ another minimum is reached in the reflection pattern. After approx. $1000\,\mathrm{s}$, the measured x-ray reflectivity at a fixed position in q_z is stationary. Recording the entire reflectivity curve confirms that any features related to a layered structure on top of the SiO_2 are absent (see the lower insets in Fig. 6.15a). This points to destruction and at least partial removal of the OTS-layer from the surface.

Most (surface and interface) diffraction beamlines at synchrotron radiation facilities are operated at x-ray energies below $20\,\mathrm{keV}$. Figure 6.15b shows that the energy absorbed by a water molecule at $20\,\mathrm{keV}$ is more than five times larger compared to the absorption at $72.5\,\mathrm{keV}$. High energy x-rays are therefore well suited to minimize energy deposition in the organic layer.

Figure 6.15b shows that – after an incubation time of about $50\,\mathrm{s}$ – the x-ray intensity at the interference minimum starts to increase indicating the onset of the degradation of the OTS-layer. An irradiation of $50\,\mathrm{s}$ with a flux density of $3.8 \cdot 10^{13}\,\mathrm{photons\,mm^{-2}s^{-1}}$ in the incidence beam at the sample position corresponds to a total deposited dose of about $600\,\mathrm{kGy}$ in water. In the hydrophobic OTS-layer this flux results in average to an absorbed energy of $2.7\,\mathrm{meV/s}$ in one $(CH_2)_{18}$ hydrocarbon chain. To break one C-C bond per alkyl chain by photons directly absorbed in the OTS-layer requires therefore in average approximately $1300\,\mathrm{s}$. The much faster degeneration observed in the experiments gives evidence for secondary processes with significantly higher efficiency.

The fast degeneration of the OTS-layer during x-ray irradiation of the sample immersed in water in comparison to the sample measured in air, Ar, or N_2 can be explained by the formation of OH-radicals [146]. They are created in secondary Auger electron cascades [147] in the water. The radicals can diffuse to the organic layer where chemical reactions with the alkyl chain are triggered. At the beginning of this process, the damaged molecules are well separated from each other. These diluted point defects are not observable in x-ray reflectivity. From a certain threshold on the defects (e.g. polar defects, such as hydroxyl groups, or charged defects after further oxidation to deprotonated carboxylic acid) start to interact with each other, leading to a collective distortion of the well ordered alkyl chains. Radicals formed in the organic layer react with neighboring chains, leading to a strongly cross-linked polymer-like film. Similar effects were also found in the degeneration of SAMs in XPS studies [148]. Since no significant damage on dry OTS-layers was found in this work, it is concluded that the chemical path, including OH-radicals, is dominant. Other mechanisms, induced by free electrons (photo electrons, Compton electrons) generated in the substrate, are less effective. This is also confirmed by time-dependent

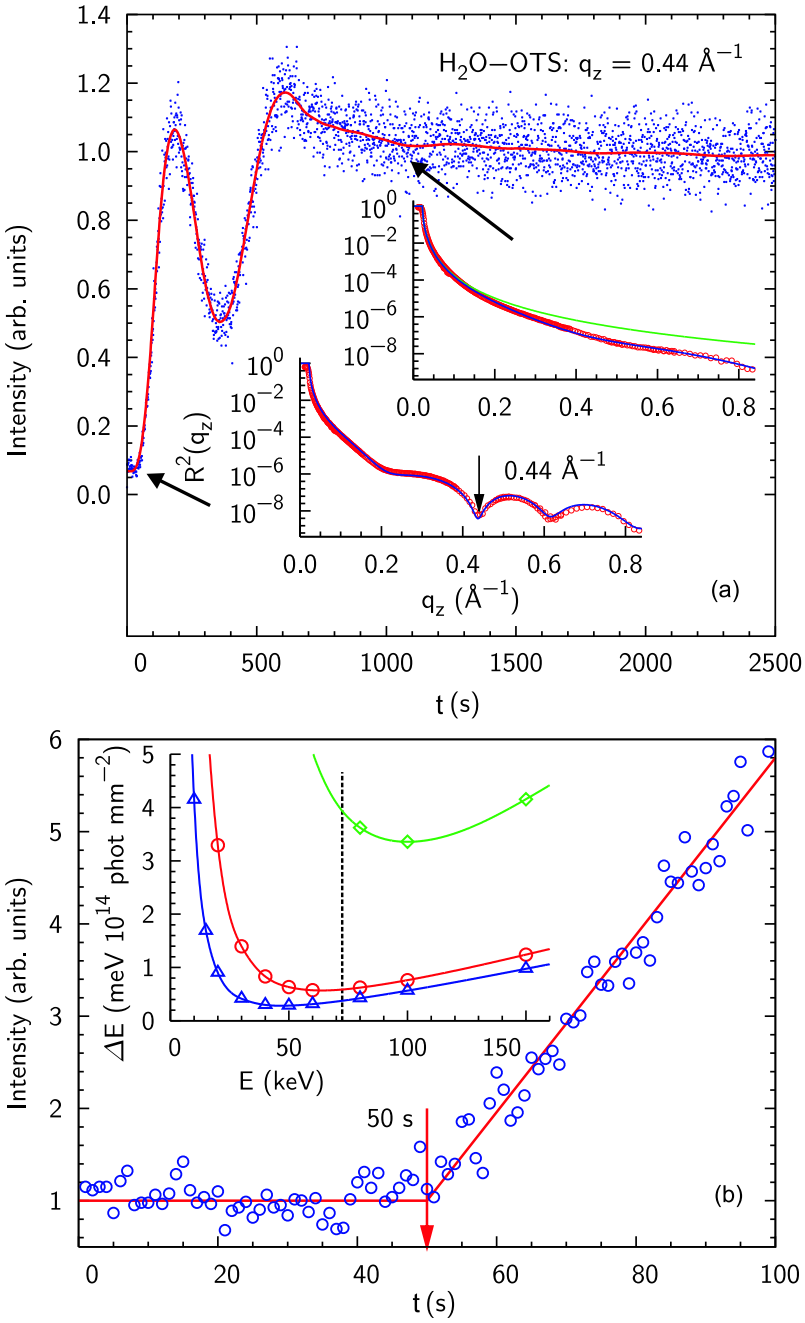

Figure 6.15: (a) Time-dependent variation of the x-ray reflectivity from the OTS sample immersed in water at the position of destructive interference at $q_z = 0.44\,\text{Å}^{-1}$. The full reflectivity curve is shown before radiation damage sets in (lower inset) and after irradiation of approx. $1000\,\text{s}$ (upper inset). (b) Magnification of the initial part of (a). The radiation damage sets in after approx. 50 seconds. (inset) Absorbed x-ray energy ΔE per $10^{14}\,\text{photons}\,\text{mm}^{-1}$ in one SiO_2 (diamonds) or H_2O (circles) molecule, and a CH_2 (triangles) group, respectively. Values for the mass energy-absorption coefficients were taken from Hubbell and Seltzer [137] (symbols) and interpolated (solid lines). The vertical dashed line at $72.5\,\text{keV}$ denotes the x-ray energy used in this work.

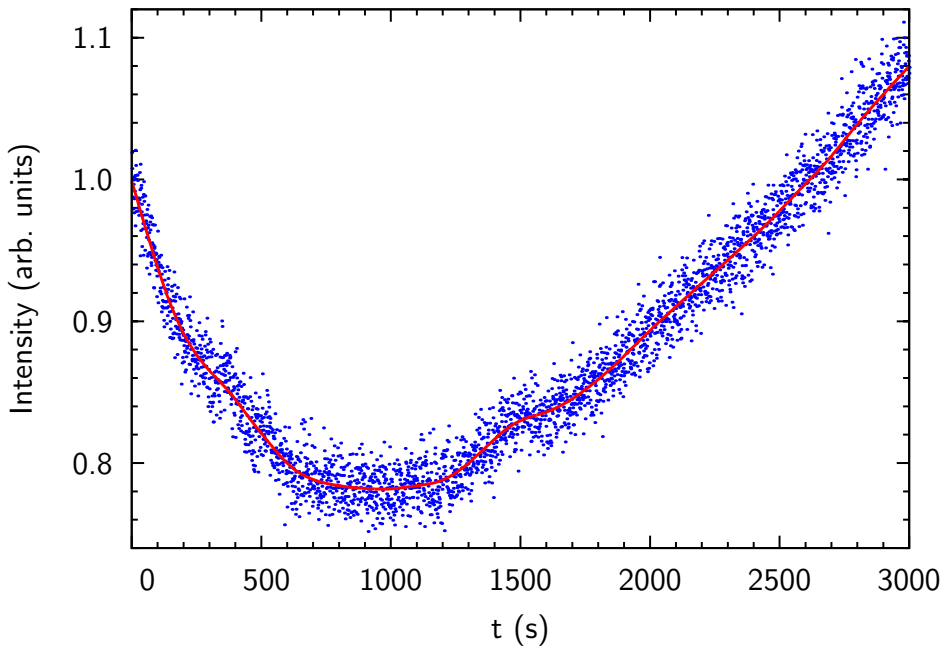

Figure 6.16: Time-dependent variation of the x-ray reflectivity at $q_z = 0.21\,\text{Å}^{-1}$ from an ice-OTS interface kept at $-10°\text{C}$.

measurements of the x-ray reflectivity from an ice-OTS interface[2]. Figure 6.16 clearly shows that the radiation damage occurs on much larger time scales. Since the total yield of secondary electrons is comparable in water and ice [147], the reduced radiation damage at the ice-OTS interface is attributed to the reduced mobility of radicals created by the secondary electrons. The reduced diffusivity of the radicals in the solid ice phase hinders the progression of the radiation damage significantly. On time scales accessible in the experiments the OTS-layers could, in fact, never be completely destroyed at the ice-OTS interface.

In order to avoid radiation damage during data taking, the sample cell was translated perpendicular to the x-ray beam while measuring the reflectivity of the sample immersed in water. Each single data point was thus taken on a fresh and undamaged spot spaced by $24\,\mu\text{m}$ on the interface (see Sec. 5.4.1). Below a momentum transfer of $q_z = 0.7\,\text{Å}^{-1}$ the counting time was kept well below the onset time of $40\,\text{s}$ for the observed radiation damage in Fig. 6.15b. The illumination time was increased to $30\,\text{s}$ only for the last data points at momentum transfer values $q_z > 0.7\,\text{Å}^{-1}$.

Figure 6.17 shows a lateral scan over a region which was previously irradiated for $\tau = 90\,\text{s}$ on two spots separated by $40\,\mu\text{m}$. The profile shows two peaks which can be modeled by identical Gaussian profiles with a FWHM of the damaged region of $26.8\,\mu\text{m}$. This

[2] Measurements on the ice-OTS interface were performed in collaboration with S. Schöder. Experimental details as well as further analysis and discussion can be found in [40, 149].

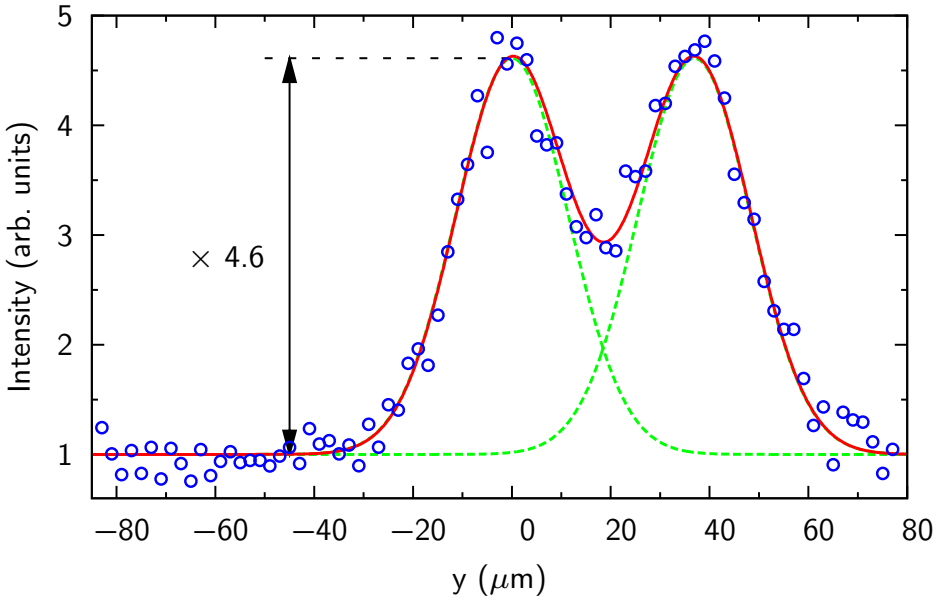

Figure 6.17: Lateral scan over an area which was previously irradiated on two spots, spaced by $40\,\mu\mathrm{m}$, for $90\,\mathrm{s}$ each, at an incident angle α_i corresponding to $q_z = 0.44\,\text{Å}^{-1}$. The solid line is a fit with two identical Gaussians (dashed lines).

corresponds directly to the width of the horizontal beam profile $\Delta_\mathrm{h} = 24\,\mu\mathrm{m}$ extracted from the knife edge scan (see Fig. 5.3). The intensity increase by a factor of 4.6 is in good agreement with the increase extracted from Fig. 6.15b for an irradiation time of $\tau = 90\,\mathrm{s}$. This clearly shows that the beam damage is local and confined to the irradiated area only. No additional broadening of the damaged region due to OH-radical diffusion on a $\mu\mathrm{m}$ scale was observed. This is in contrast to recent claims [90] that beam damage on samples immersed in water can be significantly reduced by working with a thin film ($\mu\mathrm{m}$) cell in order to minimize the amount of OH-radicals created in the beam path in comparison to the bulk setup used in this work.

Chapter 7

Conclusions

In this thesis, a high energy x-ray reflectivity study of the density profiles of water at hydrophobic and hydrophilic substrates is presented. This technique is an ideal tool to study the structure of deeply buried interfaces on a sub-nanometer scale. The experiments have been performed at the high energy beamline ID15A at the European Synchrotron Radiation Facility (ESRF) in Grenoble, France. This thesis contributed to the optimization of the novel HEMD setup towards a system allowing quantitative, both surface and interface sensitive high energy x-ray scattering experiments at the experimental limit. For experiments at solid-liquid interfaces, a novel sample cell was developed which is adapted to the special requirements.

As a model system for hydrophobic non-polar organic substances, which are highly relevant in technical and biological processes, Si-wafers functionalized with OTS-SAMs were selected. At the hydrophobic water-OTS interface, clear indications for the existence of a small water depletion gap were found. The key results of this work are:

- The integrated density depletion amounts to $d_{\mathrm{w}}\left(\rho_{\mathrm{H_2O}} - \rho_{\mathrm{w}}\right) = 1.1 \pm 0.1\,\text{Å g cm}^{-3}$ extending over a maximum of two molecular layers.
- The influence of a variety of gases dissolved in water could be excluded.
- Nanobubble formation as a cause of the observed effects could be ruled out.
- OH-radicals are most likely the dominant driving factor for radiation damage.

A systematic study of radiation damage effects detected at the dry OTS surface, the water-OTS interface, and the ice-OTS interface revealed that x-ray induced decomposition of the OTS-layer is most pronounced in liquid water. In addition, the radiation damage is highly localized on the irradiated area on a $\mu\mathrm{m}$ scale. In combination with estimations of the absorbed energy, these results suggest a dominant role of OH-radicals arising from secondary Auger electrons in the complex damage mechanism. The analysis of the scattering intensity distributions parallel to the interface gives clear evidence that the observed density depletion is not caused by nanobubbles as detected in some AFM measurements. Additional measurements performed on water enriched with a representative selection of

different noble, non-polar, and polar gases clearly show that these gases do not influence the hydrophobic density depletion zone at a single sharp wall on the length scale of a few molecular diameters. In contrast to these results, experiments on water in confinement measuring the long-ranged hydrophobic interactions on a $10\,\mathrm{nm}$ scale have shown a significant decrease of the attractive forces when dissolved gases are present in the water [100]. The observed density depletion at the hydrophobic OTS interface corresponds to approximately 40% of a monolayer of water molecules. This value agrees well with previous x-ray reflectivity measurements at the interface between a paraffin monolayer on top of water performed by Jensen et al. [27] as well as qualitatively with recent neutron reflectivity experiments [89].

To determine the extent of the interfacial deviation from the bulk density precisely by means of reflectivity experiments, both a sharp interface as well as high instrumental real space resolution are mandatory. The latter depends on a large dynamic range since a wide q-range up to large momentum transfer needs to be covered. Brilliant high-energy synchrotron radiation gives access to deeply-buried-solid-liquid interfaces with a flatness on the molecular level. This approach meets the requirements mentioned above for high precision studies. In this work, we consequently optimized it towards the experimental limits and could thus achieve the today most accurate determination of the maximum extent of the interfacial structure: The region with a density deviation from the bulk value could be confined to one to two molecular diameters, i.e. the length scale of the average OO distance and the correlation length in liquid bulk water [57, 59]. Whereas our approach provides an ideal tool for high-accuracy measurements, different probes employed in previous studies have to deal with intrinsic limitations: At free liquid interfaces, thermally excited capillary waves give rise to an inherent roughness; in neutron reflectivity experiments, the low flux from nuclear reactors and spallation sources, compared with third generation synchrotrons, is the restricting factor.

However, what are the bottlenecks for even more precise experiments, and where are the general limits? The main restrictions are the following: Primarily, the dynamic range accessible in a scattering experiment is given by the incident flux and the background level (see Sec. 4.4). In the near future technical improvements at ID15 will increase the flux by two orders of magnitude for experiments using the HEMD setup. While this speeds up the experiments tremendously, it will not allow the collection of reflectivity data at higher q-values since radiation damage permits only the deposition of a fixed x-ray dose on the organic material. The second limitation is that substrate surfaces with sub molecular roughness are essential for the determination of the interfacial structure on a molecular level, since x-rays average over the coherently illuminated sample area and thus convolute the intrinsic local profile with the interfacial roughness. Since the OTS substrate is composed of densely packed hydrocarbon chains, the minimum interfacial corrugation is the radius of a methyl group, i.e. approximately $2\,\text{Å}$. Together with results from AFM measurements reported in literature [66], the reflection pattern recorded on the dry sample shows that further optimization of the well-ordered OTS substrates is exhausted.

An important factor for the size of the interfacial density depletion is the molecular surface morphology that can alter interfacial properties significantly as demonstrated by

Mamatkulov et al. [79]. In analogy to the high solubility of small non-polar objects (e.g. H_2 or CH_4) in liquid bulk water, the hydrogen bond network can arrange more readily around interfacial protrusions than on a solid flat wall. The characteristic length scale for these curvature effects can be estimated from the structural dimensions in solid water [150]. The diameter of the hexagonal channels in ice 1h is given by the lattice parameter of 4.5 Å along the a-axis [151]. This corresponds to the spherical cap diameter of the terminal methyl groups of the OTS alkyl chains of approximately 4 Å. Thus, the molecular morphology may explain the smaller experimental values for the interfacial density depletion found in this thesis and in a previous study by Jensen et al. [27] in comparison to MD simulations [30, 79].

Since hydrophobic and hydrophilic interfaces may both exhibit a density depletion [30, 89], it is not possible to confirm the existence of a specific hydrophobic water gap unambiguously. Due to the lack of a contrast-matched reference layer, the result for the hydrophilic water-SiO_2 interface is less conclusive, but still allows for the existence of a small water depletion gap, which could be a generic feature to any solid-liquid interface. Deeper insight in the mechanisms leading to the interfacial density depletion was revealed from calculations employing a simple DFT model of classical fluids at hydrophobic and hydrophilic solid walls (see Sec. 3.3.2). Here the water molecules are modeled as hard spheres with an isotropic interaction potential. These assumptions provide the requirements for the observation of packing effects at a solid wall as well as the influence of the total interfacial tension, represented by the macroscopic contact angle. By comparison with the experimental findings from the hydrophobic substrate, an integrated density depletion of 0.6 Å g cm^{-3} was predicted for a more hydrophilic interface with a contact angle of $80°$. This decrease is in qualitative agreement with recent MD simulations performed by Janecek et al. [30].

Further complications arise from the non-spherical water molecule exhibiting a strong dipole moment and participating in a locally ordered hydrogen bond network. This non-isotropic behavior leads to an additional orientational ordering of the water molecules near the solid interface. Here, the ratio between dispersive VdW and polar contributions to the total interfacial tension, as well as the hydrogen bond acceptor and donor properties are also highly relevant. Since x-rays are essentially insensitive to hydrogen atoms, direct information on the orientational arrangement and the local hydrogen bond structure has to be deduced from MD simulations or other experimental methods such as SFG spectroscopy techniques [30, 34].

Another source of density depletion at hydrocarbon interfaces are the terminal methyl groups. Their electron density is smaller than the one of the middle part of the alkyl chains. This is an intrinsic depletion layer present at all interfaces with a high areal density of terminal hydrogen atoms. The magnitude of this effect can be estimated from the intermolecular depletion zone in bulk crystalline alkanes or lipid bilayers. Employing x-ray crystallography Craievich et al. obtained an electron depletion in the methyl region of crystalline long chain alkanes of $0.58\,e$Å^{-2} [152]. Ocko et al. calculated a depletion of $0.58\,e$Å^{-2} [153] from the interfacial region in lipid bilayers [154]. For a comparison of

the electron depletion associated to a single layer of densely packed methyl groups, these values have to be divided by a factor of two. The depletion can partially be explained by packing effects but clearly shows that the methyl groups may contribute significantly to the interfacial electron depletion of $\Gamma = 0.3\,e\text{Å}^{-2}$ found in this work.

In conclusion, this work presents an x-ray reflectivity study of hydrophobic water-solid interfaces at the experimental limit. Even though the molecular arrangement of the water molecules cannot be determined with this technique, the integrated density depletion and the extent of the depleted zone was established with unrivaled precision. These key results serve both as benchmark as well as reference values for comparison with recent and future theoretical and experimental findings [8, 30, 155, 156]. There are still many open questions concerning the interfacial structure of water at hydrophilic and hydrophobic interfaces. For several of them x-ray scattering methods are the ideal tool to get access to structural information on the molecular length scale. Some of the questions that may be tackled in the near future are addressed in the following outlook.

Chapter 8

Outlook

General scope

This thesis is part of a long term project in the department for low-dimensional and metastable materials at the Max Plack Institute for Metals Research in cooperation with the high energy scattering beamline ID15 at the ESRF exploring the structure of deeply buried interfaces [9]. One starting point was the work of Oliver Klein and Dr. Matthias Denk [132] on silicon-liquid metal interfaces, which later was continued by Dr. John Okasinski [134]. On the other hand, the project of Dr. Simon Engemann [104] [133] was focused on native SiO_2-ice interfaces and recently extended by Dr. Sebastian Schöder [149] to various other substrates. The observation of a quasi-liquid interfacial water layer suggested a further study of solid-water interfaces with emphasis on hydrophobic surfaces. First attempts in cooperation with Dr. Craig Priest and Dr. David Snoswell from the Ian Wark Reseach Institute in Adelaide showed that a successful completion of this very challenging task requires a highly optimized system based on a detailed analysis of the expected signal and the inevitable damage, the x-rays leave on the sample.

Future projects

The results obtained in this thesis pave the way to a large variety of interesting studies which have either already been started or may be tackled in the future. An open question addresses the physical origin of the observed density depletion at the hydrophobic interface. The interpretation depends strongly on whether it is a special hydrophobic or water specific phenomenon or a generic feature associated with any solid-liquid interface. For a deeper understanding, additional experiments are necessary.

Changing the contact angle of the surface can be achieved, both by the surface preparation and by the type of liquid used. In principle, the deposition of hydrophilic SAMs, based on organic alkanol-silanes or perfluorinated molecules, are straightforward. However, the additional interaction between the polar functional alcohol groups leads to a less-ordered film and therefore to a larger interfacial roughness. Within this thesis, first experiments not shown in this work were performed on fluorinated SAMs. By exchanging water with a non-polar liquid (e.g. alkanes) the interactions within the liquid bulk phase change from

mainly hydrogen bonding to purely VdW, resulting in a totally different interaction potential. Here, the disadvantage is the much larger size of the molecules compared to water, which renders a direct comparison of the results rather complicated. From theoretical considerations, one expects a different temperature trend for the effects contributing to the interfacial density depletion. While DFT models and MD simulations predict an increased gap with rising temperature, the orientational ordering of the asymmetric water molecules decreases, favoring a high-entropy configuration. Since the MD simulations performed by Mamatkulov et al. predict a higher compressibility of the interfacial water, a slight decrese of the interfacial density depletion with incresed preassure is expected [79]. Molecular ordering of the interfacial water molecules may be influenced by changing the pH [93] or applying an external electric field [92, 157].

Depending on their position in the Hofmeister series [158], salts dissolved in water can act both as structure builder and structure breaker for the hydrogen-bonding network. Therefore, they may alter the interfacial structure significantly [89]. Further optimization also should be done on the preparation of well-defined OTS-ice interfaces. They can give a deeper insight into the phenomena of interfacial melting.

Within this work, first experiments on liquid-liquid interfaces between water, hexane, and perfluorohexane were also performed. They clearly showed that the liquid mode of the HEMD setup at ID15A [60] is highly competitive with state of the art beamlines specially designed for this purpose [61]. However, the intrinsic roughness at fluid interfaces caused by capillary waves limits the accessible q_z-range to approximately $0.3\,\text{Å}^{-1}$. While this q_z-range is insufficient for the extraction of real space information on the molecular length scale of water, interesting studies of surfactant adsorption are possible.

Another fruitful project, emerging from the experiments on solid-water interfaces, concerns the study of layering effects of Room Temperature Ionic Liquids (RTILs) at solid surfaces, where first results were already obtained [128]. Whereas the size of the water molecule is only $2.8\,\text{Å}$, the size of the cations and anions of RTILs ranges up to one nanometer. Therefore, in contrast to this work, molecular resolution can be achieved in the x-ray reflectivity experiments.

Appendix A

Abbreviations and Acronyms

AFM	**A**tomic **F**orce **M**icroscope
AMPW	**A**symmetrical **M**ulti**P**ole **W**iggler
ASA	**A**daptive **S**imulated **A**nnealing
CRL	**C**ompound **R**efractive **L**ens
DFT	**D**ensity **F**unctional **T**heory
ESRF	**E**uropean **S**ynchrotron **R**adiation **F**acility
FWHM	**F**ull **W**idth of **H**alf **M**aximum
HEMD	**H**igh **E**nergy X-ray **M**icro **D**iffraction Setup
ID	**I**nsertion-**D**evice (at a straight section of a synchrotron)
MD	**M**olecular **D**ynamic
NR	**N**eutron **R**eflectivity
OTS	**O**ctadecyl-**T**richloro**S**ilane
p.a.	**p**ro **a**nalysi (analysis grade)
PE-HD	**P**oly**E**thylene (**h**igh **d**ensity)
PFA	**P**er**F**luor**A**lkoxy Copolymer
PMMA	**P**oly**M**ethyl **M**eth**A**crylate
PTFE	**P**oly**T**etra**F**luoro**E**thylene
RTIL	**R**oom **T**emperature **I**onic **L**iquid
SAM	**S**elf **A**ssembled **M**onolayer
SFE	**S**urface **F**ree **E**nergy
SFG	**S**um **F**requency **G**eneration
SLD	**S**cattering **L**ength **D**ensity
TDS	**T**hermal **D**iffuse **S**cattering
TOC	**T**otal **O**rganic/**O**xidizable **C**arbon
VdW	**V**an **d**er **W**aals

Appendix B

Symbols used in Equations

Elementary constants

CODATA internationally recommended values of the fundamental physical constants where taken from NIST [159].

$a_0 = \frac{4\pi\epsilon_0\hbar^2}{m_e e^2} = 5.2918 \cdot 10^{-11}\,\mathrm{m}$	Bohr radius
$c = 2.9979 \cdot 10^{8}\,\mathrm{ms}^{-1}$	vacuum light speed
$e = 1.6022 \cdot 10^{-19}\,\mathrm{C}$	elementary charge
$\epsilon_0 = 8.8542 \cdot 10^{-12}\,\mathrm{Fm}^{-1}$	permittivity of free space
$\hbar = 1.0546 \cdot 10^{-34}\,\mathrm{Js}$	Planck constant $/2\pi$
$k_\mathrm{B} = 1.3807 \cdot 10^{-23}\,\mathrm{JK}^{-1}$	Boltzmann constant
$\lambda_\mathrm{C} = \frac{h}{m_e c} = 2.4263 \cdot 10^{-12}\,\mathrm{m}$	Compton wavelength of an electron
$m_\mathrm{e} = 9.1094 \cdot 10^{-31}\,\mathrm{kg}$	electron mass
$N_\mathrm{A} = 6.0221 \cdot 10^{-23}\,\mathrm{mol}^{-1}$	Avogadro constant
$r_\mathrm{e} = \frac{e^2}{4\pi\epsilon_0 m_e c^2} = 2.8179 \cdot 10^{-15}\,\mathrm{m}$	classical electron radius

Symbols

a_i, b_i, c	form factor interpolation coefficients from [127]
$\alpha_\mathrm{c} \approx \sqrt{2\delta}$	critical angle of total reflection
α_f	exit angle
α_i	incidence angle
β	optical constant (imaginary part)
C_Z	Compton factor for small momentum transfer
χ^2	deviation between fitted and experimental data
d	thickness
δ	optical constant (real part)

E	x-ray energy
η	packing fraction of hard spheres
$f_0\,(q)$	angular dependent part of the atomic scattering form factor
$f^{(1)}\,(E)$	real part of the atomic scattering form factor in forward scattering
$f^{(2)}\,(E)$	imaginary part of the atomic scattering form factor in forward scattering
$F\,(q)$	structure factor
$G\,(r)$	correlation function
γ	surface or interfacial tension, surface free energy (SFE)
γ^{D}	dispersive contribution to the SFE
γ^{H}	hydrogen bond contribution to the SFE
γ^{P}	polar contribution to the SFE
Γ	interfacial electron deficit
I	scattered x-ray intensity
$\vec{k_{\mathrm{i}}}$	incidence wave vector
$\vec{k_{\mathrm{f}}}$	final wave vector
$\lambda = \frac{hc}{E}$	x-ray wavelength
m	mass
μ_{material}	mass attenuation coefficient of the specified material
$n = 1 - \delta + i\beta$	complex optical constant or refractive index
Ω	grand canonical potential
$P = \frac{1}{2}\left[1 + \cos^2 2\vartheta\right]$	polarization factor for nonpolarized x-rays
$P_{\parallel} = 1$	polarization factor for parallel polarization
$P_{\perp} = \cos^2 2\vartheta$	polarization factor for perpendicular polarization
ψ	scattering angle in polarization plane
$\vec{q} = \vec{k_{\mathrm{f}}} - \vec{k_{\mathrm{i}}}$	scattering vector
q_{c}	maximal wave vector transfer for total reflection
q_{max}	maximum momentum transfer achieved in an experiment
q_z	z-component of the scattering vector
$R^2\,(q_z)$	x-ray reflectivity
ρ_{e}	electron density
ρ_{material}	mass density of the specified material
ρ_{mol}	molar density
$S\,(q)$	liquid structure factor
t	time
T	temperature
$2\vartheta = \alpha_{\mathrm{i}} + \alpha_{\mathrm{f}}$	total scattering angle
Z	atomic number

Bibliography

[1] M. Schneider. *Leonardo da Vinci, Das Wasserbuch*. Schirmer, München, (1996). Aus dem Engl. von Helmut Reuter.

[2] R. Ludwig and D. Paschek. Anomalien und Rätsel – Wasser. *Chem. Unserer Zeit*, **39** 164–175, (2005).

[3] P. Ball. *H_2O: Biographie des Wassers*. Piper, München, (2001). Aus dem Engl. von Helmut Reuter.

[4] D. Chandler. Two faces of water. *Nature*, **417** 491, (2002).

[5] W. Kauzmann. Some factors in the interpretation of protein denaturation. *Adv. Prot. Chem.*, **14** 1–63, (1959).

[6] J. Israelachvili and H. Wennerström. Role of hydration and water structure in biological and colloidal interactions. *Nature*, **379** 219–225, (1996).

[7] D. Chandler. Interfaces and the driving force of hydrophobic assembly. *Nature*, **437** 640–647, (2005).

[8] D. Chandler. Oil on troubled water. *Nature*, **445** 831–832, (2007).

[9] H. Reichert, V. Honkimäki, A. Snigirev, S. Engemann, and H. Dosch. A new x-ray transmission-reflection scheme for the study of deeply buried interfaces using high energy microbeams. *Physica B*, **336** 46–55, (2003).

[10] L. G. Parratt. Surface studies of solids by total reflection of x-rays. *Phys. Rev*, **95** 359–369, (1954).

[11] P. S. Pershan. Structure of surfaces and interfaces as studied using synchrotron radiation - liquid surfaces. *Faraday Discuss. Chem. Soc.*, **89** 231–245, (1990).

[12] M. Tolan. *X-Ray Scattering from Soft Matter Thin Films*. Springer, Berlin, (1999).

[13] L. Ingber. Simulated annealing: Practice versus theory. *Math. Comput. Model.*, **18** 29–57, (1993).

[14] J. W. G. Tyrrell and P. Attard. Images of nanobubbles on hydrophobic surfaces and their interactions. *Phys. Rev. Lett.*, **87** 176104, (2001).

[15] J. Mahnke, J. Stearnes, R. A. Hayes, D. Fornasiero, and J. Ralston. The influence of dissolved gas on the interaction surfaces of different hydrophobicities in aqueous media. *Phys. Chem. Chem. Phys.*, **1** 2793–2798, (1999).

[16] T. Koishi, S. Yoo, K. Yasuoko, X. C. Zeng, T. Narumi, R. Susukita, A. Kawai, H. Furusawa, A. Suenaga, N. Okimoto, N. Futatsugi, and T. Ebisuzaki. Nanoscale hydrophobic interaction and nanobubble nucleation. *Phys. Rev. Lett.*, **93** 185701, (2004).

[17] A. Luzar and D. Bratko. Gas solubility in hydrophobic confinement. *J. Phys. Chem. B*, **109** 22545–22552, (2005).

[18] A. C. Simonsen, P. L. Hansen, and B. Klosgen. Nanobubbles give evidence of incomplete wetting at a hydrophobic interface. *J. Colloid Interface Sci.*, **273** 291–299, (2004).

[19] M. Holmberg, A. Kuhle, J. Garnaes, K. A. Morch, and A. Boisen. Nanobubble trouble on gold surfaces. *Langmuir*, **19** 10510–10513, (2003).

[20] Unnahbares Wasser. Max Plack press releases C63/2006(221), http://www.mpg.de/bilderBerichteDokumente/dokumentation/pressemitteilungen/2006/pressemitteilung20061207/, December (2006).

[21] Mind the gap. ESRF press releases, http://www.esrf.eu/news/pressreleases/gap/, November (2006).

[22] B. Wirsing. So nah und doch so fern. *Max Planck Forschung*, page 10, (2007). http://www.mpg.de/bilderBerichteDokumente/multimedial/mpForschung/2007/heft01/pdf7.pdf.

[23] A. K. Soper and M. A. Ricci. Structures of high-density and low-density water. *Phys. Rev. Lett.*, **84** 2881–2884, (2000).

[24] G. Hura, J. M. Sorenson, R. M. Glaeser, and T. Head-Gordon. A high-quality x-ray scattering experiment on liquid water at ambient conditions. *J. Chem. Phys.*, **113** 9140–9148, (200).

[25] C. Y. Lee, J. A. McCammon, and P. J. Rossky. The structure of liquid water at an extended hydrophobic surface. *J. Chem. Phys.*, **80** 4448–4455, (1984).

[26] J. R. Grigera, S. G. Kalko, and J. Fischbarg. Wall-water interface. a molecular dynamics study. *Langmuir*, **12** 154–158, (1996).

[27] T. R. Jensen, M. O. Jensen, N. Reitzel, K. Balashev, G. H. Peters, K. Kjaer, and T. Bjornholm. Water in contact with extended hydrophoobic surfaces: Direct evidence of weak dewetting. *Phys. Rev. Lett.*, **90** 086101, (2003).

[28] N. Giovambattista, P. J. Rossky, and P. G. Debenedetti. Effect of pressure on the phase behavior and structure of water confined between nanoscale hydrophobic and hydrophilic plates. *Phys. Rev. E*, **73** 041604, (2006).

[29] N. Giovambattista, P. G. Debenedetti, and P. J. Rossky. Effect of surface polarity on water contact angle and interfacial hydration structure. *J. Phys. Chem. B*, **111** 9581–9587, (2007).

[30] J. Janecek and R. R. Netz. Interfacial water at hydrophobic and hydrophilic surfaces: Depletion versus adsorption. *Langmuir*, **23** 8417–8429, (2007).

[31] Z. Ge, D. G. Cahill, and P. V. Brown. Thermal conductance of hydrophilic and hydrophobic interfaces. *Phys. Rev. Lett.*, **96** 186101, (2006).

[32] V. Ostroverkhov, G. A. Waychunas, and Y. R. Shen. New information on water interfacial structure revealed by phase-sensitive surface spectroscopy. *Phys. Rev. Lett.*, **94** 046102, (2005).

[33] Y. R. Shen and V. Ostroverkhov. Sum-frequency vibrational spectroscopy on water interfaces: Polar orientation of water molecules at interfaces. *Chem. Rev.*, **106** 1140–1154, (2006).

[34] L. F. Scatena, M. G. Brown, and G. L. Richmond. Water at hydrophobic surfaces: Weak hydrogen bonding and strong orientation effects. *Science*, **292** 908–912, (2001).

[35] Q. Du, E. Freysz, and Y. R. Shen. Surface vibrational scectroscopic studies of haydrogen bonding and hydrophobicity. *Science*, **264** 826–828, (1994).

[36] R. Steitz, T. Gutberlet, T. Hauss, B. Klosgen, R. Krastev, S. Schemmel, A. C. Simonsen, and G. H. Findenegg. Nanobubbles and their precursor layer at the interface of water against a hydrophobic substrate. *Langmuir*, **19** 2409–2418, (2003).

[37] D. Schwendel, T. Hayashi, R. Dahint, A. Pertsin, M. Grunze, R. Steitz, and F. Schreiber. Interaction of water with self-assembled monolayers: Neutron reflectivity measurements of the water density in the interface region. *Langmuir*, **19** 2284–2293, (2003).

[38] D. A. Doshi, E. B. Watkins, J. N. Israelachvili, and J. Majewski. Reduced water density at hydrophobic surfaces: Effect of dissolved gases. *Proc. Natl. Acad. Sci. U.S.A.*, **102** 9458–9462, (2005).

[39] M. Mezger, H. Reichert, S. Schöder, J. Okasinski, H. Schröder, H. Dosch, D. Palms, J. Ralston, and V. Honkimäki. High-resolution in situ x-ray study of the hydrophobic gap at the water-octadecyl-trichlorosilane interface. *Proc. Natl. Acad. Sci. U.S.A.*, **49** 18401–18404, (2006).

[40] M. Mezger, S. Schöder, H. Reichert, H. Schröder, J. Okasinski, V. Honkimäki, J. Ralston, J. Bilgram, R. Roth, and H. Dosch. Water and ice in contact with OTS functionalized surfaces: A high resolution x-ray reflectivity study. *J. Chem. Phys.*, (2008). in print.

[41] P. Ball. *H_2O: A Biography of Water*. Weidenfeld & Nicolson, London, (1999).

[42] V. F. Petrenko and R. W. Whitworth. *Physics of Ice*. Oxford University Press, Oxford, (1999).

[43] S. Sastry. Water structure: Order and oddities. *Nature*, **409** 300–301, (2001).

[44] J. A. Odutola and T. R. Dyke. Partially deuterated water dimers: Microwave spectra and structure. *J. Chem. Phys.*, **72** 5062–5070, (1980).

[45] C. G. Salzmann, P. G. Radaelli, A. Hallbrucker, E. Mayer, and J. L. Finney. The preparation and structures of hydrogen ordered phases of ice. *Science*, **311** 1758–1761, (2006).

[46] J. D. Bernal and R. H. Fowler. A theory of water and ionic solution, with particular reference to hydrogen and hydroxyl ions. *J. Chem. Phys.*, **1** 515–548, (1933).

[47] L. Pauling. The structure and entropy of ice and of other crystals with some randomness of atomic arrangement. *J. Am. Chem. Soc.*, **57** 2680–2684, (1935).

[48] K. Röttger, A. Endriss, J. Ihringer, S. Doyle, and W. F. Kuhs. Lattice constants and thermal expansion of H_20 and D_20 ice Ih between 10 and 265 K. *Acta Cryst.*, **B50** 644–648, (1994).

[49] C. M. B. Line and R. W. Whitworth. A high resolution neutron powder diffraction study of D_2O ice XI. *J. Chem. Phys.*, **104** 10008–10013, (1996).

[50] W. C. Röntgen. Ueber die constitution des flüssigen wassers. *Annalen der Physik und Chemie*, **281** 91–97, (1892).

[51] P. G. Debenedetti. Supercooled and glassy water. *J. Phys.: Condens. Matter*, **15** R1669–R1726, (2003).

[52] H. E. Stanley, S. V. Buldyrev, G. Franzese, N. Giovambattista, and F. W. Starr. Static and dynamic heterogeneities in water. *Phil. Trans. R. Soc. A*, **363** 509–523, (2005).

[53] J. M. Sorenson, G. Hura, R. M. Glaeser, and T. Head-Gordon. What can x-ray scattering tell us about the radial distribution functions of water? *J. Chem. Phys.*, **113** 9149–9161, (200).

[54] T. Head-Gordon and G. Hura. Water structure from scattering experiments and simulation. *Chem. Rev.*, **102** 2651–2669, (2002).

[55] A. H. Narten. Liquid water: Atom pair correlation functions from neutron and x-ray diffraction. *J. Chem. Phys.*, **56** 5681–5687, (1972).

[56] K. Nishikawa and N. Kitagawa. X-ray diffraction study of liquid water. *Bull. Chem. Soc. Jpn.*, **53** 2804–2808, (1980).

[57] L. Bosio, J. Teixeira, and H. E. Stanley. Enhanced density fluctuations in supercooled H_2O, D_2O, and ethanol-water solutions: Evidence from small-angle x-ray scattering. *Phys. Rev. Lett.*, **46** 597–600, (1981).

[58] L. Bosio, J. Teixeira, and M.-C. Bellissent-Funel. Enhanced density fluctuations in water analyzed by neutron scattering. *Phys. Rev. A*, **39** 6612 – 6613, (1989).

[59] Y. Xie, K. F. Ludwig, G. Morales, D. E. Hare, and C. M. Sorensen. Noncritical behavior of density fluctuations in supercooled water. *Phys. Rev. Lett.*, **71** 2050–2053, (1993).

[60] V. Honkimäki, H. Reichert, J. S. Okasinski, and H. Dosch. X-ray optics for liquid surface/interface spectrometers. *J. Synchrotron Rad.*, **13** 426–431, (2006).

[61] M. L. Schlossman. X-ray scattering from liquid-liquid interfaces. *Physica B*, **357** 98–105, (2005).

[62] K. Lum, D. Chandler, and J. D. Weeks. Hydrophobicity at small and large length scales. *J. Phys. Chem. B*, **103** 4570–4577, (1999).

[63] Y. S. Seo and S. Satija. No intrinsic depletion layer on a polystyrene thin film at a water interface. *Langmuir*, **22** 7113–7116, (2006).

[64] M. Fujii, S. Sugisawa, K. Fukada, T. Kato, T. Shirakawa, and T. Seimiya. Packing of hydrocarbon and perfluorocarbon chains planted on oxidized surface of silicon as studied by ellipsometry and atomic-force microscopy. *Langmuir*, **10** 984–987, (2004).

[65] I. M. Tidswell, T. A. Rabedeau, P. S. Pershan, S. D. Kosowsky, J. P. Folkers, and G. M. Whitesides. X-ray grazing-incidence diffraction from alkylsiloxane monolayers on silicon-wafers. *J. Chem. Phys.*, **95** 2854–2861, (1991).

[66] M. Fujii, S. Sugisawa, K. Fukada, T. Kato, and T. Seimiya. Hexagonally close-packed alkyl chains silylized on oxidized silicon surface. *Langmuir*, **11** 405–407, (2005).

[67] R. A. Bonham, L. S. Bartell, and D. A. Kohl. The molecular structures of n-pentane, n-hexane and n-heptane. *J. Am. Chem. Soc.*, **81** 4765–4769, (1959).

[68] R. Boese, H. C. Weiss, and D. Blaser. The melting point alternation in the short-chain n-alkanes: Single-crystal x-ray analyses of propane at 30 k and of n-butane to n-nonane at $90\,\mathrm{K}$. *Angew. Chem. int. Ed.*, **38** 988–992, (1999).

[69] Y. Wang and M. Lieberman. Growth of ultrasmooth octadecyltrichlorosilane self-assembled monolayers on SiO_2. *Langmuir*, **19** 1159–1167, (2003).

[70] Y. Liu, L. K. Wolf, and M. C. Messmer. A study of alkyl chain conformational changes in self-assembled n-octadecyltrichlorosilane monolayers on fused silica surfaces. *Langmuir*, **17** 4329–4335, (2001).

[71] F. M. Fowkes. Attractive forces at interfaces. *Industrial and Engineering Chemistry*, **56** 40–52, (1964).

[72] D. K. Owens. Estimation of the surface free energy of polymers. *J. Appl. Polym. Sci.*, **13** 1741–1747, (1969).

[73] R. Evans. The nature of the liquid-vapour interface and other topics in the statistical mechanics of non-uniform, classical fluids. *Adv. Phys.*, **28** 143–200, (1979).

[74] F. van Swol and J. R. Henderson. Wetting and drying transitions at a fluid-wall interface: Density-functional theory versus computer simulation. *Phys. Rev. A*, **40** 2567–2578, (1989).

[75] R. Evans, J. R. Henderson, and R. Roth. Nonanalytic curvature contributions to solvation free energies: Influence of drying. *J. Chem. Phys.*, **121** 12074–12084, (2004).

[76] R. Roth, R. Evans, A. Lang, and G. Kahl. Fundamental measure theory for hard-sphere mixtures revisited: the White Bear version. *J. Phys.: Condens. Matter*, **14** 12063–12078, (2002).

[77] L. Cheng, P. Fenter, K. L. Nagy, M. L. Schlegel, and N. C. Sturchio. Molecular-scale density oscillations in water adjacent to a mica surface. *Phys. Rev. Lett.*, **87** 156103, (2001).

[78] S. H. Park and G. Sposito. Structure of water adsorbed on a mica surface. *Phys. Rev. Lett.*, **89** 0845501, (2002).

[79] S. I. Mamatkulov, P. K. Khabibullaev, and R. R. Netz. Water at hydrophobic substrates: Curvature, pressure, and temperature effects. *Langmuir*, **20** 4756–4763, (2004).

[80] A. Schreiber, I. Ketelsen, and G. H. Findenegg. Melting and freezing of water in ordered mesoporous silica materials. *Phys. Chem. Chem. Phys.*, **3** 1185–1195, (2001).

[81] C. Y. Ruan, V. A. Lobastov, F. Vigliotti, S. Chen, and A. H. Zewail. Ultrafast electron crystallography of interfacial water. *Science*, **304** 80–84, (2004).

[82] P. J. Eng, T. P. Trainor, G. E. Brown Jr., G. A. Waychunas, M. Newville, S. R. Sutton, and M. L. Rivers. Structure of the hydrated α-Al_2O_3 (0001) surface. *Science*, **288** 1029–1033, (2000).

[83] H. Ogasawara, B. Brena, D. Nordlund, M. Nyberg, A. Pelmenschikov, L. G. M. Pettersson, and A. Nilsson. Structure and bonding of water on Pt(111). *Phys. Rev. Lett.*, **89** 276102, (2002).

[84] I. M. P. Aarts, A. C. R. Pipino, J. P. M. Hoefnagels, W. M. M. Kessels, and M. C. M. van de Sanden. Quasi-ice monolayer on atomically smooth amorphous SiO_2 at room temperature observed with a high-finesse optical resonator. *Phys. Rev. Lett.*, **95** 166104, (2005).

[85] A. Verdaguer, G. M. Sacha, H. Bluhm, and M. Salmeron. Molecular structure of water at interfaces: Wetting at the nanometer scale. *Chem. Rev.*, **106** 1478–1510, (2006).

[86] L. B. R. Castro, A. T. Almeida, and D. F. S. Petri. The effect of water or salt solution on thin hydrophobic films. *Langmuir*, **20** 7610 –7615, (2004).

[87] M. Mao, J. Zhang, R. H. Yoon, and W. A. Ducker. Is there a thin film of air at the interface between water and smooth hydrophobic solids. *Langmuir*, **20** 1843–1849, (2004).

[88] Y. Takata, J. H. J. Cho, B. M. Law, and M. Aratono. Ellipsometric search for vapor layers at liquid-hydrophobic solid surfaces. *Langmuir*, **22** 1715–1721, (2006).

[89] M. Maccarini, R. Steitz, M. Himmelhaus, J. Fick, S. Tatur, M. Wolff, M. Grunze, J. Janecek, and R. R. Netz. Density depletion at solid-liquid interfaces: A neutron reflectivity study. *Langmuir*, **23**, (2007).

[90] A. Poynor, L. Hong, I. K. Robinson, S. Granick, Z. Zhang, and P. A. Fenter. How water meets a hydrophobic surface. *Phys. Rev. Lett.*, **97**, (2006).

[91] P. Geissbühler, P. Fenter, E. DiMasi, G. Srajer, L. B. Sorensen, and N. C. Sturchio. Three-dimensional structure of the calcite-water interface by surface x-ray scattering. *Surface Science*, **573** 191–203, (2001).

[92] M. F. Toney, J. N. Howard, J. Richer, G. L. Borges, J. G. Gordon, O. R. Melroy, D. G. Wiesler, D. Yee, and L. B. Sorensen. Voltage-dependent ordering of water molecules at an electrode-electrolyte interface. *Nature*, **368** 444–446, (1994).

[93] A. J. Hopkinsa, C. L. McFearina, and G. L. Richmond. Investigations of the solid-aqueous interface with vibrational sum-frequency spectroscopy. *Curr. Opin. Solid State Mat. Sci.*, **9** 19–27, (2005).

[94] V. Ostroverkhov, G. A. Waychunas, and Y. R. Shen. Vibrational spectra of water at water/α-quartz (0001) interface. *Chem. Phys. Letters*, **386** 144–148, (2004).

[95] J. N. Israelachvili and R. Pashley. The hydrophobic interaction is long-range, decaying exponentially with distance. *Nature*, **300** 341–342, (1982).

[96] H. K. Christenson and P. M. Claesson. Direct measurements of the force between hydrophobic surfaces in water. *Adv. Colloid Interface Sci.*, **91** 391–436, (2001).

[97] S. Singh, J. Houston, F. van Swol, and C. J. Brinker. Drying transition of confined water. *Nature*, **442** 526, (2006).

[98] D. R. E. Snoswell, J. Duan, D. Fornasiero, and J. Ralston. Colloid stability and the influence of dissolved gas. *J. Phys. Chem. B*, **107** 2986–2994, (2003).

[99] W. Gong, J. Stearnes, D. Fornasiero, R. A. Hayes, and J. Ralston. The influence of dissolved gas on the interactions between surfaces of different hydrophobicity in aqueous media. *Phys. Chem. Chem. Phys.*, **1** 2799–2803, (1999).

[100] E. Meyer E, K. J. Rosenberg, and J. Israelachvili. Recent progress in understanding hydrophobic interactions. *Proc. Natl. Acad. Sci. U.S.A.*, **103** 15739–15746, (2006).

[101] N. Ishida, T. Inoue, N. Miyahara, and K. Higashitani. Nano bubbles on a hydrophobic surface in water observed by tapping-mode atomic force microscopy. *Langmuir*, **16** 6377–6380, (2000).

[102] J. Yang, J. Duan, D. Fornasiero, and J. Ralston. Very small bubble formation at the solid-water interface. *J. Phys. Chem. B*, **107** 6139–6147, (2003).

[103] M. Rauscher, H. Reichert, S. Engemann, and H. Dosch. Local density profiles in thin films and multilayers from diffuse x-ray and neutron scattering. *Phys. Rev. B*, **72** 205401, (2005).

[104] S. Engemann. *Premelting at the ice–SiO_2 interface - A high-energy x-ray microbeam diffraction study*. PhD thesis, University of Stuttgart, Faculty of Mathematics and Physics, (2005).

[105] A. Braslau, M. Deutsch, P. S. Pershan, A. H. Weiss, J. AlsNielsen, and J. Bohr. Surface-roughness of water measured by x-ray reflectivity. *Phys. Rev. Lett.*, **54** 114–117, (1985).

[106] O. M. Magnussen, B. M. Ocko, M. J. Regan, K. Penanen, P. S. Pershan, and M. Deutsch. X-ray reflectivity measurements of surface layering in liquid mercury. *Phys. Rev. Lett.*, **74** 4444–4447, (1995).

[107] J. Als-Nielsen and D. McMorrow. *Elements of Modern X-Ray Physics*. Wiley & Sons Ltd, Chichester, (2001).

[108] J. D. Jackson. *Classical electrodynamics*. Wiley, New York, 3. edition, (1999).

[109] B. L. Henke, E. M. Gullikson, and J. C. Davis. X-ray interactions: Photoabsorption, scattering, transmission, and reflection at $E = 50-30,000$ eV, $Z = 1-92$. *Atomic Data and Nuclear Data Tables*, **54** 181–342, (1993).

[110] C. T. Chantler, K. Olsen, R. A. Dragoset, A. R. Kishore, S. A. Kotochigova, and D. S. Zucker. *X-Ray Form Factor, Attenuation and Scattering Tables*. National Institute of Standards and Technology, Gaithersburg, (2003). http://physics.nist.gov/ffast.

[111] C. T. Chantler. Detailed tabulation of atomic form factors, photoelectric absorption and scattering cross section, and mass attenuation coefficients in the vicinity of absorption edges in the soft x-ray ($Z = 30-36$, $Z = 60-89$, $E = 0.1\,\text{keV} - 10\,\text{keV}$), addressing convergence issues of earlier work. *J. Phys. Chem. Ref. Data*, **29** 597–1048, (2000).

[112] H. Vaclav, U. Pietsch, and T. Baumbach. *High-resolution x-ray scattering from thin films and multilayers*, volume 149 of *Springer tracts in modern physics*. Springer, Berlin, (1999).

[113] L. Nevot and P. Croce. Characterization of surfaces by grazing x-ray reflection - application to study of polishing of some silicate-glasses. *Rev. de Physique Appliquee*, **15** 761–779, (1980).

[114] D. K. G. de Boer and A. J. G. Leenaers. Probing interface roughness by x-ray scattering. *Physica B*, **221** 18–26, (1996).

[115] M. J. Regan, E. H. Kawamoto, S. Lee, P. S. Pershan, N. Maskil, M. Deutsch, O. M. Magnussen, B. M Ocko, and L. E. Berman. Surface layering in liquid gallium - an x-ray reflectivity study. *Phys. Rev. Lett.*, **75** 2498–2501, (1995).

[116] M. J. Regan, P. S. Pershan, O. M. Magnussen, B. M. Ocko, M. Deutsch, and L. E. Berman. Capillary-wave roughening of surface-induced layering in liquid gallium. *Phys. Rev. B*, **45** 9730–9733, (1996).

[117] C. Braun. Parratt or The Reflectivity Tool. HMI, Berlin, (1997-2002).

[118] W. Schweika, H. Reichert, W. Babik, O. Klein, and S Engemann. Strain-induced incomplete wetting at CuAu(001) surfaces. *Phys. Rev. B*, **70** 041401, (2004).

[119] M. Paulus, C Gutt, and M Tolan. Surface roughness and adsorption isotherms of molecularly thin liquid films: An x-ray reflectivity study. *Phys. Rev. E*, **72** 061601, (1995).

[120] L. Ingber. Adaptive simulated annealing (ASA). http://www.ingber.com, (2004).

[121] M. J. Berger, J. H. Hubbell, S. M. Seltzer, J. Chang, J. S. Coursey, R. Sukumar, and D. S. Zucker. *XCOM: Photon Cross Section Database*. National Institute of Standards and Technology, Gaithersburg, (2005). http://physics.nist.gov/PhysRefData/Xcom/Text/XCOM.html.

[122] W. J. Huisman, J. F. Peters, J. W. Derks, H. G. Ficke, D. L. Abernathy, and J. F. van der Veen. A new x-ray diffraction method for structural investigations of solid-liquid interfaces. *Rev. Sci. Instrum.*, **68** 4169–4176, (1997).

[123] P. A. Fenter. X-ray reflectivity as a probe of mineral-fluid interfaces: A user guide. *Rev. Mineral. Geochem.*, **49** 149–221, (2002).

[124] O. Klein and Y. Nishina. The scattering of light by free electrons according to Dirac's new relativistic dynamics. *Nature*, **122** 398–399, (1928).

[125] O. Klein and Y. Nishina. Über die Streuung von Strahlung durch freie Elektronen nach der neuen relativistischen Quantendynamik von Dirac. *Z. Phys. A*, **52** 853–868, (1929).

[126] J. H. Hubbell, W. J. Veigele, E. A. Briggs, R. T. Brown, D. T. Cromer, and R. J. Howerton. Atomic form factors, incoherent scattering functions, and photon scattering cross sections. *J. Phys. Chem. Ref. Data*, **4** 471–538, (1975).

[127] T. Hahn, editor. *International tables for crystallography, Vol. C Mathematical, physical and chemical tables*. Kluwer, Dordrecht, 2. edition, (1999).

[128] M. Mezger, H. Schröder, H. Reichert, S. Schramm, J. S. Okasinski, S. Schöder, V. Honkimäki, M. Deutsch, B. M. Ocko, J. Ralston, and H. Dosch. Extended molecular layering of a pyrrolidinium-based ionic liquid at the sapphire(0001) surface. (in preparation).

[129] V. Honkimäki. The ID15A high energy scattering beamline. http://www.esrf.eu/UsersAndScience/Experiments/MaterialsScience/ID15, (2006). European Synchrotron Radiation Facility, ID15, Grenoble, France.

[130] P. Suortti and T. Tschentscher. High-energy scattering beamlines at European Synchrotron Radiation Facility. *Rev. Sci. Instrum.*, **66** 1798, (1995).

[131] H. Reichert. The high energy micro diffraction (HEMD) instrument at the ESRF. http://www.mf.mpg.de/en/abteilungen/dosch/hemd/, (2006). MPI for Metals Research, Stuttgart, Germany.

[132] M. Denk. *Structural Investigation of Solid-Liquid Interfaces. Metal-Semiconductor Interface*. PhD thesis, University of Stuttgart, Faculty of Mathematics and Physics, (2006).

[133] S. Engemann, H. Reichert, H. Dosch, J. Bilgram, V. Honkimäki, and A. Snigirev. Interfacial melting of ice in contact with SiO_2. *Phys. Rev. Lett.*, **92** 205701–1–4, (2004).

[134] H. Reichert, M. Denk, J. Okasinski, V. Honkimäki, and H. Dosch. Giant metal compression at liquid-solid (Pb-Si, In-Si) schottky junctions. *Phys. Rev. Lett.*, **98** 116101, (2007).

[135] B. Lengeler, C. G. Schroer, M. Richwin, J. Tümmler, M. Drakopoulos, A. Snigirev, and I. Snigireva. A microscope for hard x rays based on parabolic compound refractive lenses. *Appl. Phys. Lett.*, **74** 3924–3926, (1999).

[136] N. Huber. HUBER Diffraktionstechnik. http://www.xhuber.com. Rimsting, Germany.

[137] J. H. Hubbell and S. M. Seltzer. *Tables of X-Ray Mass Attenuation Coefficients and Mass Energy-Absorption Coefficients*. National Institute of Standards and Technology, Gaithersburg, (1996). http://www.physics.nist.gov/PhysRefData/XrayMassCoef/cover.html.

[138] V. Honkimäki. private communication.

[139] W. Kern. *Handbook of Semiconductor Wafer Cleaning Technology*. Noyes, Park Ridge, New Jersey, (1993).

[140] T. M. McIntire, S. R. Smalley, J. T. Newberg, A. S. Lea, J. C. Hemminger, and B. J. Finlayson-Pitts. Substrate changes associated with the chemistry of self-assembled monolayers on silicon. *Langmuir*, **22** 5617–5624, (2006).

[141] S. Garoff, E. B. Sirota, S. K. Sinha, and H. B. Stanley. The effects of substrate roughness on ultrathin water films. *J. Chem. Phys.*, **90** 7505–7515, (1989).

[142] S. R. Wasserman, G. M. Whitesides, I. M. Tidswll, B. M. Ocko, P. S. Pershan, and J. D. Axe. The structure of self-assembled monolayers of alkylsiloxanes on silicon - a comparison of results from ellipsometry and low-angle x-ray reflectivity. *J. Am. Chem. Soc.*, **111** 5852–5861, JUL (1989).

[143] I. M. Tidswell, B. M. Ocko, P. S. Pershan, S. R. Wasserman, G. M. Whitesides, and J. D. Axe. X-ray specular reflection studies of silicon coated by organic monolayers (alkylsiloxanes). *Phys. Rev. B*, **41** 1111–1128, (1990).

[144] A. F. Holleman and N. Wiberg. *Lehrbuch der anorganischen Chemie*. de Gruyter, Berlin, (2007).

[145] J. Yang, J. Duan, D. Fornasiero, and J. Ralston. Kinetics of CO_2 nanobubble formation at the solid/water interface. *Phys. Chem. Chem. Phys.*, (2007). DOI: 10.1039/b709624k.

[146] I. Farhataziz and M. A. J. Rodgers, editors. *Radiation Chemistry: Principles and Applications*. VCH, (1987).

[147] N. I. Timneanu, C. Caleman, J. Hajdu, and D. van der Spoel. Auger electron cascades in water and ice. *J. Chem. Phys.*, **299** 277–283, (2004).

[148] A. Shaporenko, M. Zharnikov, P. Feulner, and D. Menzel. Quantitative analysis of temperature effects in radiation damage of thiolate-based self-assembled monolayers. *J. Phys.: Condens. Matter*, **18** 1677–S1689, (2006).

[149] S. Schöder. *Substrate-Dependence of the Ice Premelting at Heterogeneous Interfaces: An X-Ray Scattering Study*. PhD thesis, University of Stuttgart, Faculty of Mathematics and Physics, (2008).

[150] F. H. Stillinger. Structure in aqueous solutions of nonpolar solutes from the standpoint of scaled-particle theory. *J. Solut. Chem.*, **2** 141–158, (1973).

[151] K. Röttger, A. Endriss, J. Ihringer, S. Doyle, and W. F. Kuhs. Lattice constants and thermal expansion of H_2O and D_2O ice Ih between 10 and 265 K. *Acta Cryst.*, **B50** 644–648, (1994).

[152] A. F. Craievich, I. Denicolo, and J. Douchet. Molecular motion and conformational defects in odd-numbered paraffins. *Phys. Rev. B*, **30** 4782–4787, (1984).

[153] B. M. Ocko, A. Dhinojwala, and J. Daillant. *Comment on A. Poynor et al., Phys. Rev. Lett. 97, 266101 (2006)*, (to be published).

[154] M. C. Wiener, R. M. Suter, and J. F. Nagle. Structure of the fully hydrated gel phase of dipalmitoylphosphatidylcholine. *Biophys. J.*, **55** 315–325, (1989).

[155] S. Subramanian and S. Sampath. Dewetting phenomenon: Interfacial water structure at well-organized alkanethiol-modified goldŰaqueous interface. *J. Colloid Interface Sci.*, **313** 64–71, (2007).

[156] A. E. Ismail, G. S. Grest, and M. J. Stevens. Structure and dynamics of water near the interface with oligo(ethylene oxide) self-assembled monolayers. *Langmuir*, **32** 8508–8514, (2007).

[157] Z. D. Schultz, S. K. Shaw, and A. A. Gewirth. Potential dependent organization of water at the electrified metal-liquid interface. *J. Am. Chem. Soc.*, **127** 15916 –15922, (2005).

[158] F. Hofmeister. Zur Lehre von der Wirkung der Salze. *Arch. Exp. Pathol. Pharmacol.*, **24** 247–260, (1888).

[159] The nist reference on constants, units, and uncertainty. http://www.physics.nist.gov/cuu/, (2006).

Danksagung

Ganz herzlich möchte ich mich bei all denjenigen bedanken, die zum Gelingen dieser Arbeit beigetragen haben. Mein besonderer Dank gilt Herrn **Prof. Dr. Helmut Dosch** für die freundliche Aufnahme am Max-Planck-Institut für Metallforschung, seine ständige Diskussionsbereitschaft sowie das große Interesse mit dem er die Entwicklung dieser Arbeit verfolgte. Ebenso danke ich meinem Betreuer Herrn **Dr. Harald Reichert** für die Vermittlung der experimentellen Fertigkeiten, den fruchtbaren Gedankenaustausch bei der Datenanalyse und deren Interpretation sowie die konstruktive Mithilfe bei der Korrektur dieser Arbeit. Bei Herrn **Prof. Dr. Clemens Bechinger** bedanke ich mich für die Übernahme des Mitberichts.

Ohne die unermüdliche Hilfe von **Heiko Schröder**, **Sebastian Schöder** und **Dr. John Okasinski** während der Strahlzeiten in Grenoble wäre der ununterbrochene 24-h Betrieb der Beamline unmöglich gewesen. Zusammen mit **Dr. Ingo Ramsteiner**, **Dr. Simon Engemann**, **Dr. János Major** und **Dr. Sandrine Dourdain** standen sie mir in vielen Fragen mit Rat und Tat hilfreich zur Seite.

Für den produktiven Aufenthalt am Ian Wark Institut der University of South Australia in Adelaide danke ich Herrn **Prof. Dr. John Ralston**. Zusammen mit **Dr. Dennis Palms** und **Dr. Rossen Sedev** führte er mich in die Präparation und Charakterisierung hydrophober Oberflächen ein und beriet bei der Auswahl des geeigneten Materialsystems für die Reflektivitätsexperimente. Für die Hilfestellung während der Experimente an der ESRF möchte ich mich sowohl bei der Crew von ID15, **Dr. Veijo Honkimäki**, **Dr. Thomas Buslaps**, **Dr. Diego Pontoni**, **Dr. Federica Venturini**, **Dr. Gabriela Gonzalez Aviles**, **Mogens Kretzschmer**, **Anthony Mauro** als auch beim Leiter des zentralen Chemielabors **Dr. Harald Müller** ganz herzlich bedanken.

Durch die Kooperation mit **Dr. Roland Roth** lernte ich den theoretischen Hintergrund von fest-flüssig-Grenzflächen besser zu verstehen und meine experimentellen Ergebnisse aus anderer Warte zu interpretieren. Weitere Diskussionen, welche zu einem vertieften Verständnis führten, konnte ich mit **Prof. Dr. Moshe Deutsch**, **Dr. Ben Ocko**, **Prof. Dr. Jörg Bilgram** und **Prof. Dr. Ian Robinson** führen. Auch von unserer studentischen wissenschaftlichen Hilfskraft **Björn Wehinger** sowie **Sebastian Schramm** und **Tobias Lampmann** deren Diplomarbeiten ich begleiten durfte, konnte ich immer wieder Neues lernen.

Für die exzellente technische Unterstützung möchte ich mich bei **Annette Weißhardt**, **Frank Adams**, **Rolf Henes**, **Arnold Weible**, **Thomas Meisner** und **Helmut Wendel** ganz

herzlich bedanken. Bezüglich der präzisen Anfertigung der experimentellen Aufbauten, welche in dieser Arbeit Verwendung fanden, konnte ich immer auf die mechanische Werkstatt am ITAP unter der Leitung von Herrn **Michael Schäfer**, die feinmechanische Werkstatt von Frau **Sabine Seiffert** und die Glaswerkstatt von Herrn **Helmut Kammerlander** jeweils mit ihrem Team zählen. Bei der Installation und Wartung des Clusters, auf dem die Datenanalyse durchgeführt wurde, war die Unterstützung durch **Dr. András Major** sehr hilfreich.

Auf meine Bürokollegen **Dr. Reinhard Streitel**, **Alexander Reicho** und **Claus Ellinger** konnte ich stets zählen. In kritischer gegenseitiger Betrachtung unserer Experimente und Ergebnisse lernte ich Fragestellungen abseits meines Themengebiets kennen, wurde aber auch auf interessante Aspekte meiner eigenen Arbeit aufmerksam gemacht. Für die gute Zusammenarbeit, die freundliche Arbeitsatmosphäre und die gemeinsame Zeit bei außerdienstlichen Unternehmungen möchte ich mich darüber hinaus bei allen Mitarbeitern der Abteilung Dosch bedanken.

Schließlich danke ich meinen Eltern, die mir das Studium ermöglicht und mich stets unterstützt haben.